FEDERAL UNIVERSITY OF ITAJUBÁ
POST-GRADUATION PROGRAM OF
MECHANICAL ENGINEERING

METAMODEL-BASED STATIC AND DYNAMIC OPTIMIZATION OF COMPOSITE STRUCTURES WITH PLY DROP-OFFS

CAMILA APARECIDA DINIZ

Itajubá – MG
2022

FEDERAL UNIVERSITY OF ITAJUBÁ
POST-GRADUATION PROGRAM OF
MECHANICAL ENGINEERING

METAMODEL-BASED STATIC AND DYNAMIC OPTIMIZATION OF COMPOSITE STRUCTURES WITH PLY DROP-OFFS

CAMILA APARECIDA DINIZ

This thesis was presented to the Post-Graduation Program of Mechanical Engineering from the Mechanical Engineering Institute of the Federal University of Itajuba as a requirement to obtain the title of Ph.D. in Science in Mechanical Engineering.

Area of concentration: Design, Materials and Process.

Examining commission:
Prof. Dr. Luiz Claudio Pardini – ITA
Prof. Dr. Ricardo Mello Di Benedetto – UNESP
Prof. Dr. Bruno Silva de Sousa – UNIFEI
Prof. Dr. Yohan Alí Díaz Méndez – UNIFEI
Prof. Dr. Sebastião Simões da Cunha Júnior (co-advisor) – UNIFEI
Prof. Dr. Guilherme Ferreira Gomes (advisor) – UNIFEI

Itajubá – MG
2022

DINIZ, Camila Aparecida

Metamodel-based static and dynamic optimization of composite structures with ply drop-offs/ Camila Aparecida Diniz – Itajubá: UNIFEI, 2022.

146p.

Thesis (doctorate) – Federal University of Itajubá, 2022.

Advisor: Prof. Dr. Guilherme Ferreira Gomes

1. Ply drop-off – Optimization – Metamodel – Hybrid composites

I. Gomes, Guilherme F. II. Universidade Federal de Itajubá III. Metamodel-based static and dynamic optimization of composite structures with ply drop-offs.

Dedication

This work is especially dedicated to my family and friends, who encouraged and motivated me during this journey.

Acknowledgements

Firstly, I thank God for giving me strength to overcome the obstacles and challenges, making this dream possible.

My parents Maria Dolores and Milton, my sisters Denize and Laís and my husband Lucas, the loved once who have always supported me in all the moments with a lot of patience, love, and care.

Also, my godfather, Paulo Carvalho, and my dear aunt Helena Rhodus, who have always participated in my academic life.

To Professor Dr. Guilherme Ferreira Gomes for friendship, dedication, persistence, seriousness, and support during the development of this work, who shared the vast scientific knowledge, always with a lot of patience and expertise.

To Professor Dr. Sebastião Simões, my dear co-advisor, for the friendship, support, and expertise shared over all these years.

I would also like to thank my GEMEC and NTC colleagues for their help, knowledge sharing, and fun times at the UNIFEI.

Finally, I would like to thank CAPES for financial support and the Federal University of Itajubá for the great welcoming and learning opportunity.

"Education is not the learning of facts, but the training of the mind to think."

Albert Einstein

ABSTRACT

Nowadays, there is no analytical equation able to analyze the issues related to the performance of structures with ply drop-offs. In order to address this issue, a metamodel using Design of Experiments and the SunFlower Algorithm for static and dynamic optimization of composite structures with ply drop-offs was developed in this study. Through numerical simulations and experimental tests, a characterization of the static and dynamic behavior of tapered hybrid and non-hybrid tubes was proposed. Then, a metamodel was developed considering the results obtained through numerical simulations, where the best ply drop-off location that provides the best static and dynamic conditions was identified, and, posteriorly, it was applied in the manufacture of the tubes. The numerical results revealed that the hybrid tube reinforced with carbon and glass of fibers supported a high loading in buckling conditions when compared with non-hybrid tubes. Before the manufacture of the tubular structures, an experimental comparative study using honeycomb sandwich structures with different face sheets and cores was proposed to analyze the fabric characteristics. The results showed that the hybrid fabric reinforced with glass and aramid of fibers was demonstrated to be not viable for tubular structure manufacture. Then, in the manufacture of the tubular structures, the carbon, glass, and carbon/aramid hybrid fabrics were applied. The experimental results obtained with the optimized structures revealed that the hybridization provided an increase in the level of damping. The modal analyses performed on the intact and damaged structures demonstrated a smooth reduction in the first natural frequency and in the damping factor for the damaged structures. Aiming a comparative analysis between tapered and non-tapered structures, tubular structures without ply drop-offs were manufactured and experimental tests were performed. The hybrid tapered structure manufactured with carbon, aramid, and glass of fibers proved to be a promising option in compression conditions, supporting a loading of 9.489 kN, while the non-tapered structure supported a loading of 13.283 kN. In addition, this hybrid structure revealed a lower manufacturing cost when compared with the other hybrid structures, and it was considered lighter with a mass of 53 grams. The non-tapered hybrid structure had a mass of 77 grams, 30% higher than the tapered structure's mass. Therefore, metamodel-based static and dynamic optimization was demonstrated to be feasible and advantageous for determining the optimum ply drop-off location.

Keywords: *Ply drop-off; Optimization; Metamodel; Hybrid composites.*

RESUMO

Atualmente não existe uma equação analítica que seja capaz de analisar questões relacionadas ao desempenho de estruturas com *ply drop-offs*. Com intuito de suprir essa questão, um metamodelo usando Projeto de Experimentos e o algoritmo *SunFlower* para otimização do comportamento estático e dinâmico de estruturas com *ply drop-offs* foi proposto nesse estudo. Através de simulações numéricas e testes experimentais, uma caracterização sobre o comportamento estático e dinâmico de tubos escalonados híbridos e não híbridos foi proposta. Então, um metamodelo foi desenvolvido considerando os resultados obtidos com as simulações numéricas, onde a melhor localização para os *ply drop-offs* foi identificada e, posteriormente, esta localização ótima foi usada na manufatura dos tubos. Os resultados numéricos revelaram que o tubo híbrido reforçado com fibras de carbono e vidro suportou um maior carregamento em condições de flambagem quando comparado aos tubos não híbridos. Antes da manufatura dos tubos, um estudo comparativo experimental envolvendo estruturas sanduíches *honeycomb* considerando diferentes faces e núcleos foi desenvolvido com intuito de analisar as características de cada tecido aplicado na face das estruturas. Os resultados mostraram que o tecido híbrido reforçado com fibras de vidro e aramida não era viável na manufatura dos tubos. Então, para a manufatura das estruturas tubulares foram considerados os tecidos reforçados com fibras de carbono, vidro e carbono/aramida. Os resultados experimentais obtidos com as estruturas ótimas mostraram que a hibridização proporcionou um aumento no nível de amortecimento. As análises modais executadas com as estruturas intactas e danificadas demonstraram uma suave redução na primeira frequência natural e no fator de amortecimento para as estruturas danificadas. Então, estruturas tubulares sem drop-offs foram manufaturadas e testes experimentais foram realizados. A estrutura híbrida manufaturada com fibras de carbono, aramida e vidro provou ser uma opção promissora em condições de compressão, suportando um carregamento de 9,489 kN, enquanto a estrutura não escalonada suportou um carregamento de 13,283 kN. Além disso, essa estrutura foi considerada mais leve com massa de 53 gramas e revelou um custo de manufatura reduzido, quando comparado às outras estruturas híbridas. A estrutura híbrida não escalonada apresentou massa de 77 gramas, o que corresponde a uma massa 30% maior quando comparado à estrutura escalonada. Finalmente, o metamodelo baseado na otimização provou ser viável e vantajoso.

PALAVRAS-CHAVE: *Ply drop-off; Otimização; Metamodelo; Compósitos híbrido.*

TABLE OF CONTENTS

LIST OF FIGURES

LIST OF TABLES

LIST OF ABBREVIATIONS

ACO: Ant Colony Optimization

ANOVA: Analysis of variance

C: Carbon tube with ply drop-offs

CA: Carbon/aramid tube with ply drop-offs

CAC: Sandwich structure with carbon face and aramid core

CFRP: Carbon fiber-reinforced polymer

CP: Sandwich structure with carbon face and polypropylene core

DOE: Design of Experiments

FEM: Finite Element Method

FI: Failure index

FRF: Frequency response function

G: Glass tube with ply drop-offs

GA: Sandwich structure with glass face and aramid core

GFRP: Glass fiber-reinforced polymer

GP: Sandwich structure with glass face and polypropylene core

HCA: Sandwich structure with carbon and aramid hybrid face and aramid core

HCAG: Carbon, aramid and glass hybrid tube with ply drop-offs

HCG: Carbon and glass hybrid tube with ply drop-offs

HCP: Sandwich structure with carbon and aramid hybrid face and polypropylene core

HGA: Sandwich structure with glass and aramid hybrid face and aramid core

HGP: Sandwich structure with glass and aramid hybrid face and polypropylene core

LB: Lower bound

MO: Multiobjective optimization

PP: Polypropylene

PSO: Particle Swarm Optimization

RSM: Response surface methodology

SFO: SunFlower optimization

TW: Tsai-Wu failure criterion

UB: Upper bound

LIST OF SYMBOLS

Q	Amount of heat
θ	Angle for ply orientation [graus]
$\overline{N}_x, \overline{N}_y$	Axial and circumferential forces [N]
x,y,z	Axial, circumferential and radial coordinate directions [m]
u,v,w	Axial, circumferential and radial displacements [m]
$[D]$	Bending/torsion stiffness matrix
X^*	Best plantation
λ	Buckling load/bifurcation point [kN]
ϕ	Buckling mode shapes
N	Circumferential buckle waves
R^2	Coefficient of determination
D	Composite desirability function
F_s^{ult}	Core shear ultimate strength
$[B]$	Coupling stiffness matrix
X	Current plantation
R	Cylinder inner radius [mm]
η_r	Damping loss factor
ξ	Damping ratio
η	Damping value (loss factor)
ρ	Density [kg/m³]
$[K_d]$	Differential stiffness matrix
S_i	Direction of plants toward the sun
Δu	Displacement [m]
δ_{max}	Displacement [m]
r_i	Distance between the plant and the current best [m]
E_1	Elasticity modulus in the longitudinal direction [GPa]
E_2	Elasticity modulus in the transverse direction [GPa]
ΔE	Energy lost
B	Estimated coefficient
T	Facing thickness
N_x,N_y,N_{xy}	Forces resultants in the plane [N]
ω_a	half power point [rad/s]

ω_b	half power point [rad/s]
D	Individual desirability function
L	Length [m]
$[K]$	Linear stiffness matrix
ΔF	Load
M	Longitudinal buckle half waves
σ_1^C	Longitudinal compression strength [MPa]
σ_1	Longitudinal normal stress [MPa]
σ_1^T	Longitudinal tensile strength [MPa]
Mos	Margin of safety
F_{max}	Maximum load in bending [N]
P_{max}	Maximum load prior to the first failure in buckling [N]
σ_{max}	Maximum stress [MPa]
$[A]$	Membrane stiffness matrix
M_x,M_y,M_{xy}	Moment resultants [N.m]
ωn	Natural frequency [Hz]
k	Number of design parameters
N_{iter}	Number of iterations
N_p	Number of particles
N_{pop}	Number of plants
L_p	Longitudinal position
X_1	Panel position for first ply drop-off
X_2	Panel position for second ply drop-off
P_p	Ply position
Y_1	Ply position for first ply drop-off
Y_2	Ply position for second ply drop-off
υ_{12}	Poisson ratio
U_{max}	Potential energy at maximum displacement
R_c	Radius of creation
E	Random error term or noise
SR	Resistence factor
ω_r	Resonance frequencies [Hz]
Y	Response

G_{12}	Shear modulus in the 1-2 plane [GPa]
τ_{12}	Shear strength in the plane [MPa]
P	Source power
ε	Strain [mm/mm]
F	Strength parameters [MPa]
$[K_T]$	Tangent stiffness matrix
σ_2^C	Transverse compression strength [MPa]
σ_2	Transverse normal stress [MPa]
σ_2^T	Transverse tensile strength [MPa]
TW_c	Tsai-Wu failure criterion in compression
TW_t	Tsai-Wu failure criterion in torsion

CHAPTER 1: INTRODUCTION

Recently, tubular composite structures have been extensively studied and used in various applications, such as wind turbine blades, sailing ships, pressure vessels, and fuel ducts in aircraft, among others, and have recently drawn attention to the prosthetic industry. In the literature, some relevant applications of tubular structures manufactured with composite material are: *i)* oil and gas , *ii)* automotive, *iii)* in pylon structures for lower limb prostheses, *iv)* aircraft, *v)* in vehicle frames for energy absorption, and *vi)* bicycles (DINIZ *et al.* 2019; YANG *et al.* 2020; AMAECHI *et al.* 2022), as can be seen in Figure 1.1.

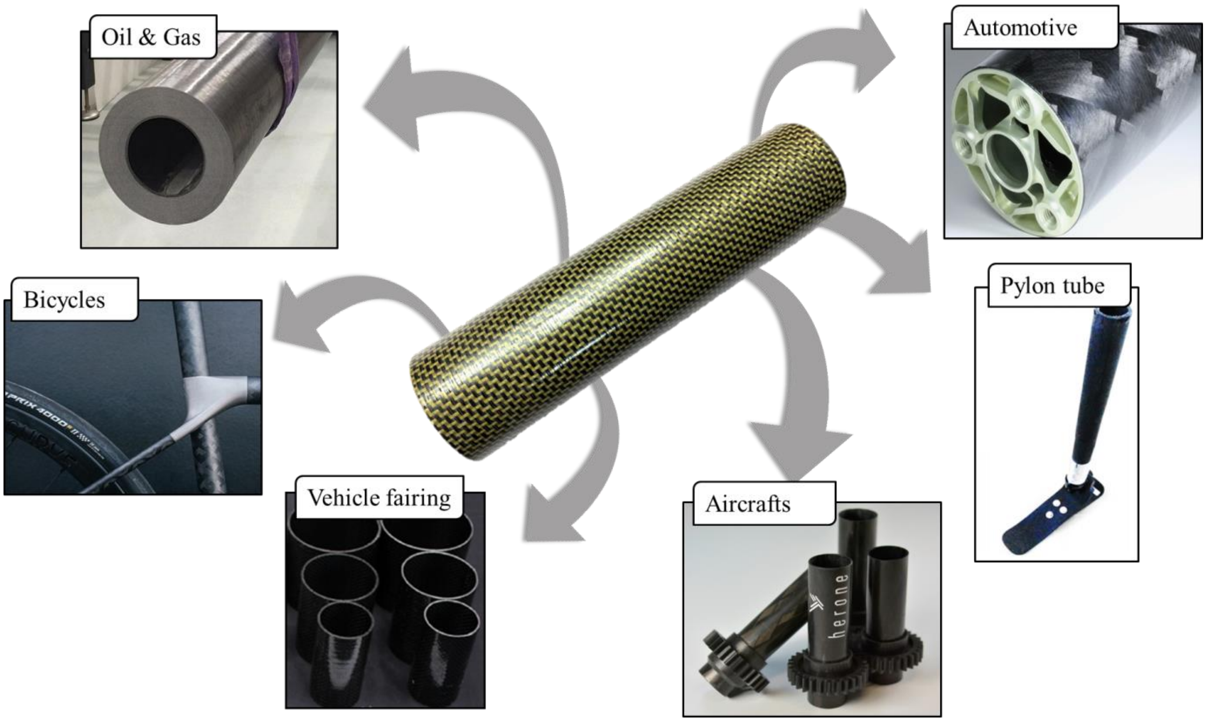

Figure 1.1 – Different application for tubular structures manufactured in composite material (adapted from GOMES *et al.* 2017; YANG *et al.* 2020; AMAECHI *et al.* 2022).

The use of composite materials in tubular structures is very attractive and advantageous thanks to their high structural performance characterized by lightweight, high strength and stiffness, superior energy-absorbing capacity, high fatigue resistance, and excellent design flexibility (FITRIAH *et al.* 2017; ZHAO *et al.* 2019). Zhao *et al.* (2019) report that the use of thin-walled tubular structures for crashworthy applications provides both fuel economics and high security in relation to crashes when compared with tubular structures manufactured in metal.

At present, hybrid configurations for tubular structures are gaining increasing interest in modern industry to provide the combination of two or more different fibers in a single matrix, aiming to provide versatile properties and reduce material cost (LI *et al.* 2020). Ravishankar *et al.* (2019) affirm that hybrid composite materials are applicable in several engineering fields due to their lightweight, low cost, high strength, and ease of manufacturing methods. In addition to the hybridization involving tubular composite structures, an efficient alternative frequently used in the aerospace industry to reduce the mass and, consequently, the cost of material is the dropping-off of plies along the length of the laminate, known as ply drop-off or tapered. The ply drop-off allows the reduction of the laminate thickness by dropping plies at different locations in relation to their length (LIU *et al.* 2018).

A common composite structure with ply drop-off is divided into several panels (longitudinal direction) with stacked plies (transversal direction), as shown in Figure 1.2 (VIDYASHANKAR and MURTY, 2001).

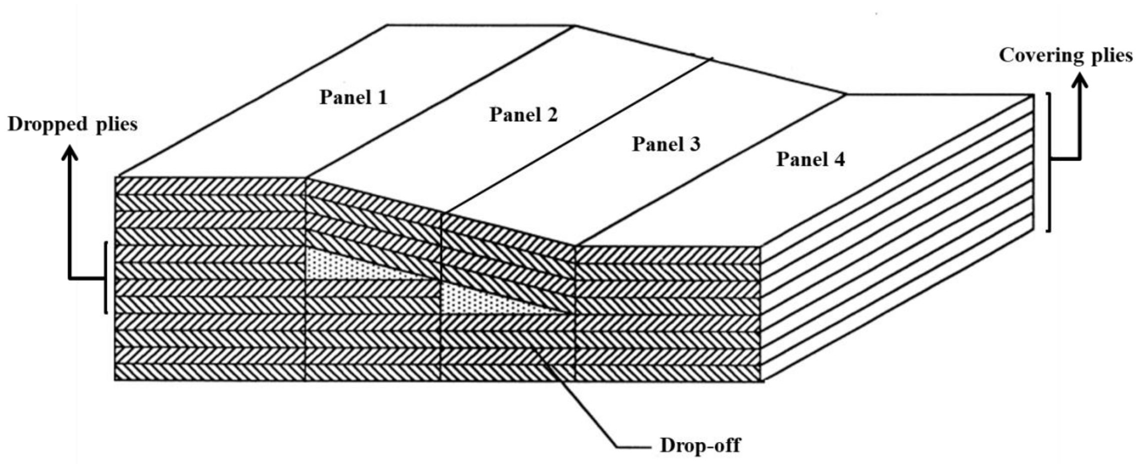

Figure 1.2 – Nomenclature of a structure with 2 ply drop-offs composed of 4 panels and 12 plies in total (adapted from VIDYASHANKAR and MURTY, 2001).

For a typical laminate with ply drop-off, it is possible to consider two main variables responsible for ply drop-off location related to the ply that should be dropped and which panel this ply is located. Then, it is possible to conclude that the main variables that describe the ply drop-off location are ply (vertical position) and panel (longitudinal position). For example, in the Figure 1.2, the first ply drop-off was located by dropping the fifth and sixth plies on the second panel.

According to Dhurvey and Mittal (2013), tapered stuctures present a high capacity for structural adaption, damage tolerance, and reduced mass in various engineering applications. The most significant concern is related to the manufacturing parameters for this type of structure because the dropping-off of the plies can cause the concentration of stresses in the region near the ply drop-off and failures that directly affect the structural performance. Meanwhile, depending on the ply drop-off location, these unwanted situations can be controlled or reduced. In the literature, it is possible to find some authors that describe the main difficulties and precautions associated with the use of structures with ply drop-offs (IRISARRI *et al.* 2014; NASAB *et al.* 2018; ZENG *et al.* 2019).

Therefore, this study proposes a metamodel based on static and dynamic behavior of tapered structures aiming at the best ply drop-off location. For the development of the metamodel, numerical and statistical methods are applied, and, posteriorly, experimental tests are performed considering laminate and sandwich composite structures.

1.1 Research Objectives

1.1.1 General objective

The main objective of this work is to develop metamodel-based static and dynamic behavior of laminate composites (planar and tubular) to determine the optimum ply drop-off location by means of numerical-experimental evaluations aiming at increase structural performance.

1.1.2 Specific objectives

The optimum design of tapered structures is analyzed through the following steps:

- Based on numerical analyses, develop a metamodel using the Response surface methodology to know the best ply drop-off location and the impact caused by tapering in the properties related to the failure criterion, strain, and first natural frequency of a planar structure;

- Propose an optimization strategy using a metamodel obtained through design of experiments and the SunFlower algorithm to determine the better ply drop-off location, aiming to minimize the failure criterion with the mass and maximize the first natural frequency and buckling load of hybrid and non-hybrid tubular structures, considering numerical analyses;
- Develop a singular study of characterization through experimental tests on four different types of fabrics for future applications in tubular structures, considering modal, bending, and buckling conditions;
- Manufacture tapered tubular structures with the material recommended in the characterization study, considering the optimum ply drop-off location and performing compression and modal experimental tests to prove the feasibility and advantages of the optimized tapered tubular structure;
- Manufacture non-tapered structures with the same setup used in the tapered tubular structures, encouraging a comparative study about the feasibility and advantages of the use of drop-offs.

1.2 Justification for Research

The use of tapered composite structures is growing, and therefore the necessity of robust designs with this type of structure is expanding. According to Shim (2002), the main difficulties encountered in researches involving tapered structures are: *i)* the large number of ply drop-off locations in a single structure; and *ii)* the influence that the ply drop-off location has on the strength of the laminate composite. It can be affirmed that the ply drop-off location is a key question in any analysis involving tapered laminate structure.

The composite material with ply drop-off has been very useful in planar structures, as is the case of applications in the aeronautical industry (PANETTIERI *et al.* 2019; SHRIVASTAVA *et al.* 2019; KAPPEL, 2019) and the wind industry (NASAB *et al.* 2018; ALBANESI *et al.* 2018a; SJØLUND *et al.* 2019). However, studies considering applications of ply drop-off in hybrid tubular structures are limited and poorly explored. In addition, there are a few studies considering tapered structures in buckling situations. Dhurvey and Mittal (2013) assert that buckling and vibration analyses involving laminate structures with ply drop-off are limited in the literature, which may increase interest in the research.

It is very common to use statistical methods in studies with composite materials (GHASEMI *et al.* 2016; NARESH *et al.* 2018; KUMAR and RAJMOHAN, 2019; ADAMU *et al.* 2019; BAKHTIARI *et al.* 2020). Nonetheless, optimization studies of tapered laminate composites involving metamodels based on statistical methods, such as design of experiments, are unusual. Therefore, this study continues to encourage many other researches.

In that way, with the metamodel based on statistical methods, the SunFlower algorithm, and numerical and experimental analyses, it is expected to supply the scarcity of research in this field and contribute to the use of tapered tubular structures of high performance in various engineering applications.

1.3 State of the Art

In recent decades, the search for high-performance materials, such as composite materials, has had a great expansion. Due to its many advantages, this material has become an attractive material for many industries that have started to design and manufacture their structures using composite materials (GOMES *et al.* 2018; XU *et al.* 2018; ARTEIRO *et al.* 2020).

In the mid-1980s, the aeronautical industry started to develop a new technique for application in laminate composite structures, known as ply drop-off. The main aims were to reduce the thickness and mass through structural tapering and improve the structural performance. Meanwhile, the impacts of the tapered on the structures were unknown and poorly studied, which made the manufacture of these structures more complex and their structural integrity affected. Cairns *et al.* (1999) studied the damage and delamination effects in tapered structures considering some parameters, such as thickness, stacking sequence, ply drop-off geometry, and manufacturing conditions. The authors concluded that thick laminates are stronger to delamination, the dropping of more than one ply in the same panel increases the risk of delamination on the laminate, and internal ply drop-offs are less favorable to delamination when compared with external ply drop-offs.

In the meantime, optimization strategies aimed to optimal designs for structures with ply drop-off have emerged. Kristinsdottir *et al.* (2001) elaborated an optimization study about manufacturing conditions for structures with ply drop-offs using blending rules that recommend continues plies on the upper and bottom laminate surface with the intention of avoiding external ply drop-offs. The use of these rules provided a simple manufacturing process for the tapered structure. Additionally, Irisarri *et al.* (2014) proposed a simultaneous optimization of the fiber angle distribution and ply drop-off location in laminate structures. The authors proposed new rules for the use of ply drop-offs based on analyses and tests perfomed by the industry. These rules have the intention of avoiding delamination and propagation of cracks, and aim to preserve the structural integrity and ensure manufacturing conditions. Sudhagar *et al.* (2017) developed a structural optimization to obtain the appropriate sequence and orientation plies of tapered laminate plates using the Finite element method (FEM) and Genetic algorithm (GA), aiming to maximize the first natural frequency and damping factor. The authors noted that the natural frequencies increased with all plies oriented to 90º. While doing that, Albanesi *et al.* (2018b) elaborated a novel methodology using GA with the inverse FEM to determine the optimal ply drop-off configuration of laminate wind turbine blades minimizing the mass. The design variables were the initial and final location of the plies on the structure, considering as constraints the deflection, maximum stress, and natural frequencies. The results showed that the mass could be reduced by 15% with the optimal ply drop-off design. Lund (2018) performed an optimization strategy for tapered laminates, including minimizing the failure index (FI) and structural mass. For this, the constraints applied considered buckling conditions, laminate strength, structural displacement, and natural frequencies. The authors affirmed that the most significant factors for tapered structures are the thickness, plies stacking sequence, ply drop-off geometry, and manufacturing conditions. Shrivastava *et al.* (2019) proposed an optimization study of tapered wing panels using heuristic method to determine the best ply drop-off location on the structures. The multiobjective optimization considered the Tsai-Wu failure index and safety margin. The use of ply drop-offs on the structure generated a significant reduction in mass with a positive safety margin. Moreover, the algorithm was able to determine the ideal tapered end.

As it was possible to notice, many studies involving tapered structures consider the stacking sequence as the main design variable to determine the optimal mechanical properties of tapered structures. However, there are other parameters poorly explored that also have an influence on the ply drop-off location, such as which plies should be dropped and in which panel or longitudinal direction. It was also noted that many researchers prefer evolucionary algorithms in conjunction with FEM for optimizing structures with ply drop-offs (PEETERS and ABDALLA, 2016; MUC, 2018; VEMULURI *et al.* 2018; ZHAO and KAPANIA, 2018; SANZ-CORRETGE, 2019). Despite this, Sanz-Corretge (2019) emphasizes that evolutionary algorithms such as GA must be run many times to generate consolidated solutions, which entails a high computational cost. For this reason, An *et al.* (2019) suggest the use of approximation concepts such as the Response surface methodology (RSM) to reduce the computational cost.

To the best of the author's knowledge, very few efforts have been devoted to metamodel based on ply drop-off location optimization for tubular stuctures. Metamodelling using statistical methods in association with numerical and experimental tests for optimization of tapered tubular structures is considered scarce in the literature. Therefore, this research topic is seen as innovative and promising.

1.4 Thesis Outline

The following thesis is divided into five Chapters.

In Chapter 2, the background theoretical about the guidelines for laminate structures with ply drop-offs, Design of experiments, the SunFlower algorithm, failure criterion, buckling analyses, and modal analysis are presented.

In Chapter 3, the methodology developed in this study is proposed.

In Chapter 4, the results are drawn and discussed.

Finally, the conclusions, publications, and suggestions for future works are presented in Chapter 5.

(Intentionally left blank)

CHAPTER 2: THEORETICAL BACKGROUND

2.1 Main Design Guidelines for Structures with Ply Drop-offs

A typical laminate composite with ply drop-off presents a thick panel formed by all plies, a thin panel composed by uninterrupted plies, a taper angle created by the dropping of plies and a taper section where the ply drop-offs are located, as depicted in Figure 2.1 (IRISARRI *et al.* 2014).

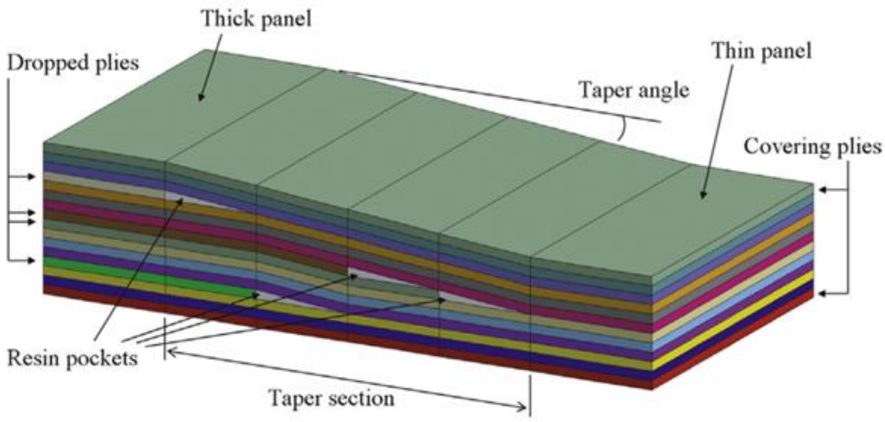

Figure 2.1 – Nomenclature used in structures with ply drop-offs (taken from IRISARRI *et al.* 2014).

It can be noted in Figure 2.1 that the laminate is longitudinally fragmented into panels or zones (x-axis) and transversely comprised of a ply stacking sequence (z-axis). When a ply is dropped, theoretically, voids are generated and can be filled with resin. For this reason, the region near the ply drop-off is also known as resin pockets (VIDYASHANKAR and MURTY, 2001).

The implementation of ply drop-offs on a structure is not trivial. Indeed, it may be considered quite complex because the discontinuity between plies may impose difficulties relative to the stress concentration in the vicinity of the ply drop-off, as well as possible premature failures such as delamination, matrix cracking, and fiber fractures (MUKHERJEE and VARUGHESE, 2001; WEISS *et al.* 2010). To avoid these unwanted situations, guidelines for the manufacture of structures with ply drop-off arising from industrial knowledge were elaborated. Some of these guidelines are exposed and considered in this work. Other rules can be found in Irisarri *et al.* (2014):

- Symmetry: the symmetric stacking sequence should be centered on the midplane;
- Balance: where the stacking sequence differs from 0º and 90º, it should be balanced with the same number of $+\theta$ and $-\theta$ plies;
- Damtol: on the lower and upper surfaces of the laminate, it is not permitted to have oriented plies 0º ;
- Covering: plies in the lower and upper surfaces should not be dropped;
- Max-stopping: it is not accepted that more than two plies stops at the same panel;
- Maximum taper slope: the taper angle should not be greater than 7º.

These guidelines provide structural integrity and manufacturing conditions for tapered structures. In addition to these guidelines, Weiss *et al.* (2010) suggest that it not be dropped many plies on the same panel because of the static strength, which could lead to the delamination of the structure.

2.2 Design of Experiments

Design of Experiments (DOE) is a common statistical method widely used in several analyses. It refers to an experiment planning process in which a suitable data set is collected and examined for the purpose of providing meaningful conclusions (MONTGOMERY, 2017). This method comprises several techniques, such as factorial design, the RSM, and the Taguchi method, which depend on the process characteristics and responses that will be analyzed.

2.2.1 Factorial design

Full factorial design is a strategy capable of estimating the main effects and their interactions in an experiment as well as allowing the verification of the presence of quadratic terms. The effects are measured through the change in response caused by modifying the levels of the factors, as depicted in Figure 2.2 (MONTGOMERY, 2017). Thus, it becomes possible to distinguish the relevance among the factors that influence the response and define the experiments that will be done.

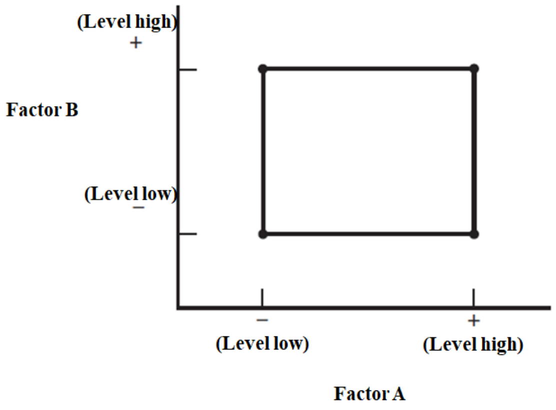

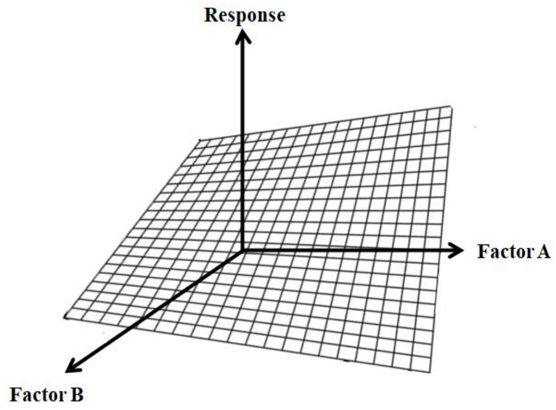

Figure 2.2 – Full factorial experiment: (a) Considering two factors and (b) considering two factors and one response (MONTGOMERY, 2017).

The factorial design can be described by a linear regression model, as shown in Equation 2.1 (MONTGOMERY, 2017).

$$y=\beta_0+\beta_1 x_1+\beta_2 x_2+\beta_{12} x_1 x_2+e \tag{2.1}$$

where y and β are the response and estimated coefficients, respectively, x_1 and x_2 are the design variables, and e is the random error term.

To examine the factorial design, Analysis of Variance (ANOVA) tests are often performed, which, by comparison between the mean variances, determine the difference in a set of means and study the quality of the fit, establishing a regression model for the system. The ANOVA analyzes the variables through a *p-value* that is defined as the probability of observing a given value of the test statistic. Traditionally, a *p-value* less than 0.05 represents that there is a statistically significant difference between the means of the groups composed by the response and design variables. Now, if the *p-value* is not less than 0.05, it is possible to conclude that there is not sufficient evidence to affirm that there is a statistically significant difference between the means of the groups. (MONTGOMERY *et al.* 2012).

The quality of fit is measured by adjusting the coefficient of determination (R^2_{adj}), which demonstrates how well the model is fitted to the data, in addition to determining the predictive capability of the regression model. The R^2_{adj} value ranged from 0 to 100. The closer the coefficient of determination is to 100, the better the model is suited to the data. A model with an R^2_{adj} of above 80% is already considered appropriate, revealing that it explains the variability of the fitted data (MONTGOMERY *et al.* 2012).

2.2.2 Response surface methodology

The RSM is a mathematical and statistical technique based on fitting a second-order Equation that describes the behavior of a data-set. First, one must obtain a suitable first-order approximation function between design and response variables. However, if the system reveals a curvature, it is necessary to use a second-order model represented by the RSM, as shown in Equation 2.2 (MONTGOMERY, 2017).

$$y=\beta_0+\sum_{i=1}^{k}\beta_i x_i+\sum_{i=1}^{k}\beta_{ii}x_i^2+\sum_{i<j}0\sum\beta_{ij}x_i x_j+e \tag{2.2}$$

where k represents the number of design parameters.

The main differences between the factorial design and RSM are the inclusion of the quadratic terms that are responsible for the level of the variables and optimization of the responses (MONTGOMERY, 2017).

A typical RSM considers a complete quadratic model, which, in this case, is constituted of two design factors related to the ply drop-off location considering the panel and ply positions, as shown in Figure 2.3a. In Figure 2.3b is depicted a 3D plot of the factors in relation to the fitted response surface.

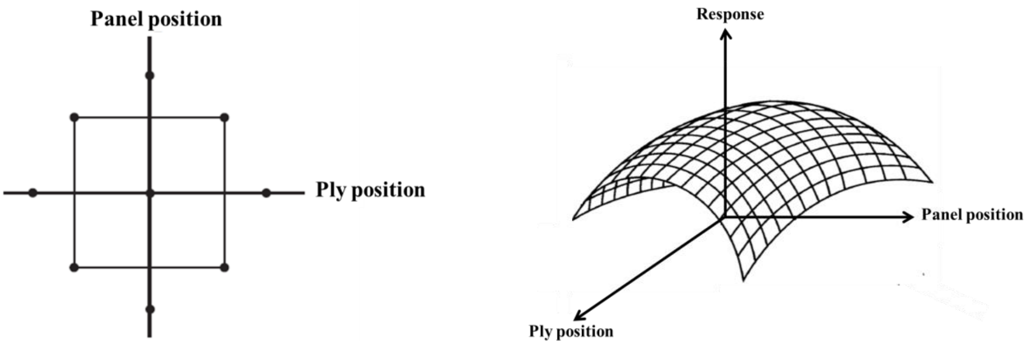

(a) (b)

Figure 2.3 – Typical response surface: (a) Central composite design and (b) three-dimensional (MONTGOMERY, 2017).

The optimization strategy developed with the RSM applies the desirability function, in which response values are restricted to one and indicated by individual desirability functions (*d*) ranging from 0, for an undesirable response, to 1, for a fully desired response, creating the composite desirability function (*D*) defined by Equation 2.3 (MYERS *et al.* 2009).

$$D=(d_1 x d_2 x d_3 ... x d_n)^{1/n} = \left(\prod_{i=1}^{n} d_i\right)^{1/n} \tag{2.3}$$

where d_i represents the desirability considering each output response and n is the number of responses.

2.3 SunFlower Optimization Algorithm

Many algorithms began to build upon from GA, such as Particle Swarm Optimization (PSO), Ant Colony Optimization (ACO), and currently, SunFlower Optimization (SFO). This new algorithm created by Gomes *et al.* (2019) has already been used in many studies (QAIS *et al.* 2019; YUAN *et al.* 2020; GOMES *et al.* 2020). The algorithm is based on the behavior of sunflowers in the search for the sun during the day. At night, the sunflowers follow the opposite direction to wait again the next morning. The pollination process is considered to take place randomly along the minimal distance between the flower *i* and the flower *i*+1. Aiming for a fast solution in the optimization, the algorithm considers that each sunflower only produces one pollen gamete and reproduces individually, unlike in the real world where each flower patch often release millions of pollen gametes. In addition to this, the optimization process is based on inverse square law radiation, where the intensity of the radiation is inversely proportional to the square of the increase distance, such that the radiation intensity value reduces in proportion to the square of the increase in distance. The main objective of the algorithm is to minimize the distance between the plant and the sun, if the distance between sunflowers and the sun increases, the radiation intensity will decrease, making them less likely to achieve the vicinity of the global optimum (sun). The amount of heat Q received by each plant is depicted by Equation 2.4.

$$Q_i = \frac{P}{4\pi r_i^2} \tag{2.4}$$

where P represents the source power and r_i the distance between the plant and the current best.

The mathematical model of the sunflower's direction to the sun is given by:

$$\vec{S_i} = \frac{X^* - X_i}{\|X^* - X_i\|}, \quad i = 1, 2, \ldots, n_p, \tag{2.5}$$

where X^* and X represent the best plantation and the current plantation, respectively.

The step of the sunflowers in the direction s is depicted in Equation 2.6:

$$d_i = \lambda x P_i(\|X_i - X_{i+1}\|) x (\|X_i - X_{i+1}\|), \tag{2.6}$$

where λ is the constant value that defines the inertial displacement of the plants and $P_i(\|X_i - X_{i+1}\|)$ represents the pollination probability. The candidates closer to the sun will take smaller steps, while the more distant candidates will move normally. In order not to skip favorable regions in order to be a global minimum candidate, the maximum step for each individual is achieved by Equation 2.7:

$$d_{max} = \frac{\|X_{max} - X_{min}\|}{2xN_{pop}} \tag{2.7}$$

where X_{max} and X_{min} are the upper and lower bounds values, and N_{pop} is the total number of plants.

The new plantation is given by Equation 2.8:

$$\overrightarrow{X_{i+1}}=\overrightarrow{X_i}+d_i x \overrightarrow{S_i} \tag{2.8}$$

The SFO considers the main three biological operators: *i)* Pollination rate, which defines the percentage of the population who will pollinate, *ii)* survival rate corresponds to the sunflowers that move toward the sun, and *iii)* mortality rate represents the percentage of sunflowers that do not survive because they are further from the sun.

In summary, the SFO begins with the generation of a population of individuals. Afterward, the entire population is assessed, and then the individual with the best evaluation among all will be transformed into the sun. The rest of the individuals will be guided by the individual chosen as the sun. Once sunflowers are oriented toward the sun, they will reproduce and move toward the optimal point.

2.4 Tsai-Wu Failure Criterion

The Failure criteria have been elaborated to detect failures through the estimation of effects caused by efforts applied to a structure. The failure analysis may become quite complex for composite materials due to the anisotropy. The Tsai-Wu failure criterion is considered very appropriate due to approximation with experimental data for analysis of the failure mechanisms (TSAI and WU, 1971). With knowledge about strength parameters and stresses, it is possible to establish whether the structure will fail or not using the Tsai-Wu failure criterion, whereby a failure occurs in the structure if Equation 2.9 is violated (VOYIADJIS and KATTAN, 2005):

$$F_{11}\sigma_1^2+F_{22}\sigma_2^2+F_{66}\tau_{12}^2+F_1\sigma_1+F_2\sigma_2+F_{12}\sigma_1\sigma_2\leq 1 \tag{2.9}$$

where F_{11}, F_{22}, F_{66}, F_1, F_2, F_{12} are the strength parameters and σ_1, σ_2, τ_{12} are the stresses (normal and shear).

The strength parameters are responsible for differentiating the tensile and compression stresses, as depicted in Equation 2.10 – 2.14 (VOYIADJIS and KATTAN, 2005):

$$F_{11}=\frac{1}{\sigma_1^T\sigma_1^C} \tag{2.10}$$

$$F_{22}=\frac{1}{\sigma_2^T\sigma_2^C} \tag{2.11}$$

$$F_1=\frac{1}{\sigma_1^T}-\frac{1}{\sigma_1^C} \tag{2.12}$$

$$F_2=\frac{1}{\sigma_2^T}-\frac{1}{\sigma_2^C} \tag{2.13}$$

$$F_{66}=\frac{1}{(\tau_{12}^F)^2} \tag{2.14}$$

The F_{12} constant can be obtained by the Equation 2.15 based on experimental tests (TSAI and HAN, 1980).

$$F_{12}=-\frac{1}{2}\left[\frac{1}{\sigma_1^T\sigma_1^C\sigma_2^T\sigma_2^C}\right]^{1/2} \tag{2.15}$$

The safety margin provides the additional loading value that is supported by the structure, in addition to the loading applied. A positive safety margin indicates how many times the structure bears the loading applied initially (CAMPBELL, 2010). With knowledge of the resistance factor (SR), the safety margin can be obtained by Equation 2.16:

$$MoS = SR-1 \tag{2.16}$$

where *SR* represents the resistance factor, and it can be obtained by Equation 2.17 considering the failure index (*FI*):

$$SR=\frac{1}{FI} \tag{2.17}$$

2.5 Linear and Nonlinear Buckling Analysis

2.5.1 Analytical buckling model

Buckling is a loss of stability caused by geometric effects, material chacteristics, and boundary conditions. When the buckling is not controlled, it can lead to material failure and even structure collapse (BARBERO, 2014).

According to Bisagni (2005), the investigated buckling in linear conditions considers the effects of the initial geometry imperfections and stacking sequence. However, the buckling under non-linear conditions was demonstrated to be more complex due to the loss of stability or deformations in an unlimited extension.

For the study of the buckling in the tubular composite material, it is necessary to consider stresses and strains based on the Classical laminate theory (CLT) as proposed by Jones (1968), where a variation of the stresses generates modification in the moments and forces. Posteriorly, Perry *et al*. (1992) included in the classical solution the stability differential Equation for cylindrical shells under axial compression and circumferential loading, as shown in Equations 2.18 - 2.21.

$$\begin{bmatrix} N \\ M \end{bmatrix} = \begin{bmatrix} A & B \\ B & D \end{bmatrix} \begin{bmatrix} \varepsilon \\ k \end{bmatrix} \tag{2.18}$$

$$\delta N_{x,x}+\delta N_{xy,y}=0 \tag{2.19}$$

$$\delta N_{xy,x}+\delta N_{y,y}=0 \tag{2.20}$$

$$\frac{\delta N_y}{R}-\delta M_{x,xx}+\delta M_{xy,y}-\delta M_{xy,xy}-\delta M_{y,yy}+\delta \overline{N}_x w_{,xx}+\delta \overline{N}_{xy} w_{,yy}=0 \tag{2.21}$$

where A, B and D are components of the stiffness matrix, δ is the variation of the components, N_x and N_y are active forces in the plane, while $\overline{N}_x$ and $\overline{N}_y$ are resultant forces in compression and circumferential loading, respectively.

Therefore, the resulting Equations that satisfy the boundary conditions are established by applying the displacement and buckling functions. Assumptions based on Equation 2.21 can be assumed in Equation 2.22.

$$\delta N_y = v = w = \delta M_x = 0 \tag{2.22}$$

where:

$$v = \sum_{m=1}^{\infty}\sum_{n=1}^{\infty} \bar{v}_{mn} sin\left(\frac{m\pi x}{L}\right) sin\left(\frac{ny}{R}\right)_0 \tag{2.23}$$

$$w = \sum_{m=1}^{\infty}\sum_{n=1}^{\infty} \bar{w}_{mn} sin\left(\frac{m\pi x}{L}\right) cos\left(\frac{ny}{R}\right) \tag{2.24}$$

The axial displacement can be obtained from Equation 2.25:

$$u = \sum_{m=1}^{\infty}\sum_{n=1}^{\infty} \bar{u}_{mn} cos\left(\frac{m\pi x}{L}\right) cos\left(\frac{ny}{R}\right) \tag{2.25}$$

where $\bar{v}_{mn}$, $\bar{w}_{mn}$ and $\bar{u}_{mn}$ are the amplitudes of the buckling displacement.

According to Jones (1968), the displacement functions as pure modes considering a particular m (longitudinal buckle half waves) and n (circumferential buckle waves), extracting the summation signs and refusing the coupled mode shapes between bending and extension. For the purpose of obtaining a nontrivial solution, the results of Equations 2.23 to 2.25 for the determination of amplitude coefficients must be zero. Thus, the derived solution for a clamped-free composite cylinder is obtained by Equation 2.26:

$$\lambda = \frac{1}{k_1\left(\frac{n}{R}\right)^2 + k_2\left(\frac{m\pi}{L}\right)^2} - \frac{\begin{bmatrix} F_{11} & F_{12} & F_{16} \\ F_{21} & F_{22} & F_{26} \\ F_{61} & F_{62} & F_{66} \end{bmatrix}}{\begin{bmatrix} F_{11} & F_{12} \\ F_{21} & F_{22} \end{bmatrix}} \tag{2.26}$$

where:

$$\bar{N}_y = k_1\lambda \quad \text{and} \quad \bar{N}_x = k_2\lambda \tag{2.27}$$

$$F_{11}=A_{11}\left(\frac{m\pi}{L}\right)^2+A_{66}\left(\frac{n}{R}\right)^2 \tag{2.28}$$

$$F_{12}=F_{21}=(A_{12}+A_{66})\left(\frac{m\pi}{L}\right)\left(\frac{n}{R}\right) \tag{2.29}$$

$$F_{16}=F_{61}=\frac{A_{12}}{R}\frac{m\pi}{L}+B_{11}\left(\frac{m\pi}{L}\right)^3\left(\frac{n}{R}\right)^2 \tag{2.30}$$

$$F_{22}=A_{22}\left(\frac{n}{R}\right)^2+A_{66}\left(\frac{m\pi}{L}\right)^2 \tag{2.31}$$

$$F_{26}=F_{62}=A_{22}\left(\frac{n}{R^2}\right)+(B_{12}+2B_{66})\left(\frac{m\pi}{L}\right)^2\left(\frac{n}{R}\right)+B_{22}\left(\frac{n}{R}\right)^3 \tag{2.32}$$

$$F_{66}=D_{11}\left(\frac{m\pi}{L}\right)^4+2(D_{12}+2D_{66})\left(\frac{m\pi}{L}\right)^2\left(\frac{n}{R}\right)^2+D_{22}\left(\frac{n}{R}\right)^4+\frac{A_{22}}{R^2}+2\frac{B_{22}}{R}\left(\frac{n}{R}\right)^2+2\frac{B_{12}}{R}\left(\frac{m\pi}{L}\right)^2 \tag{2.33}$$

In this case, the buckling load is obtained from Equation 2.26, where k_1 is considered null and, consequently, $\overline{N}_y$ is equal to zero. Hence, it is necessary to solve only $\overline{N}_x$. However, if the case requires a buckling load for the cylinder under lateral pressure, the opposite should be done, $\overline{N}_x$ must be equal to zero and $\overline{N}_y$ must be resolved (JONES, 1968). This solution is valid for thin cylinders due to being based on CLT with an emphasis on the Thin-Shell Theory. For thicker tubes, the Higher Order Theory is required.

Therefore, the buckling state for slender structures can be achieved with a slight increase in the deformation along with a decrease in the applied loading.

2.5.2 Numerical buckling model

The linear buckling analysis is able to reveal the buckling load or bifurcation point for perfect structures with small deformations, providing more conservative results. For structures with large deformations, it is recommended to use nonlinear analysis because the structures suffer geometric modifications and consequently respond non-linearly (BISAGNI, 2005; ONKAR, 2019). Using the FEM, the linear buckling analysis is considered simpler and has a low computational cost (BISAGNI, 2005).

The linear buckling analysis is more useful for estimating the theoretical buckling load that will be used as the convergence criterion in the nonlinear buckling analysis. In the FEM, to determine the linear buckling load, it is necessary to encompass the effect of the differential stiffness into the linear stiffness matrix. Mathematically, the Eigenvalue analysis is required, as shown in Equation 2.34 (BISAGNI, 2005).

$$([K]+\lambda[K_d])\{\phi\}=\{0\} \tag{2.34}$$

where $[K]$ indicates the linear stiffness matrix, $[K_d]$ the differential stiffness matrix, the ϕ represents buckling mode shapes (eigenvector) and λ is the eigenvalue of the system. When the load applied to the structure is unitary, the eigenvalue can be considered as the bifurcation point. The nonlinear buckling analysis is used to achieve realistic results in which the critical load is set out by a progressive increase in the applied load until the structure becomes unstable.

When the stability of a limited elastic system subject to a conservative loading is lost, the linear stiffness matrix $[K]$ becomes singular and symmetrical. Then, the nonlinear buckling load can be found using Equation 2.35:

$$K_T(u)\Delta u\text{-}\Delta F(u)=\{0\} \tag{2.35}$$

where K_T represents the tangent stiffness matrix, (u) is the increment step, Δu and ΔF are, respectively, the displacement and the load.

As the nonlinear buckling analysis considers the linear critical load as a convergence criterion, its value must always be less than the linear buckling load. Then, a previous analysis of linear buckling is required to begin the nonlinear buckling analysis (BISAGNI, 2005).

2.6 Modal Testing

To understand the dynamic behavior of structures subject to different design conditions, dynamic characteristics like frequency, damping, and mode shapes need to be better known. Modal analysis studies the dynamic responses of a system when subjected to applied loads, where each mode has its own frequency, damping factor, and specific deformation. The natural frequency is represented by a frequency that vibrates the system without external forces after a disturbance (RAO and GRIFFIN, 2018). Due to system damping, declines are observed in the oscillating response. The damping causes energy losses in the system, which is measured by a loss factor or a loss coefficient (η), as shown in Equation 2.36 (INMAN, 2014).

$$\eta = \frac{\Delta E}{2\pi U_{max}} \tag{2.36}$$

where ΔE is the energy lost per radian and U_{max} is the potential energy at maximum displacement.

In experimental modal analyses, the vibration responses are computed by a laser vibrometer, a system of noncontact testing that obtains data of velocity over time that is converted to the frequency domain to calculate, posteriorly, the frequency response function (FRF). The FRFs are responsible for the relationship between the applied disturbance and the output response caused by this disturbance. A common method for analyzing FRF is Peak-Amplitude, for which all the responses can be assigned using one mode, disregarding the effects of other modes (EWINS, 2000). In this method, the modes are well-separated in FRF analysis, where the natural frequencies are calculated using peaks on the FRF magnitude plot, which are confirmed as resonant frequencies (ω_r). The local maximums are used to define two points (‘*a*’ and ‘*b*’) known as half-power points, then ω_a and ω_b are the frequencies of the *a* and *b* points. Finally, the loss factor (η_r) can be calculated in Equation 2.37.

$$\eta_r = \frac{\omega_a^2 - \omega_b^2}{2\omega_r^2} \tag{2.37}$$

It is evident that the noise in the measured FRF data is not considered in this method. The peak-picking method is recommended for FRF data, which presents distinct modes and appropriate frequency resolution (HEYLEN *et al.* 1997).

CHAPTER 3: MATERIALS AND METHODOLOGY

3.1 Numerical Modelling Using Finite Element Method

3.1.1 Cantilever beam with ply drop-offs

Initial analysis considered a laminate beam with 8 stacked plies having any of these plies dropped. Table 3.1 and Figure 3.1 present the geometric parameters considered for numerical analyses. Due to symmetry, it was considered a total of 16 stacked plies and 2 ply drop-offs on the structure. In a simulation, the laminate beam with ply drop-offs was subjected to a constant force evenly distributed on the central line of the thin end, creating a compression condition. The other end of the beam was clamped, restricting movements of translation and rotation in all directions, as shown in Figure 3.1. The numerical simulations were performed in an engineering computational program that considered two types of analyses: a static one for the response to strain and failure criterion, and another modal in search of the natural frequency response.

Table 3.1 – Geometric parameters for a cantilever beam with ply drop-offs.

Geometric parameters	Value
Length [m]	0.15
Width [m]	0.03
Amount of panels	8
Total of plies	16
Total of ply drop-offs	2

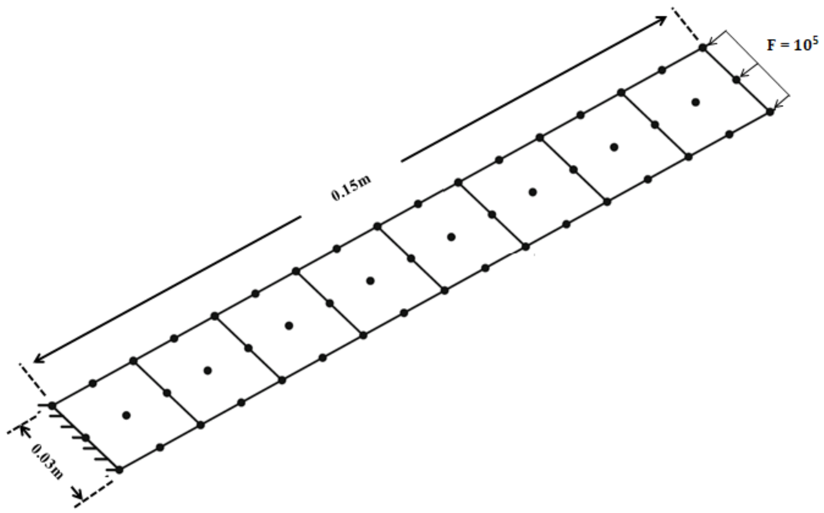

Figure 3.1 – Representation of dimensions and boundary conditions for the laminate beam with ply drop-offs (adapted from LUND, 2018).

The carbon composite material was selected for the analyses because of its high strength and low mass, and its properties were obtained through experimental tests and are depicted in Table 3.2. The carbon layer is a type of unidirectional prepreg with a thickness of 0.175 mm.

Table 3.2 – Properties of a carbon composite material considering the failure criterion (obtained from MARTINS, 2015).

Propriety	**Value**	**Unit**	**Propriety**	**Value**	**Unit**
E_1	101.86	GPa	E_2	3.41	GPa
G_{12}	7.56	GPa	υ_{12}	0.30	--
ρ	1550.00	kg/m³	σ_1^T	1363.49	MPa
σ_1^C	572.27	MPa	σ_2^T	5.86	MPa
σ_2^C	102.00	MPa	τ_{12}	200.61	MPa

In order to perform real numerical simulations, a shell type element with 8 nodes and 6 degrees of freedom per node was chosen. Then, the tapered laminate beam was discretized, with each line divided into 10 fragments, generating a total of 800 elements and 2,581 nodes in the entire structure.

According to An *et al.* (2019), there exists a feasible angle set based on industry experience, such as 0º, ±30°, ±45°, ±60°, and 90°, that should be taken into account when manufacturing structures with ply drop-offs. In this study, the stacking sequence proposed by Irisarri *et al.* (2014) of $[45º/90º/-45º/0º/-45º/0º/45º/90º]_s$ was considered.

3.1.2 Tubular structures with ply drop-offs

A typical hollow tubular laminate was modeled by stacking plies considering different orientations for the fiber angles, such as $[45º/90º/90º/-45º/0º]_s$ as indicated by Irisarri *et al.* (2014) that it satisfies the design rules. The tube with ply drop-offs was designed aiming prosthetic applications (NBR ISO 10328, 2016). The geometric parameters adopted in numerical modelling using an engineering computational program are presented in Table 3.3.

Table 3.3 – Geometric parameters for a hollow tubular laminate with ply drop-offs.

Geometric parameters	**Value**
Height [m]	0.30
Diameter [m]	0.03
Amount of panels	5
Total of plies	10
Total of ply drop-offs	4

A hybrid material (carbon/glass) was considered in addition to the conventional material (carbon). For the hybrid tube, in the outer plies, carbon fibers were used, and in the inner plies, glass fibers. In contrast, only carbon material was used for the non-hybrid tube. The carbon material properties are the same as those used for the cantilever beam structure, as can be consulted in Table 3.2, and the glass composite material properties can be seen in Table 3.4. The glass is a type of unidirectional prepreg with a thickness of 0.6 mm (KOLLAR and SPRINGER, 2003).

Table 3.4 – Properties of a glass composite material considering the failure criterion (taken from KOLLÁR and SPRINGER, 2003).

Propriety	**Value**	**Unit**	**Propriety**	**Value**	**Unit**
E_1	38.60	GPa	E_2	8.27	GPa
G_{12}	4.14	GPa	υ_{12}	0.26	--
P	1800.00	kg/m³	σ_1^T	1103.00	MPa
σ_1^C	621.00	MPa	σ_2^T	27.60	MPa
σ_2^C	138.00	MPa	τ_{12}	82.70	MPa

All the numerical models used in this study were created in an engineering computational program on a personal computer with an Intel® 5 processor, 5 GB of memory, and a 1 TB hard drive and were evaluated through FEM using a shell type element with 8 nodes and 6 degrees of freedom in each node. The time spent for each static analysis involving the Tsai-Wu failure criterion was on average 1 minute and 37 seconds, for modal analyses of 3 minutes and 12 seconds, linear buckling analyses of 3 minutes and 9 seconds, and nonlinear buckling was on average 11 minutes and 19 seconds. A mesh convergence study was done to evaluate the quality of the mesh, where the same simulations were carried out with a finer mesh and compare the results. The feasible optimal mesh was discretized each line in fragments considering 20 elements in each line of the structure, resulting in the total number of 8,002 elements and 24,162 nodes. Furthermore, rigid bodies were created at the ends for the application of the boundary conditions. While at one of the tube ends, a loading (compression or torsion) was applied, the other was clamped without any kind of translation and rotation movement, as shown in Figure 3.2. In order to obtain reliable results, the applied load in compression was 4,480N, the equivalent of 450kg, and the torsion moment was 7.1N.m, both considering failure mechanisms. The loads were established by NBR ISO 10328:2016, and this is the Standard responsible for structural tests in lower limb prosthesis.

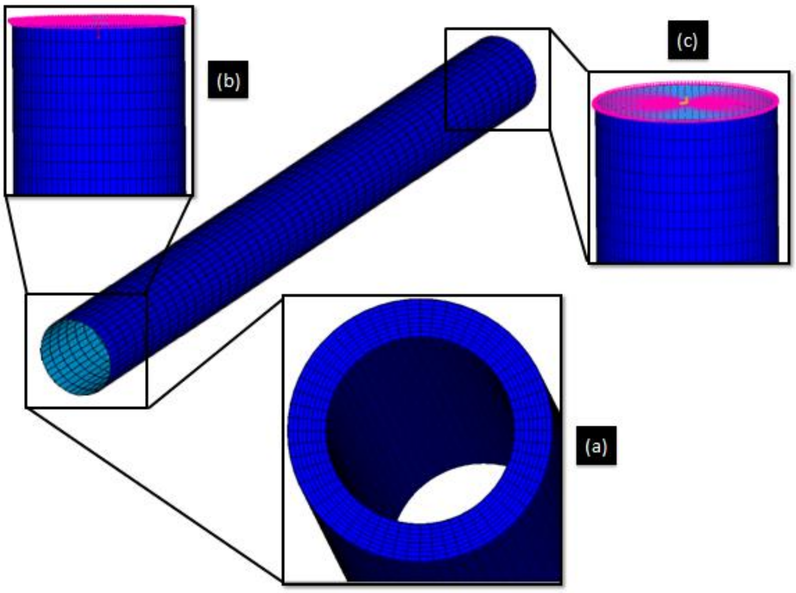

Figure 3.2 –Tubular geometry: (a) thickness of plies; (b) rigid body in the free end for applied loading and (c) rigid body in the clamped-end.

The numerical simulations using the FEM considered modal, eigen buckling, and static analyses. The first natural frequency and nonlinear buckling load were obtained by modal and eigen buckling analyses, respectively. At the same time, the FI was obtained by static tests, considering compression and torsion conditions. In the static analysis, a comparative study between the mass of non-hybrid and hybrid structures with ply drop-offs and those without ply drop-offs was performed.

3.2 Material Properties Used in the Laminate and Sandwich Structures

In this study, three different types of two-dimensional fabrics were used in the manufacture of the tubular and sandwich structures. In addition to these fabrics, for the manufacture of the sandwich structures, a two-dimensional hybrid fabric composed of glass/aramid fibers was considered. The fibers on the each fabric ply are oriented at 0º/90º. The carbon, glass, and carbon/aramid hybrid fabrics are types of plain weave, while the glass/aramid fabric is twill weave. The hybrid fabrics present the same number of fibers on their composition: 50% of carbon or glass fibers and 50% of aramid fibers in each ply. The resin system used in the experiments was Ampreg 31 epoxy resin, supplied by Gurit, and it offers higher performance and low viscosity of 300cP at 25ºC considering manual lamination, vacuum lamination, and infusion, according to the supplier. The weight ratio of resin and hardener recommended by the supplier is 100:26 in a fast curing system. Aiming for better mechanical properties, a cure time of 5 hours at 80ºC is suggested. The technique information about the fabrics and resin system is depicted in Table 3.5.

(Intentionally left blank)

Table 3.5 – Technique information and material cost of the fabric and epoxy resin system.

Material	Property	Value	Cost
Carbon fabric	Thickness [mm]	0.33	R$344.50/m²
	Nominal weight [g/m²]	200.00	
Carbon/aramid hybrid fabric	Thickness [mm]	0.28	R$260.00/m²
	Nominal weight [g/m²]	165.00	
Glass fabric	Thickness [mm]	0.21	R$20.80/m²
	Nominal weight [g/m²]	200.00	
Glass/aramid hybrid fabric	Thickness [mm]	1.73	R$318.50/m²
	Nominal weight [g/m²]	893.00	
Ampreg 31 epoxy resin	Component density [g/cm³]	1.00	R$200.97/kg
	Mixture density [g/cm³]	1.08	
	Density [g/cm³] – curing system	1.16	
	Tensile strength [MPa] – curing system	73.00	
	Elasticity modulus [GPa] – curing system	3.45	
	Strain [%] - curing system	3.58	

Sandwich structures consisted of two face sheets with two layers of fabric in each, while the core was manufactured using two type of honeycomb, such as aramid paper and polypropylene (PP).

The aramid and PP honeycomb core node lengths were 4 mm and 10 mm, respectively. The cell shape was a regular hexagonal structure for both cores, with cell sizes of 3 mm for the aramid honeycomb and 8 mm for the PP honeycomb, as shown in Figure 3.3.

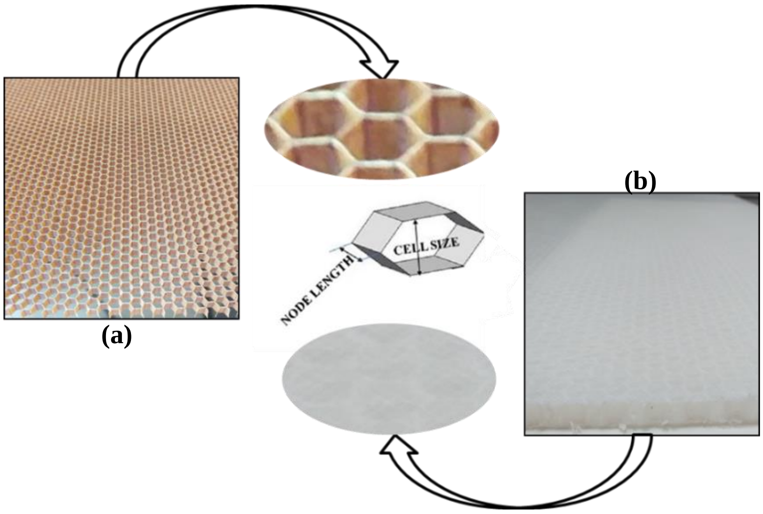

Figure 3.3 – Geometric parameters of honeycomb cells manufactured with: a) aramid material and (b) polypropylene material (adapted from THOMAS and TIWARI, 2019).

The PP honeycomb core was made of a fully recyclable material. The mechanical properties of aramid and PP honeycomb cores are listed in Table 3.6 and Table 3.7, respectively.

Table 3.6 - Mechanical properties and material cost of aramid honeycomb core.

Density [kg/m³]	**Size cell [mm]**	**Compressive strength [MPa]**	**Shear strength in L direction [MPa]**	**Shear modulus in L direction [MPa]**	**Shear strength in W direction [MPa]**	**Shear modulus in W direction [MPa]**	**Cost [unity with 80x60cm]**
48.00	3.00	1.93	1.34	44.00	0.66	23.00	R$221.00

Table 3.7 - Mechanical properties and material cost of polypropylene honeycomb core.

Density [kg/m³]	**Size cell [mm]**	**Tensile strength [MPa]**	**Compressive strength [MPa]**	**Compressive modulus [MPa]**	**Shear strength [MPa]**	**Shear modulus [MPa]**	**Cost [unity with 80x60cm]**
80.00	8.00	0.89	1.89	79.20	0.58	15.20	R$66.30

The information about the material costs was listed at the beginning of 2021. Currently, these values may have incurred financial adjustments.

In order to provide an upstanding finish and to easily remove samples, a peel ply layer was used in conjunction with a releasing wax for the manufacture of the sandwich specimens. Due to the fact that the tubular geometry is complex, the peel ply fabric did not provided an easy way to remove samples, so an Armalon ply was employed in the manufacture of the tapered tubes. The main materials used in the experiments are depicted in Figure 3.4.

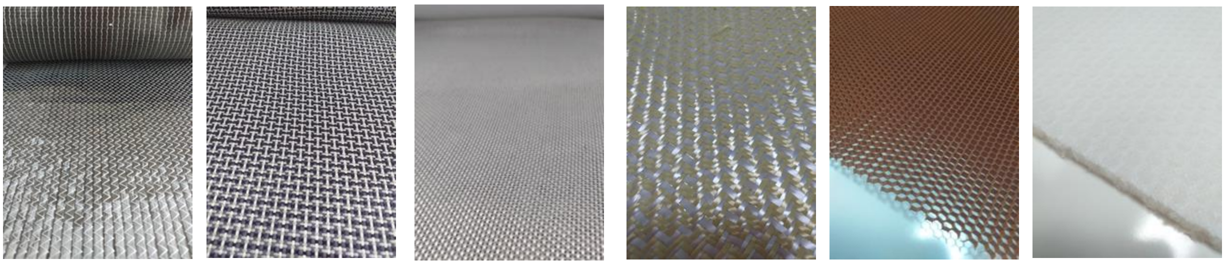

a) Carbon fabric. b) Carbon/aramid hybrid fabric. c) Glass fabric. d) Glass/aramid hybrid fabric. e) Aramid honeycomb core. f) PP honeycomb core.

Figure 3.4 - Materials used in the manufacture of the tubular laminate and sandwich structures.

3.3 The Manufacture of the Structures Used in the Experimental Tests

3.3.1 Sandwich structures with honeycomb core

First, the cores and fabrics were cut to 125 mm lengths and 46 mm widths for the modal and bending tests (HAN *et al.* 2020). Then, a hand layup process was performed to manufacture the laminates. First release wax was applied to the metal mold. After drying, a peel ply layer was placed. Then, the fabric layers were stacked on the honeycomb core, as shown in Figure 3.5a. Then two more fabric layers covered the honeycomb core, generating a sandwich structure. Subsequently, the other peel ply layer was used to cover the entire setup and a vacuum bag was sealed, as shown in Figure 3.5b. The vacuum system was applied to avoid air pockets and remove excess resin. Afterward, the laminates were placed in the oven for curing at 80ºC for 5 hours. Then, the composite laminates were removed from the metal mold, and the specimens were cut using a bench saw for the modal and bending tests, as shown in Figure 3.5c to 3.5f. The thickness of each specimen varied according to the type of fabric and core. In Table 3.8, it is possible to see the thickness and mass of the specimens manufactured for the experimental.

Table 3.8 – Average thickness and mass of the honeycomb sandwich specimens.

Type of fabric	**Type of core**	**Average thickness [mm]**	**Average mass [g] for modal and bending tests**	**Average mass [g] for bucking test**
Carbon	Aramid	5.23	14.12	5.75
Carbon	PP	11.34	18.70	15.62
Carbon/aramid	Aramid	4.89	8.95	3.70
Carbon/aramid	PP	10.94	15.20	12.29
Glass	Aramid	4.82	9.19	4.27
Glass	PP	10.83	15.47	12.64
Glass/aramid	Aramid	7.29	36.02	14.57
Glass/aramid	PP	14.47	45.48	39.26

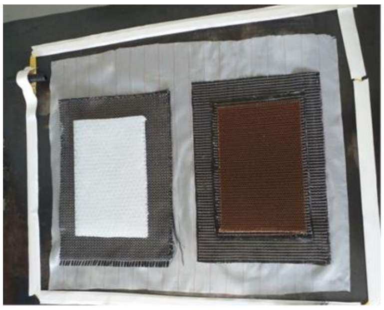

a) Preparation of the materials to vacuum bag.

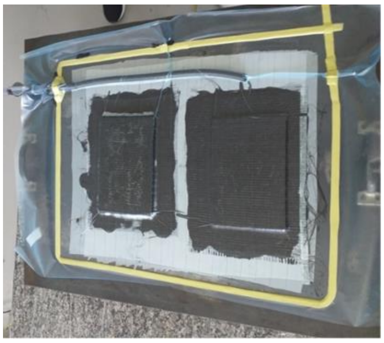

b) Vacuum bag moulding technique.

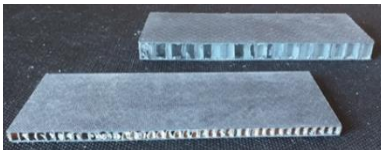

c) Carbon specimens with PP and aramid core.

d) Carbon/aramid hybrid specimens with PP and aramid core.

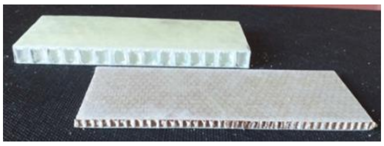

e) Glass specimens with PP and aramid core.

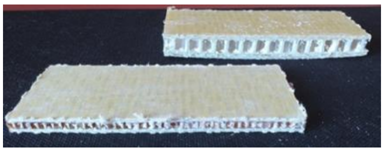

f) Glass/aramid hybrid specimens with PP and aramid core.

Figure 3.5 – Experimental procedure for the manufacture of the honeycomb sandwich structures.

For the buckling test, the specimen dimensions were established according to the ASTM C364/C364M-16 standard that considers honeycomb length, as depicted in Figure 3.6:

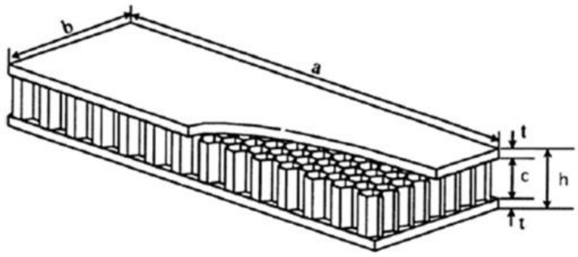

Figure 3.6 - Standard criterion used to manufacture of honeycomb sandwich structure for the buckling test (adapted from CRUPI *et al.* 2012).

where *a*, *b*, and *h* represent the length, width, and height of the specimen, respectively, and c is node length. According to ASTM C364/C364M-16, the standard manufacturing process for sandwich structures is a ≤ 8xh and b ≥ 2xh or 50 ≤ b ≤ a.

To comply with the ASTM standard that establishes the specimen geometry according to cell height, the length and width of the specimens with the PP core were 100 mm and 46 mm, respectively, while the dimensions of the specimens with the aramid core were 60 mm in length and 40 mm in width. Despite the different dimensions, all specimens were manufactured under the same conditions given their suitable shape designs after the removal process.

3.3.2 Tubular structures with ply drop-offs

The tubular specimens were manufactured by a hand layup process using eight plies of fabric, where four of these plies were dropped, generating four ply drop-offs along the tube length. All plies have their fibers oriented at 0º/90º. For the experimental tests, five different tubes were considered. Three were manufactured only with one type of fabric: carbon (C), glass (G) or carbon/aramid (CA). While the other two tubes had a hybrid structure manufactured with carbon/glass (HCG) or carbon/aramid/glass (HCAG). The hybrid tubes had their outer plies composed of carbon or carbon/aramid fibers, while their inner plies were filled with glass fiber.

In order to obtain the proper geometry for the tube, a PVC tube mold with an inner diameter of 0.25 m was used. First of all, the plies were cut considering a symmetric laminate with four ply drop-offs, and then the release was applied to the tube mold, and after drying, an armalon ply was placed, as showed in Figure 3.7a. Laterally, the fabric plies were rolled round in the tubular mold, a brush was used to spread the epoxy resin, and then another armalon ply was used to involve the tube, and, finally, the entire setup was covered by a plastic film ply, as can be seen in Figure 3.7b. Subsequently, the laminate tube was placed in the oven for the cure process at 80ºC to 5 hours. After this time, the tube was removed from the PVC tube mold and it was cut to the correct dimensions, as shown in Figure 3.7c.

(a) A tubular mold rolled with armalon and an armalon ply can be used to involve the fabric plies.

(b) The entire setup is covered by plastic film in the oven.

(c) Tapered tube specimens manufactured with carbon fabric, carbon/aramid hybrid fabric, carbon/glass fabrics, carbon/aramid/glass fabrics, and glass fabric, respectively.

Figure 3.7 – Experimental procedure for the manufacture of the tapered tube specimens.

The manufacturing process adopted for the non-tapered tubular structures was the same as that applied to the tapered structures. However, no plies were dropped. Table 3.9 presents the structural mass for the tapered and non-tapered tubes.

Table 3.9 – Structural mass considering tapered and non-tapered tubular specimens.

Type of fabric	**Tube nomenclature**	**Mass of non-tapered tubes [g]**	**Mass of tapered tubes [g]**
Carbon	C	101.23	88.14
Carbon/aramid hybrid	CA	72.42	54.99
Glass	G	72.68	55.26
Carbon/glass	HCG	87.16	72.12
Carbon/aramid/glass	HCAG	77.03	53.64

As shown in Figure 3.8, the outer diameters of each tapered tube end varied due to the different thickness of each fabric and the dropping of four plies. The outer diameters of each tapered tube can be consulted in Table 3.10.

C CA G HCG HCAG

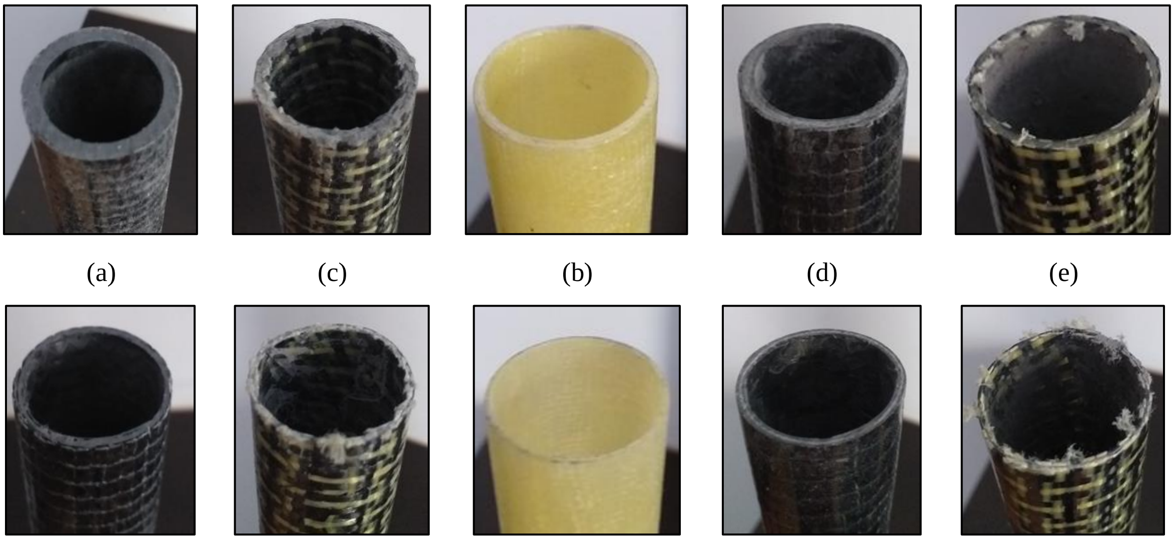

(a) (c) (b) (d) (e)

(f) (h) (g) (i) (j)

Figure 3.8 – Tubes with ply drop-offs considering (a)-(e) end thickness with all plies and (f)-(j) end thickness after that four plies are dropped.

Table 3.10 – The outer diameters of the tapered tubular specimens.

Type of fabric	**Tube nomenclature**	**The end's outer diameter with all plies [mm]**	**The end's outer diameter with plies dropped [mm]**
Carbon	C	32.46	30.03
Carbon/aramid hybrid	CA	30.22	28.13
Glass	G	28.85	27.04
Carbon/glass	HCG	30.00	28.49
Carbon/aramid/glass	HCAG	28.92	27.66

3.4 Metamodelling Using Design of Experiments

3.4.1 For a cantilever beam with ply drop-offs

The full factorial design was created with two design factors in mind considering the ply drop-off location. Based on preliminary tests, it was possible to define the experimental boundaries of the present study by considering factorial points (-1 and +1), axial points (-α and +α), and central points, as depicted in Table 3.11.

Table 3.11 – Design factors and their levels for ply drop-off location in a cantilever beam ($\alpha = 2^{k/4}$).

Design factors	***Symbol***	***Levels***				
		-α	**-1**	**0**	**+1**	**+α**
Ply position (-)	P_p	2	3	5	7	8
Longitudinal position (m)	L_p	2	2.73	4.5	6.27	7

The response variables were Tsai-Wu FI, strain suffered by the beam with the application of the compression load, and first natural frequency, both obtained in the numerical simulation using the FEM.

The factorial design generated a total of 42 runs between design and response variables, as can be verified in Appendix A. The results obtained with factorial design allowed a reduction in the number of experiments for future statistical analyses. The metamodelling based on optimization strategy was performed using the RSM with a desirability function, seeking to achieve the optimal combination for the ply drop-off location that provides excellent structural performance.

3.4.2 For tubular structures with ply drop-offs

The first step of the statistical approach involving the tubular structure is based on factorial design with four design factors related to ply drop-off location, both with two levels and five response variables: Tsai-Wu failure criterion in relation to torsion and compression, 1^{st} natural frequency, mass, and buckling load, as depicted in Table 3.12.

Table 3.12 – Design factors for ply drop-off location considering their respective levels in a tubular structure.

Design factors	***Symbol***	***Levels***		
		Low (-1)	***Middle (0)***	***High (+1)***
First panel (longitudinal position)	X_1	0.06	0.09	0.12
First ply (transversal position)	Y_1	2	3	4
Second panel (longitudinal position)	X_2	0.18	0.21	0.24
Second ply (transversal position)	Y_2	3	4	5

In the factorial design, only the hybrid tubes were considered due to their unusual structure. Posteriorly, in the RSM, the non-hybrid tube will be analyzed together with the hybrid tube.

The factorial design enables us to investigate which design factors related to ply drop-off location are relevant in the tube behavior, besides identifying the curvature for the development of the RSM that will be applied in the optimization strategy using SFO.

3.4.3 For sandwich structures with honeycomb core

To obtain all combinations between face sheets and honeycomb cores, general full factorial designs were proposed to analyze the results from the experimental tests. In this study, it was necessary to create two factorial designs. The first design investigated the results from the modal and bending tests considering ten response variables, while the second design investigated the results obtained from the buckling test considering four different response variables. It is important to highlight that the design factors are the same for the two arrangements, i.e., the type of layer used on the face sheet and the type of honeycomb used in the core. The factorial designs generated a total of 16 runs between these two design variables, as shown in Table 3.13.

Table 3.13 – Factorial arrangement with two design variables related to type of face sheet and core for sandwich structures.

	Design variables	
Exp.	***Type of face sheet***	***Type of core***
1	Carbon	Aramid
2	Carbon	PP
3	Glass	Aramid
4	Glass	PP
5	Carbon/aramid	Aramid
6	Carbon/aramid	PP
7	Glass/aramid	Aramid
8	Glass/aramid	PP
9	Carbon	Aramid
10	Carbon	PP
11	Glass	Aramid
12	Glass	PP
13	Carbon/aramid	Aramid
14	Carbon/aramid	PP
15	Glass/aramid	Aramid
16	Glass/aramid	PP

The full factorial designs will be seen in Chapter 4 in the section 4.3 entitled “On the influence of manufacturing parameters on buckling and modal properties of sandwich composite structures”.

3.5 Three-Point Bending Experimental Testing Setup

To investigate the flexural properties, sandwich structures were tested for all combinations using a static three-point bending test according to ASTM C393/C393M-20 using a universal testing machine (Instron/EMIC DL-3000), as shown in Figure 3.8a. The crosshead displacement rate was set to 6 mm/min. As shown in Figure 3.9b, the two supporting pins and the loading pin diameters were all 16 mm, and the loading span between the supports was 70 mm. The geometric parameters for the honeycomb sandwich structures were width in the W-direction at 46 mm and length in the L-direction at 125 mm. The specimen thicknesses vary from 4.80 mm to 14.76 mm accordingly to the core type and face sheet.

(a)

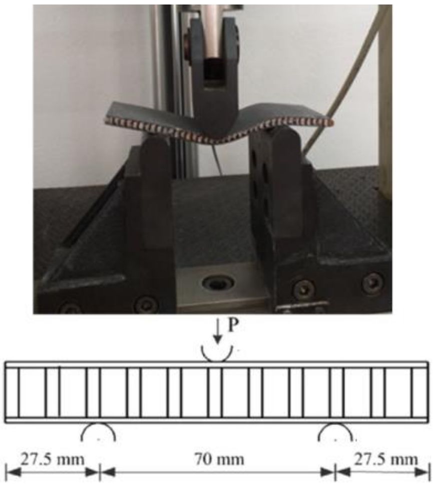

(b)

Figure 3.9 – Experimental setup for the three-point bending test: (a) Universal testing machine Instron/EMIC DL-3000 and (b) schematic of a honeycomb sandwich specimen (adapted from HAN *et al.* 2020).

The core final shear stress was determined using Equation 3.1 (ASTM C393/C393M-20). While the face sheet bending stress was calculated using Equation 3.2 (ASTM C393/C393M-20).

$$F_s^{ult} = \frac{P_{max}}{(h+c)b} \tag{3.1}$$

$$\sigma = \frac{P_{max} S}{2t(h+c)b} \tag{3.2}$$

where F_s^{ult} represents the final core shear strength, P_{max} is the maximum load prior to the first failure, h is the sandwich structure height, c is the node thickness, and b is the sandwich structure width, σ is the facing stress, S is the span length, and t is the face thickness. The face sheet bending stress was calculated using Equation 3.2 (ASTM C393/C393M-20).

3.6 Buckling Testing Experimental Setup

The buckling test for the honeycomb sandwich specimens was performed according to the ASTM C364-16 standard, using a universal test machine, model 8801 from Instron, equipped with a 100 kN load cell and controlled by the Bluehill 3 software program. The speed of the crosshead was set constant at 0.50 mm/min. The specimen sizes used in this test were 40 mm in width and 60 mm in length for the aramid honeycomb core, and 46 mm in width and 100 mm in length for the PP honeycomb core. Specimens had 10 mm of their upper and lower extremities fixed by support clamps, and then compression loads were applied to the upper extremities until failures were visually observed on the specimen's surface. The setup for the buckling test is shown in Figure 3.10.

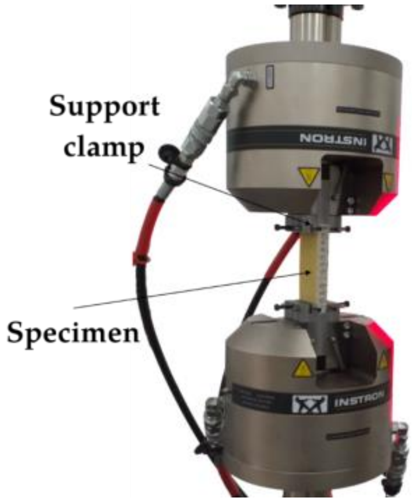

Figure 3.10 – Experimental setup for buckling test of sandwich specimens using a universal test machine from Instron.

3.7 Modal Testing Experimental Setup

In order to obtain the dynamic parameters for sandwich structures and laminate tubes, modal experimental tests were performed to identify the first natural frequencies and the damping loss factors. For the tubular structures, only the first natural frequency was considered, while for the sandwich structures, the first three natural frequencies were verified. For the experimental setup, the extremity of the sandwich specimens had 10 mm lengths fixed, while the tubes had 26 mm of length fixed, both using distinct clamping systems under clamped-free boundary conditions, as depicted in Figure 3.11. The other extremity of both structures was highlighted with a white square sticker.

The modal behavior of these structures is characterized by an analysis of free-vibration without the presence of external forced vibration. The instruments used for this test were a laser sensor, an impact hammer, a data acquisition board (DAQ), and Photon+ acquisition software, as shown in Figure 3.11.

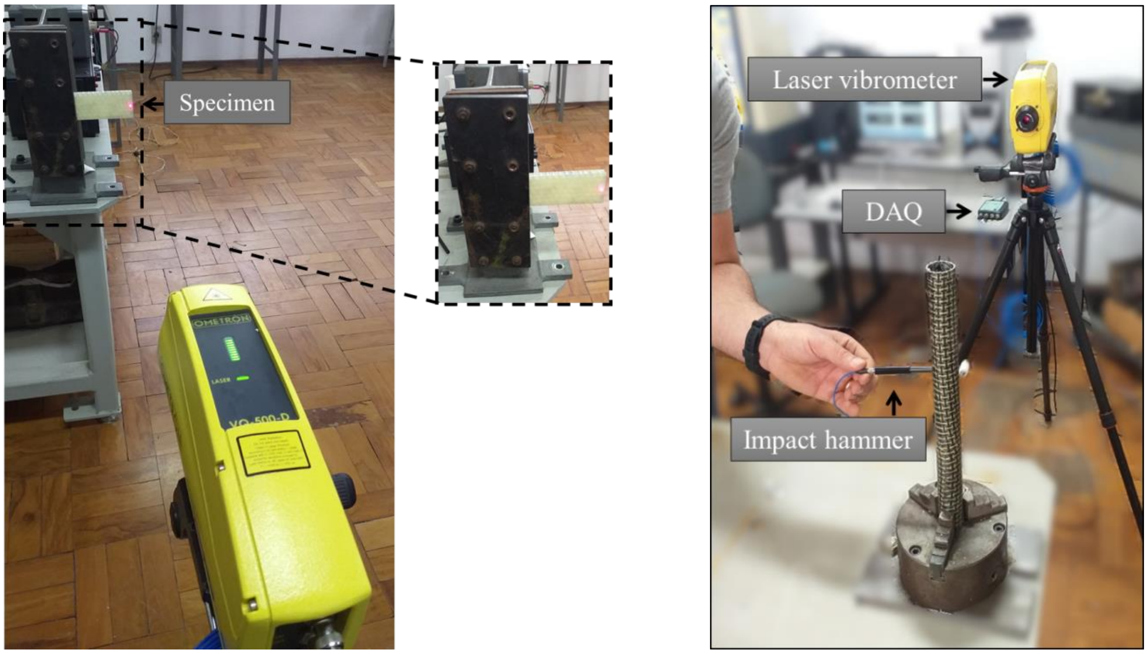

(a) (b)

Figure 3.11 - The experimental setup takes into account free vibration analyses: (a) in sandwich specimen and (b) in tubular specimen.

The impact hammer model used in this test was a Brüel & Kjaer. The laser sensor applied to measure the vibration displacement at a specific point was model VQ-500-D made by Ometron. The DAQ board was a model Photon Plus, produced by Brüel & Kjaer. All the signals created by the machine were analyzed by the LabVIEW program.

The experimental test started with a specimen disturbance using the impact hammer, where the impact force-time history provided by the hammer was recorded in the DAQ that was connected with the hammer. At the same time, the vibration responses were detected and then the signals were processed using LabVIEW programming.

3.8 Compression Testing Experimental Setup

The quasi-static compression test in laminate tubes was performed according to the ASTM E2954-15 standard test method using a universal test machine model 8801 from Instron, equipped with a 100 kN load cell and controlled by the Instron software. The speed of the crosshead adopted was a constant of 2 mm/min. The boundary conditions adopted for the tubular specimens were that their ends were supported on the upper and bottom machine plates, as can be seen in Figure 3.12. The loading was applied by the upper load plate in a direction parallel to the longitudinal axis until the specimens failed. The compression test has the intention of determining the maximum axial compressive strength obtained by specimens before it presents failure. The full setup for the compression test is depicted in Figure 3.12.

Figure 3.12 – Experimental setup for compression test of tubular structures using a universal test machine from Instron®.

A brief summary about methodology developed in this study is presented in the flowchart in Figure 3.13.

(Intentionally left blank)

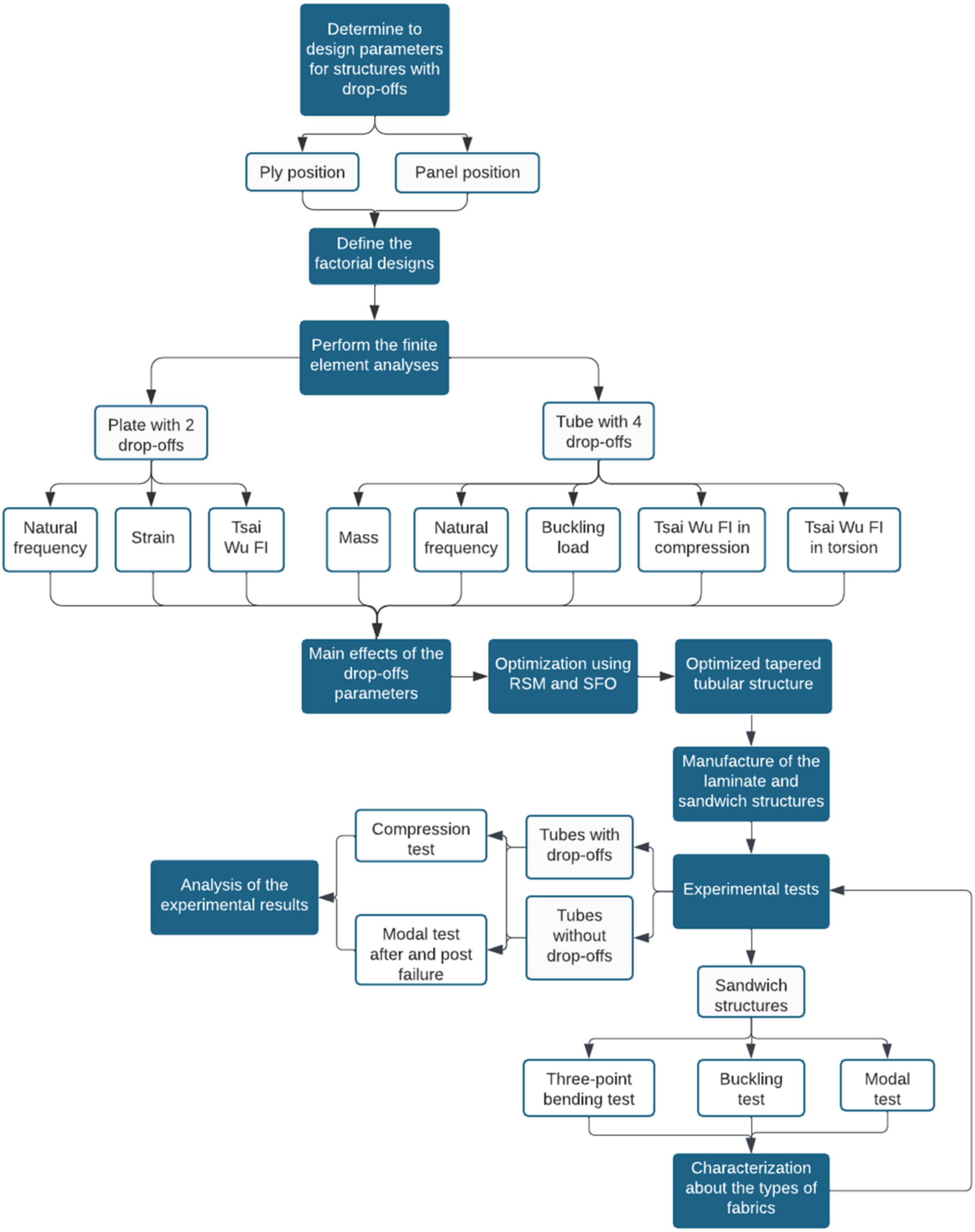

Figure 3.13 – Flowchart of the optimization and experimental strategy developed in this study.

CHAPTER 4: NUMERICAL-EXPERIMENTAL RESULTS AND DISCUSSION

4.1 Optimum Design of Composite Structures with Ply Drop-offs Using Response Surface Methodology

4.1.1 Numerical modelling of composite structures with ply drop-offs

The design factor runs were inputted into the finite element analysis algorithm so the obtained results could be employed in a full factorial design as response variables. The Tsai-Wu failure criterion response variable showed reliable results in analyses using the FEM, with the value being over one ($TW \geq 1$) in all analyses. As one may observe in Table A1 (Appendix A), many failure criterion values demonstrated similarity because only two plies were dropped, so there was no considerable change to the failure mechanisms. The model adopted did not take into account the resin pockets that can be created in the manufacturing process.

Regarding the strain and natural frequency response variables, all results were feasible. Figure 4.1 illustrates the results for each response variables considering the tenth run generated in the full factorial design (Table A1 in Appendix A), where the third ply was dropped on the fifth panel.

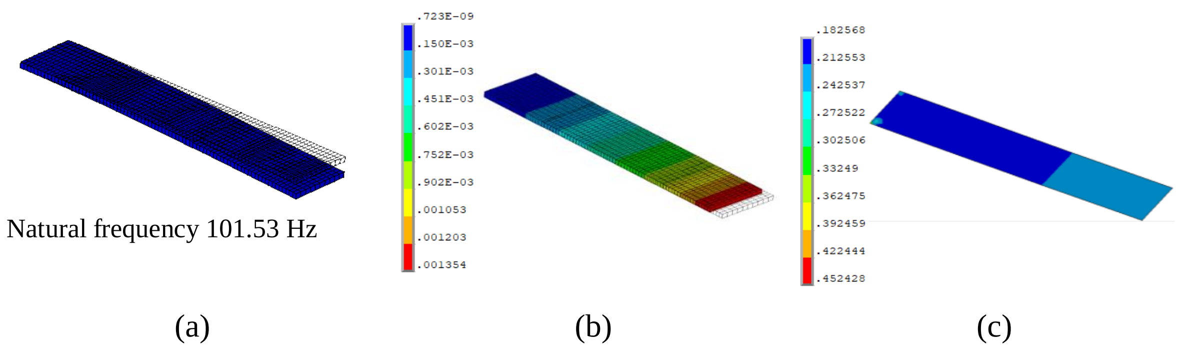

Figure 4.1 – CFRP beam with ply drop-off responses: (a) mode shape at the natural frequency, (b) strain in compression, and (c) global Tsai-Wu failure criterion.

4.1.2 Full factorial design analyzed by Analysis of variance

In this study, the primary interest in using the full factorial design was to create variations in the factor levels and verify which factors influence the response variables the most. The results generated by the full factorial design were examined using the ANOVA, where the results relative to the strain, Tsai-Wu failure criterion, and natural frequency response variables are depicted in Table 4.1, while the Table 4.2 presents the ANOVA results considering the *p-value* for design factors.

Table 4.1 – Adjusted coefficient of determination R^2_{adj} in the ANOVA model for a cantilever beam considering the response variables.

Response variables	R^2_{adj}
Strain	84.35%
Tsai-Wu failure criterion	25.41%
Natural frequency	82.10%

Table 4.2 – Model summary of the ANOVA for a cantilever beam considering the influence of the design variables in each response variables.

Strain		Tsai-Wu		Frequency	
Source	**P-Value**	**Source**	**P-Value**	**Source**	**P-Value**
Plies	0.049	Plies	0.462	Plies	0.113
Panels	0.084	Panels	0.159	Panels	0.064
Error	0.000	Error	0.000	Error	0.000

In this case, the ANOVA revealed that the model using two design factors is only appropriate for the strain and natural frequency response variables due to R^2_{adj} of over 80%. In contrast, the failure criterion response value showed a poor fit with *p-value* of 0.462 for the ply design factor and 0.159 for the panel design factor, presenting a low adjusted coefficient of determination, as shown in Table 4.2. Furthermore, considering the analyses using the ANOVA *p-value*, it is possible to establish that only the ply position has a significant influence on the strain response variable due to a *p-value* less than 0.05, as confirmed by Table 4.2.

4.1.3 Optimization using the metamodel-based Response surface methodology

Considering the more expressive parameters obtained using the full factorial design, the RSM was applied with the intention of verifying the effect of interactions and determining the optimal parameters for the ply drop-off location. In order to satisfy the requirements of the RSM, the panel position was changed to the longitudinal position in meters. The experimental matrix established by the RSM considered axial points and generated a total of 14 runs, as shown in Table 4.3, where *TW*, L_p and P_p represent, respectively, the Tsai-Wu failure criterion, the longitudinal position in meters, and the ply position. As the ply position is a discrete variable, the values from 1 to 4 in Table 4.3 were rounded to 3 to 7, respectively.

Table 4.3 –Experimental matrix for the RSM analysis considering the design and responses variables for a cantilever beam.

	Design factors		Response variables		
Exp.	L_p	P_p	**TW**	**Strain (m/m)**	**Frequency (Hz)**
1	0.05119	2.87867	0.45243	0.00140	100.27000
2	0.11730	2.87867	0.45243	0.00133	100.57000
3	0.05119	7.12132	0.45243	0.00140	98.48200
4	0.11730	7.12132	0.45243	0.00133	100.54000
5	0.08425	5.00000	0.45243	0.00137	101.06000
6	0.08425	5.00000	0.45243	0.00137	101.06000
7	0.08425	5.00000	0.45243	0.00137	101.06000
8	0.03750	5.00000	0.45252	0.00142	95.39500
9	0.13100	5.00000	0.45243	0.00132	98.73700
10	0.08425	2.00000	0.45243	0.00132	101.88000
11	0.08425	8.00000	0.45243	0.00132	100.83000
12	0.08425	5.00000	0.45243	0.00137	101.06000
13	0.08425	5.00000	0.45243	0.00137	101.06000
14	0.08425	5.00000	0.45243	0.00137	101.06000

The analyses obtained by RSM using ANOVA confirmed that the strain and natural frequency response variables provide a good interpretation of the problem, with values of R^2_{adj} higher than 90%, as shown in Table 4.4. In contrast, the failure criterion response variable continued demonstrating a low fit quality, with an $R^2 adj$ of less than 60%.

Table 4.4 –Model summary of the RSM for a cantilever beam considering the fit quality of the response.

Response	**S**	$\mathbf{R^2}$	$\mathbf{R^2_{adj}}$	$\mathbf{R^2_{(pred)}}$
Strain	0.0000075	96.31%	94.67%	88.96%
Tsai-Wu	0.0000172	56.51%	48.60%	0.00%
Natural frequency	0.414654	96.67%	93.81%	70.87%

An $R^2_{(pred)}$ value of 0% demonstrates overfitting, and a possible interpretation for this is the approximation of the decimal places of the failure criterion values. The quadratic model using RSM highlights similar conclusions to the factorial design in relation to the predictive capability of the model using two design factors and three response variables.

In order to predict the effect of interactions among the design factors and the contribution of each one to the response variability, Pareto charts were generated, as shown in Figure 4.2.

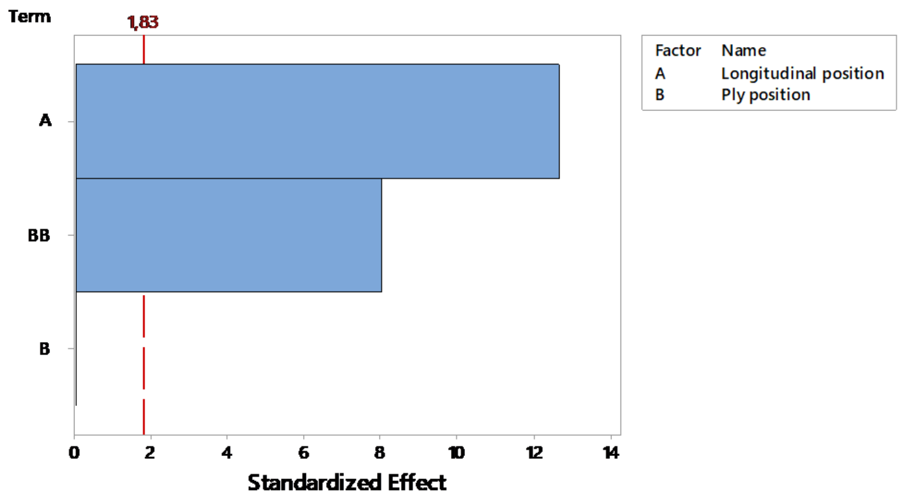

(a)

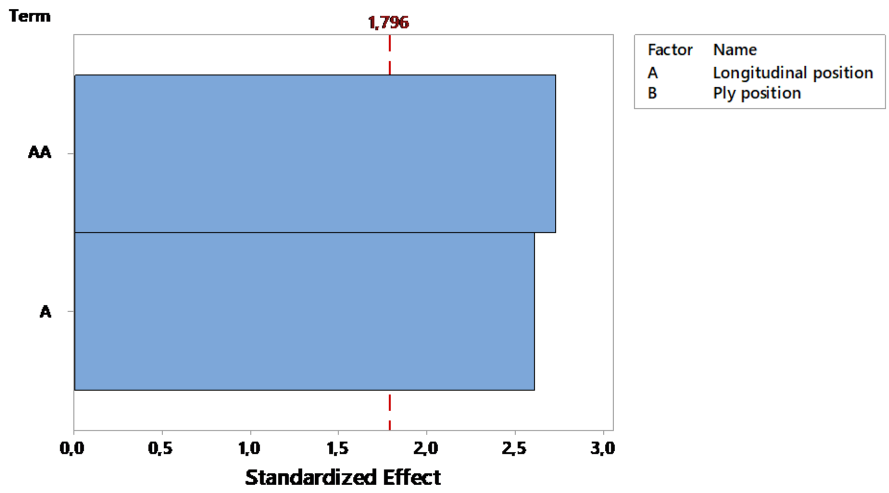

(b)

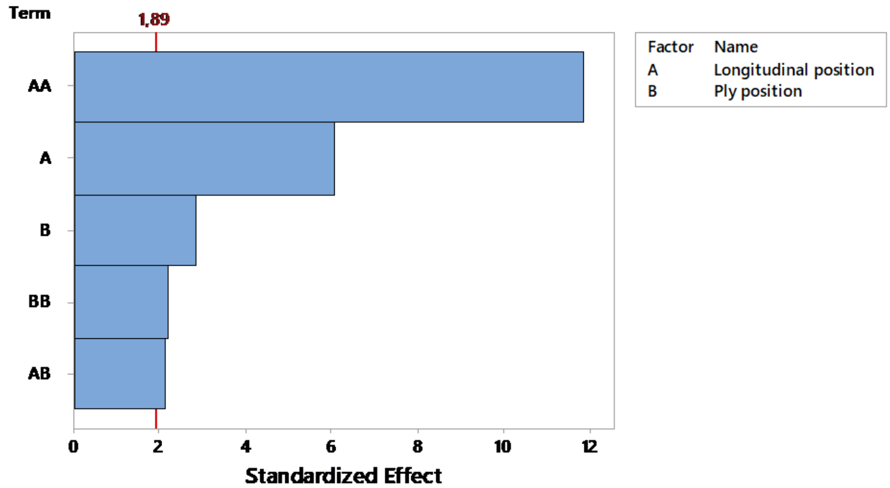

(c)

Figure 4.2 – Pareto chart for the effects between the design and response variables: (a) strain, (b) Tsai-Wu failure criterion, and (c) natural frequency.

Pareto charts allow clear interpretations of the effects of the factors and their interactions, with the effects located above the dashed red line being the most significant. One may observe that the effects of the longitudinal position (or panel position) and ply position are significant for the strain response variable. For the failure criterion response variable, only the longitudinal position has a significant effect, and, finally, for the natural frequency, all effects are significant. With knowledge of these results, it is possible to state that the longitudinal position has a considerable influence on the ply drop-off location on the laminate cantilever beam.

Considering the effects of the factors and their interactions on each response variable, main effect charts were elaborated, aiming to provide the difference between the levels of the design factors relative to the response variables, as depicted in Figure 4.3.

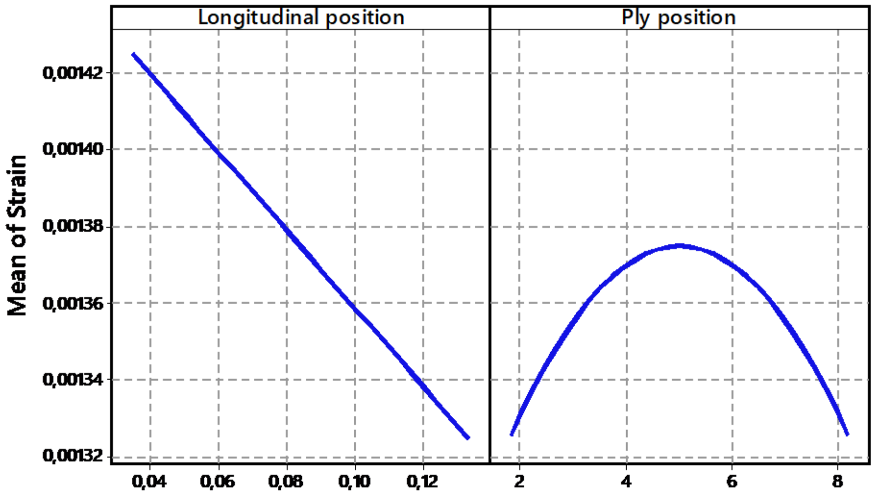

(a)

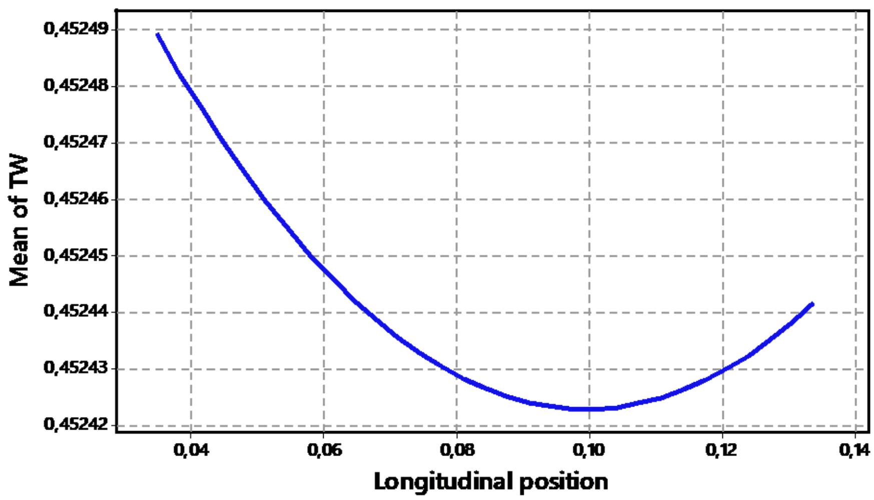

(b)

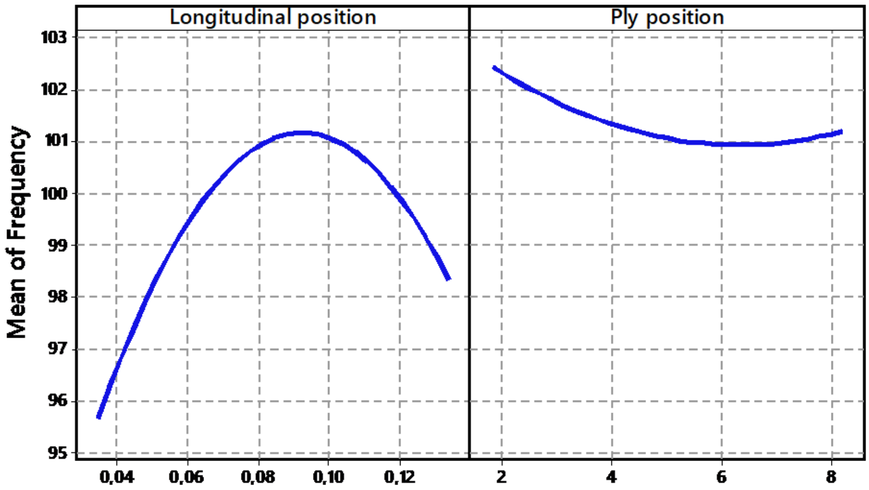

(c)

Figure 4.3 – Main effects plot for the response variables: (a) strain, (b) failure criterion, and (c) natural frequency.

The main effect charts enhance different positions for ply drop-offs with the purpose of meeting the objectives of each response variable. The optimal ply drop-off location considering the strain response variable is after 0.12 meters in the longitudinal position, dropping-off at ply position 2 or 8. Regarding the natural frequency response variable, the optimum is 0.09 meters in the longitudinal position, dropping-off at ply position 2, as shown in Figure 4.3. Due to the low level of significance for the ply position factor considering the Tsai-Wu failure criterion, only the longitudinal position was considered in the main effect plots, as can be confirmed by Figure 4.3.

To evaluate the numerical relationship between the design factors and response variables, regression Equations were generated considering each response variable, shown in Equations 4.1 - 4.3.

Strain
$$\varepsilon=0.001338-0.001014L_p+0.000049P_p-0.000005P_p^2 \tag{4.1}$$

Tsai-Wu
$$TW=0.452580-0.003150L_p+0.01584P_p^2 \tag{4.2}$$

Natural frequency
$$\omega=92.54+274.3L_p-1.470P_p-1655L_p^2+0.0747P_p^2+6.27L_pP_p \tag{4.3}$$

It is worth highlighting that regression Equations demonstrate the combination of levels for each factor and are often used as prediction models to optimize design factors. In order to check how the fitted model relates to the design factors, surface plots were generated together with contour plots, as shown in Figure 4.4 and Figure 4.5. Due to the low level of significance, the failure criterion was not plotted.

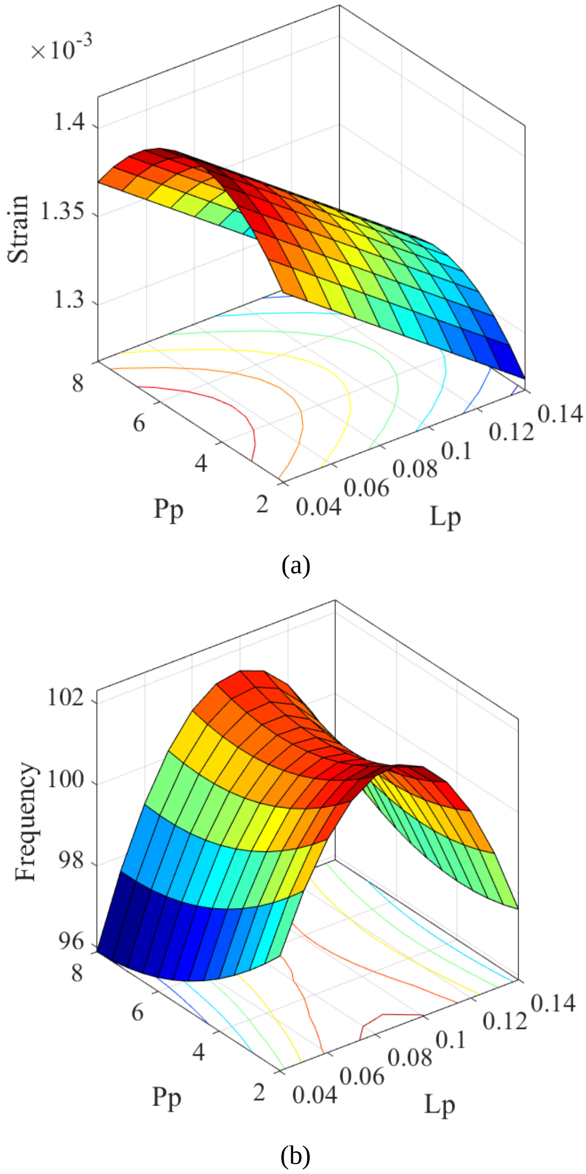

Figure 4.4 – Surface plot for the response variables: (a) strain and (b) natural frequency considering the fitted response.

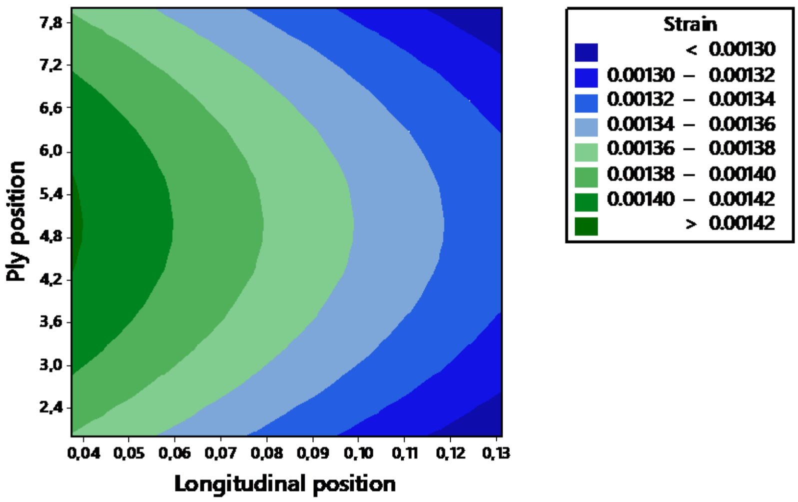

(a)

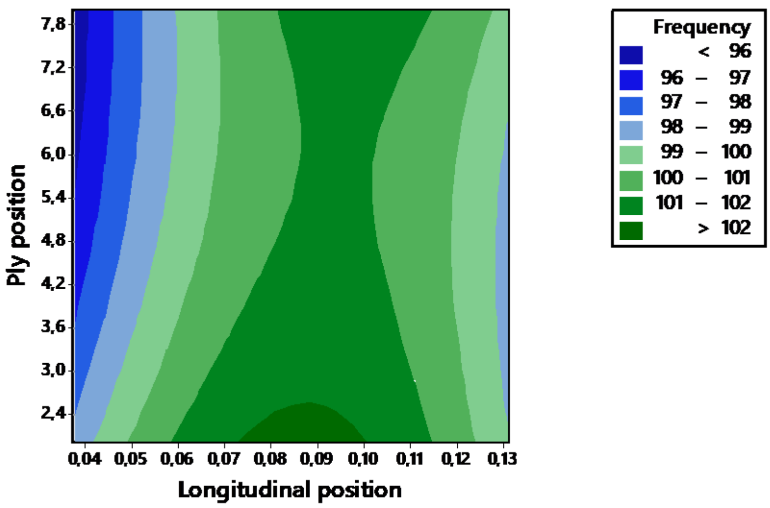

(b)

Figure 4.5 – Contour plot for the response variables: (a) strain and (b) natural frequency considering the fitted response.

The surface plots shown in Figure 4.4 reveal a quadratic response surface in which the maximum points for natural frequency and the minimum point for strain are located in the optimal region. While the contour plots exposed in Figure 4.5 reveal the optimal region in a two-dimensional view.

The optimal region that minimizes the strain and maximizes the natural frequency is known. However, it is essential to find the optimal conditions for the ply drop-off location by considering specific values for each design factor. Hence, in this study, an optimization strategy was developed using the desirability function in both mono-objective and multiobjective approaches. The mono-objective optimization is presented in Table 4.5 with the individually optimized responses, while Table 4.6 shows a multiobjective optimization considering the responses optimized simultaneously. The graphical results are presented posteriorly through a Pareto front using the SFO algorithm with 100 iterations and a population of 40 sunflowers and 3 suns.

Table 4.5 – Mono-objective optimization of the ply drop-off location considering the strain minimization and natural frequency maximization separately.

	Objective	**Response**	$\mathbf{L_p}$	$\mathbf{P_p}$	**Predicted Response by RSM**	**Predicted Response by FEM**	**Desirability**
1	Minimize	Strain	0.1310	8	0.0013	0.0013	1.0000
2	Maximize	1st Natural Frequency	0.086600	2	102.3260	101.8250	1.0000

Table 4.6 – Multiobjective optimization of the ply drop-off location considering the strain minimization and natural frequency maximization simultaneously.

<table>
<tr><th>Objective</th><th>Response</th><th>$\mathbf{L_p}$</th><th>$\mathbf{P_p}$</th><th>Predicted Response by RSM</th><th>Predicted Response by FEM</th><th>Desirability</th></tr>
<tr><td>Minimize</td><td>Strain</td><td rowspan="2">0.1008</td><td rowspan="2">2</td><td>0.0013</td><td>0.0013</td><td rowspan="2">1.0000</td></tr>
<tr><td>Maximize</td><td>1st Natural Frequency</td><td>101.9964</td><td>101.3290</td></tr>
</table>

In the multiobjective optimization, the optimal ply drop-off location relative to the longitudinal position factor is 0.1008 meters, with this position being located between 5 and 6 panels, dropping-off at the second ply. As previously mentioned, the stacking sequence adopted for the beam was of $[45^o/90^o/-45^o/0^o/-45^o/0^o/45^o/90^o]_S$. Then the dropping-off of plies oriented at a 90º angle is most indicated in both optimization strategies, as can be confirmed in Table 4.5 and Table 4.6. This orientation is considered smoother, and when plies oriented at 90º are dropped on the thin end of the laminate beam, the stress concentration is reduced (VIDYASHANKAR and MURTY, 2001).

The optimal results obtained in the multiobjective optimization were presented using a Pareto front composed of non-dominated solutions, as shown in Figure 4.6. The Pareto front is able to provide a set of optimal solutions for both objectives, which are showed along the curve. The knee point is considered the point with the greatest convexity and is often located in the middle of the curve, representing the best combination of responses variables (ZHANG *et al.* 2020; ZOU *et al.* 2017).

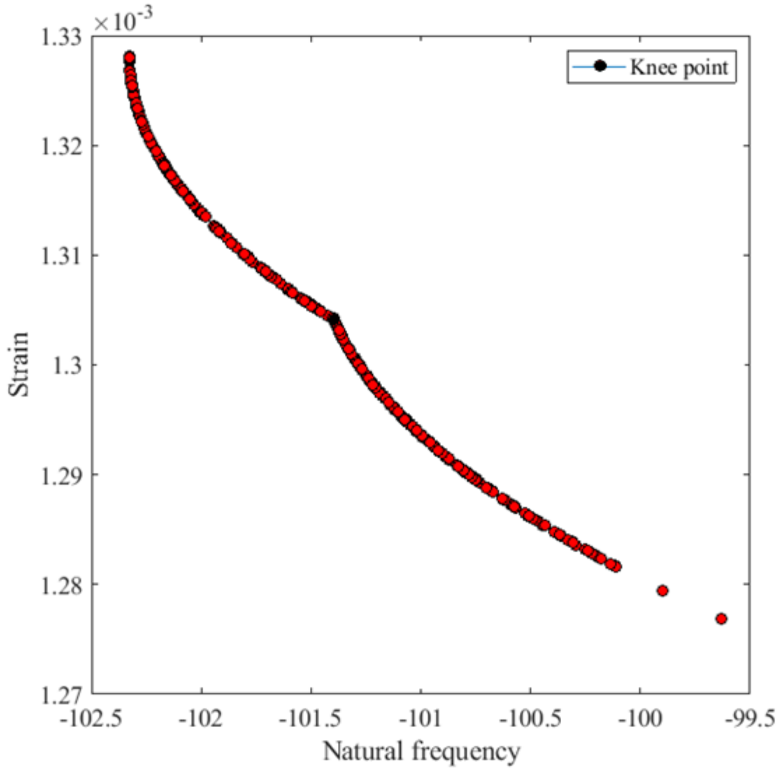

Figure 4.6 – Optimal solution found using a Pareto front considering the strain and natural frequency response variables for a cantilever beam with ply drop-offs.

The knee point showed the optimal response variable with a strain of 0.001304 and a natural frequency of 101.4 Hz. As one may observe by comparing the predicted response and the response generated using the FEM, the metamodel created demonstrated very appropriate results. To prove the accuracy of the results, merely replace the optimal design factors in the regression Equations (Equation 4.1 - 4.3), which will render response variables similar to the FEM responses. The optimal solution obtained by RSM is represented in Figure 4.7.

Figure 4.8 illustrates the optimal ply drop-off location on a laminate beam considering the optimized responses found by the metamodel using numerical simulation.

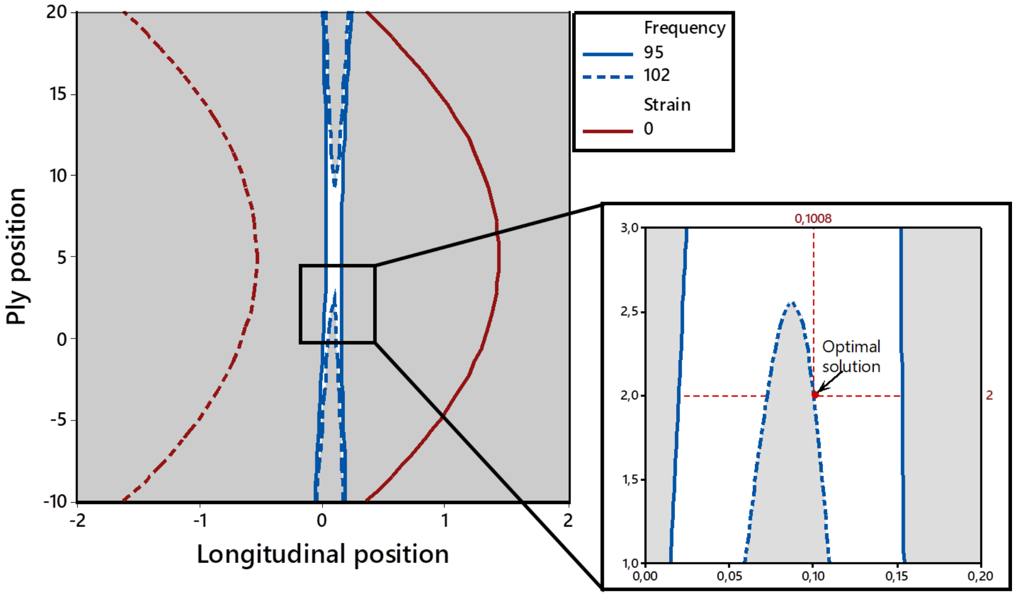

Figure 4.7 – Optimal solution for ply drop-off location on a cantilever beam considering the ply and longitudinal positions.

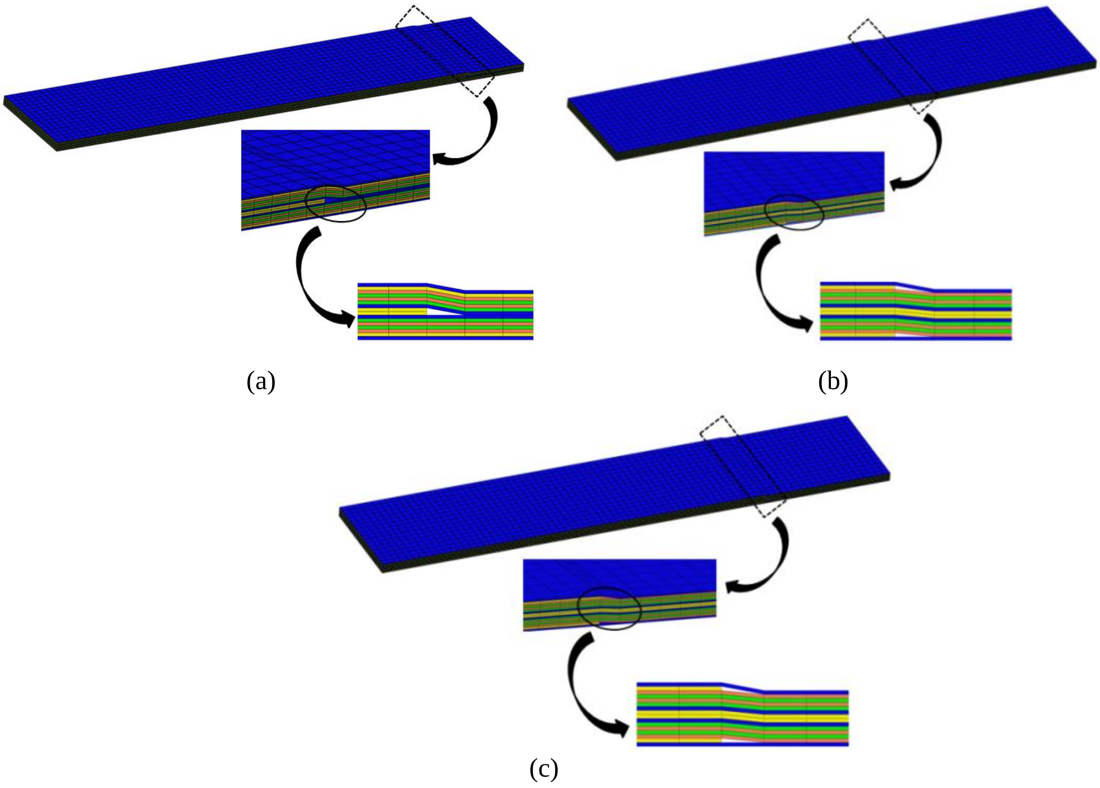

Figure 4.8 – Optimized cantilever beam considering the ply drop-off location: (a) mono-objective optimization with strain response variable, (b) mono-objective optimization with natural frequency response variable, and (c) multiobjective optimization (ply angle caption: ■ 0º ■ -45º ■ 45º ■ 90º).

Although the Tsai Wu failure criterion response variable does not offer a good interpretation of the problem related to ply drop-off location, the optimal parameters for the ply drop-off location in a cantilever beam found in the multiobjective optimization were used in a failure analysis with FEM considering the individualized plies, as shown in Figure 4.9.

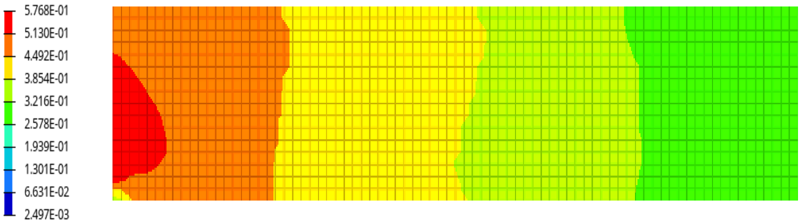

(a) Full laminate

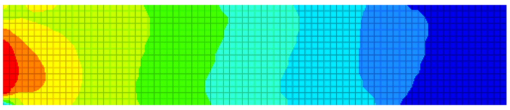

(b) ply #1 – 45º

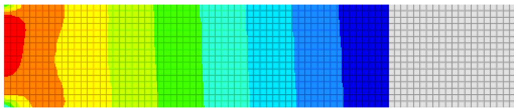

(c) ply #2 – 90º – **ply drop-off**

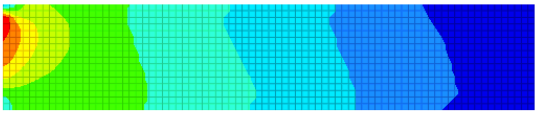

(d) ply #3 – -45º

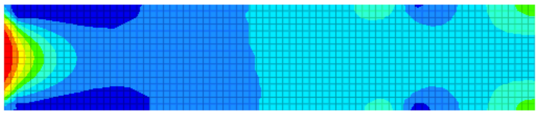

(e) ply #4 – 0º

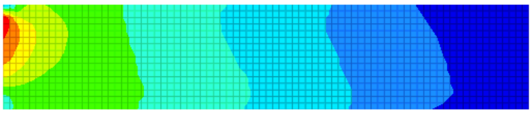

(f) ply #5 – -45º

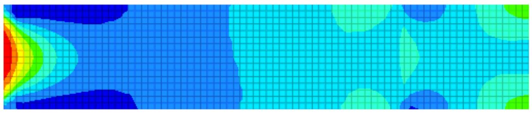

(g) ply #6 – 0º

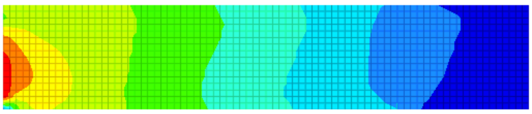

(h) ply #7 – 45º

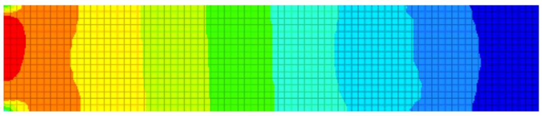

(i) ply #8 – 90º

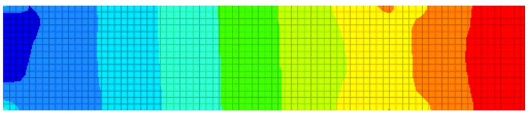

(j) ply #9 – 90º

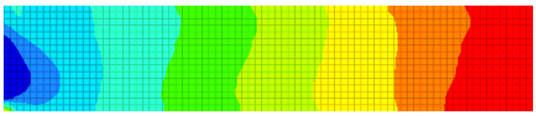

(k) ply #10 – 45º

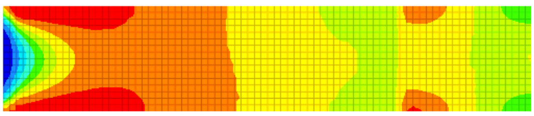

(l) ply #11 – 0º

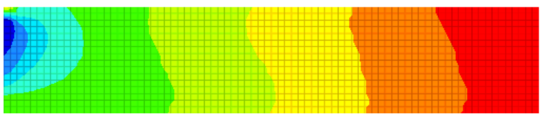

(m) ply #12 – -45º

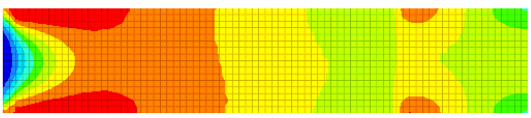

(n) ply #13 – 0º

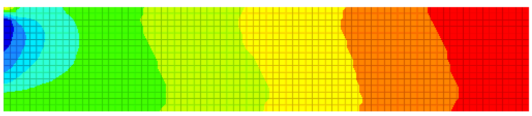

(o) ply #14 – -45º

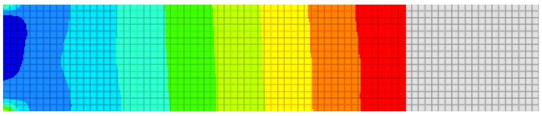

(p) ply #15 – 90º – **ply drop-off**

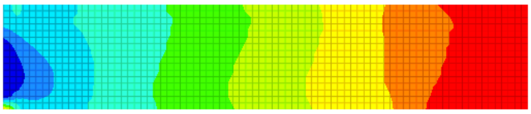

(q) ply #16 – 45º

Figure 4.9 – Plot of the failure criterion for each ply separately of a cantilever beam considering the optimal parameters obtained from the multiobjective optimization.

One may observe that, for the first eight plies, the failure criterion increased in the region near the fixed end, then, in the symmetrical part of the laminate beam, the failure criterion decreased in the region near the fixed end and increased at the beam end. Hence, it may be stated that the ply drop-off location does not influence the failure criterion, given that second ply was dropped, and the failure criterion changed after eighth ply, as shown in Figure 4.9. One possible reason for this is that the ply dropped is oriented at 90º, and when this type of ply is dropped, it presents low interlaminar stress, demonstrating a negligible effect on the stress distribution responsible for causing structural failure. Another fact that can justify the failure criterion is not influenced by ply drop-offs is the number of plies in relation to number of ply drop-offs considered limited. The laminate had 16 plies stacked, where only 2 were dropped.

4.2 Ply Drop-off Location Optimization in Hybrid CFRP/GFRP Composite Tubes Using Design of Experiments and SunFlower Optimization Algorithm

4.2.1 Numerical analyses considering the mass, failure criterion and buckling responses

The reduction in the structural mass when the 4 ply drop-offs are inserted into any region of the laminate considering the hybrid and non-hybrid tubular structures was confirmed by numerical simulations. The hybrid tapered tube presented a decrease in mass of 70% in relation to the hybrid tube without ply drop-offs. While the non-hybrid tapered tube provided a decrease in the mass by 80% due to the carbon fiber being lighter than glass fiber.

The Tsai-Wu failure index is evaluated in two conditions: torsion and compression, considering that these situations are more common in slender tubular structures. Due to the failure in compression being more common and frequently, the same is illustrated in Figure 4.10 and Figure 4.11, considering non-hybrid and hybrid tubes, respectively. In all failure analyses, the results were smaller than 1, highlighting how reliable the tubular tapered structure is. In most cases, the region close to the ply drop-off on the tubes demonstrated a slight increase in the intensity of the stress associated with failure, as can be seen in Figure 4.10 and Figure 4.11. This is due to the fact that the ply drop-off region stimulates stress concentrations (IRISARRI *et al.* 2014). The increase in the intensity of stress can be noted by an amendment in the color scale in each tubular structure, as can be seen in Figure 4.10 and Figure 4.11. For non-hybrid tapered tubes, the failure index values suffered an increase in the region close to the second ply drop-off in cases (c), (d), (g) and (h) and in the region close to both ply drop-offs in cases (a), (b), (e), (f), (i), (j), (m) and (n). For the cases (k), (l), (o) and (p), the use of ply drop-off in the non-hybrid tubular structures did not cause changes in failure index values. The intensity of stress remained stable, as can be confirmed in Figure 4.10. A reason for this can be justified due the most continuous plies, which were not dropped, had their fibers oriented at 90º in the same direction as the load, generating an increase in the laminate strength. However, when these plies oriented at 90º are dropped, as can be seen in cases (a), (b), (e) and (f) in Figure 4.10 and Figure 4.11, the failure index values have a significant increase in the posterior region to the second drop-off, and therefore the color scale of these structures is changed, generating higher failure index values. As previously mentioned, the stacking sequence adopted for the tubular structures was of $[45^o/90^o/90^o/-45^o/0^o]_S$.

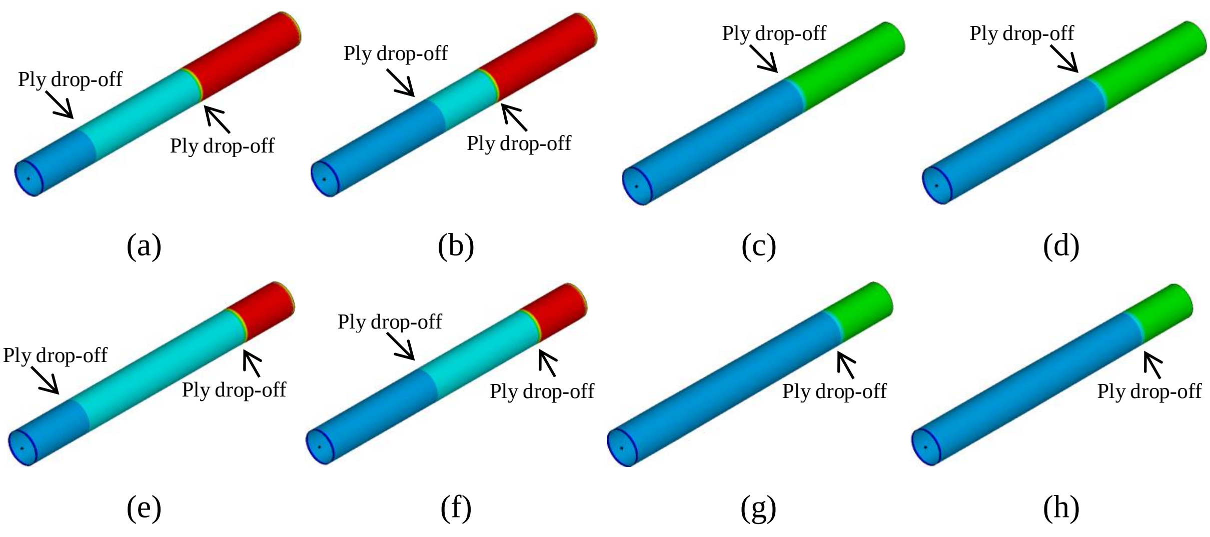

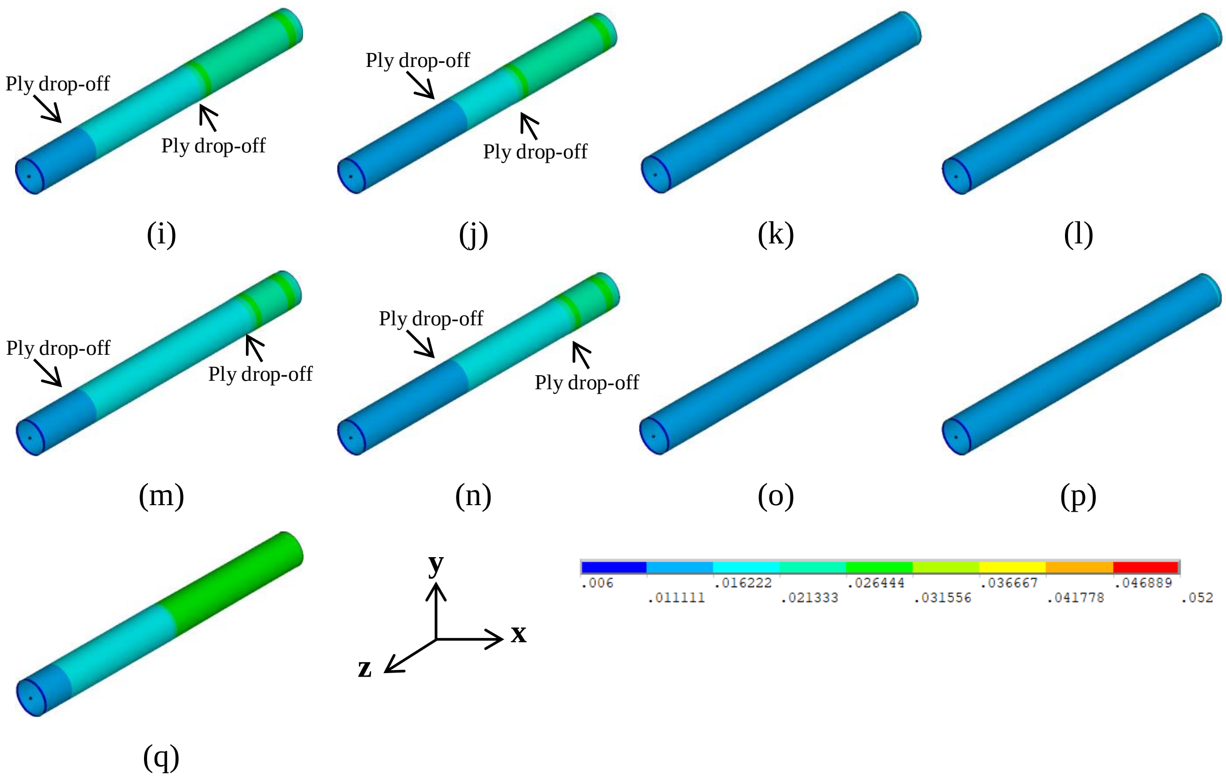

Figure 4.10 – Non-hybrid tubes considering failure in compression for ply drop-offs located in **(a)** $X_1 = 0.06$, $Y_1 = 2$, $X_2 = 0.18$ e $Y_2 = 3$, **(b)** $X_1 = 0.12$, $Y_1 = 2$, $X_2 = 0.18$ e $Y_2 = 3$, **(c)** $X_1 = 0.06$, $Y_1 = 4$, $X_2 = 0.18$ e $Y_2 = 3$, **(d)** $X_1 = 0.12$, $Y_1 = 4$, $X_2 = 0.18$ e $Y_2 = 3$, **(e)** $X_1 = 0.06$, $Y_1 = 2$, $X_2 = 0.24$ e $Y_2 = 3$, **(f)** $X_1 = 0.12$, $Y_1 = 2$, $X_2 = 0.24$ e $Y_2 = 3$, **(g)** $X_1 = 0.06$, $Y_1 =4$, $X_2 = 0.24$ e $Y_2 = 3$, **(h)** $X_1 = 0.12$, $Y_1 = 4$, $X_2 = 0.24$ e $Y_2 = 3$, **(i)** $X_1 = 0.06$, $Y_1 = 2$, $X_2 = 0.18$ e $Y_2 = 5$, **(j)** $X_1 = 0.12$, $Y_1 = 2$, $X_2 = 0.18$ e $Y_2 = 5$, **(k)** $X_1 = 0.06$, $Y_1 = 4$, $X_2 = 0.18$ e $Y_2 = 5$, **(l)** $X_1 = 0.12$, $Y_1 = 4$, $X_2 = 0.18$ e $Y_2 = 5$, **(m)** $X_1 = 0.06$, $Y_1 = 2$, $X_2 = 0.24$ e $Y_2 = 5$, **(n)** $X_1 = 0.12$, $Y_1 = 2$, $X_2 = 0.24$ e $Y_2 = 5$, **(o)** $X_1 = 0.06$, $Y_1 = 4$, $X_2 = 0.24$ e $Y_2 = 5$, **(p)** $X_1 = 0.12$, $Y_1 = 4$, $X_2 = 0.24$ e $Y_2 = 5$ e **(q)** $X_1 = 0.09$, $Y_1 = 3$, $X_2 = 0.21$ e $Y_2 = 4$.

The panel and ply design variables are represented by X and Y, respectively. Where X_1 and X_2 correspond to the first and second panels on which the ply drop-off is located, while Y_1 and Y_2 correspond to the first and second dropped ply. The FI values considering a hybrid tube with ply drop-offs can be assessed afterwards in section 4.4.2 of Table 4.7 in the second column that presents the failure in compression.

Again, the insertion of the ply drop-off in hybrid tubular structures caused changes in the intensity of stress in a manner similar to the non-hybrid tubular structures, except for the cases (k), (l), (o) and (p), where the failure index values had a smooth increase in the region close to the second ply drop-off, as can be observed in Figure 4.11. This fact is expected due to the hybrid structure being manufactured in large part with glass fibers, which provides a reduction in the structural strength. In addition, the region close to the second ply drop-off is more sensitive because of the significant reduction in the number of plies. It is worth remembering that the hybrid structures have only two plies manufactured in carbon fiber (external plies), while the non-hybrid structures are fully manufactured in carbon fiber.

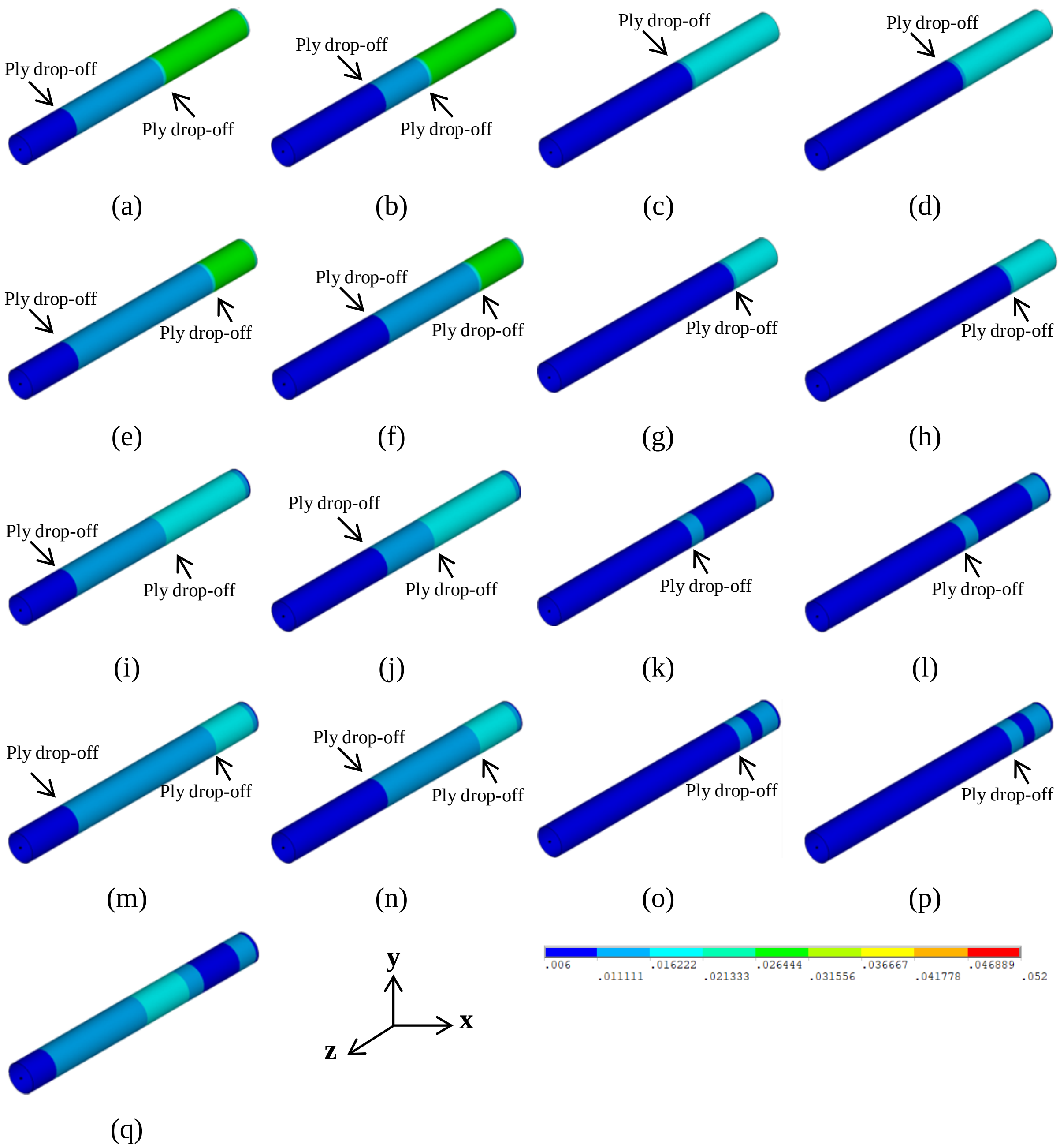

Figure 4.11 – Hybrid tubes considering failure in compression for ply drop-offs located in **(a)** $X_1 = 0.06$, $Y_1 = 2$, $X_2 = 0.18$ e $Y_2 = 3$, **(b)** $X_1 = 0.12$, $Y_1 = 2$, $X_2 = 0.18$ e $Y_2 = 3$, **(c)** $X_1 = 0.06$, $Y_1 = 4$, $X_2 = 0.18$ e $Y_2 = 3$, **(d)** $X_1 = 0.12$, $Y_1 = 4$, $X_2 = 0.18$ e $Y_2 = 3$, **(e)** $X_1 = 0.06$, $Y_1 = 2$, $X_2 = 0.24$ e $Y_2 = 3$, **(f)** $X_1 = 0.12$, $Y_1 = 2$, $X_2 = 0.24$ e $Y_2 = 3$, **(g)** $X_1 = 0.06$, $Y_1 = 4$, $X_2 = 0.24$ e $Y_2 = 3$, **(h)** $X_1 = 0.12$, $Y_1 = 4$, $X_2 = 0.24$ e $Y_2 = 3$, **(i)** $X_1 = 0.06$, $Y_1 = 2$, $X_2 = 0.18$ e $Y_2 = 5$, **(j)** $X_1 = 0.12$, $Y_1 = 2$, $X_2 = 0.18$ e $Y_2 = 5$, **(k)** $X_1 = 0.06$, $Y_1 = 4$, $X_2 = 0.18$ e $Y_2 = 5$, **(l)** $X_1 = 0.12$, $Y_1 = 4$, $X_2 = 0.18$ e $Y_2 = 5$, **(m)** $X_1 = 0.06$, $Y_1 = 2$, $X_2 = 0.24$ e $Y_2 = 5$, **(n)** $X_1 = 0.12$, $Y_1 = 2$, $X_2 = 0.24$ e $Y_2 = 5$, **(o)** $X_1 = 0.06$, $Y_1 = 4$, $X_2 = 0.24$ e $Y_2 = 5$, **(p)** $X_1 = 0.12$, $Y_1 = 4$, $X_2 = 0.24$ e $Y_2 = 5$ e **(q)** $X_1 = 0.09$, $Y_1 = 3$, $X_2 = 0.21$ e $Y_2 = 4$.

Based on the linear buckling analyses, the maximum critical load found for hybrid tubes with ply drop-offs was 31 kN and for non-hybrid tubes with ply drop-offs was 22 kN, making these loads much greater than the load applied of 4.480 kN. In order to achieve accurate results in relation to maximum buckling load, nonlinear analyses were generated, considering the linear buckling load as a stopping criterion for the algorithm. The nonlinear analyses revealed lower buckling loads than those calculated in linear buckling. Nevertheless, none of them was less than the applied compression load. Considering the nonlinear buckling analyses for hybrid tubes with ply drop-offs, the maximum buckling load achieved was 22.203 kN. It is possible to affirm that to maintain stability of the hybrid tapered tube, it is necessary to apply a load less than the nonlinear buckling load. A higher loading than this is necessary to begin the process of buckling in the structure, as can been seen in Figure 4.12.

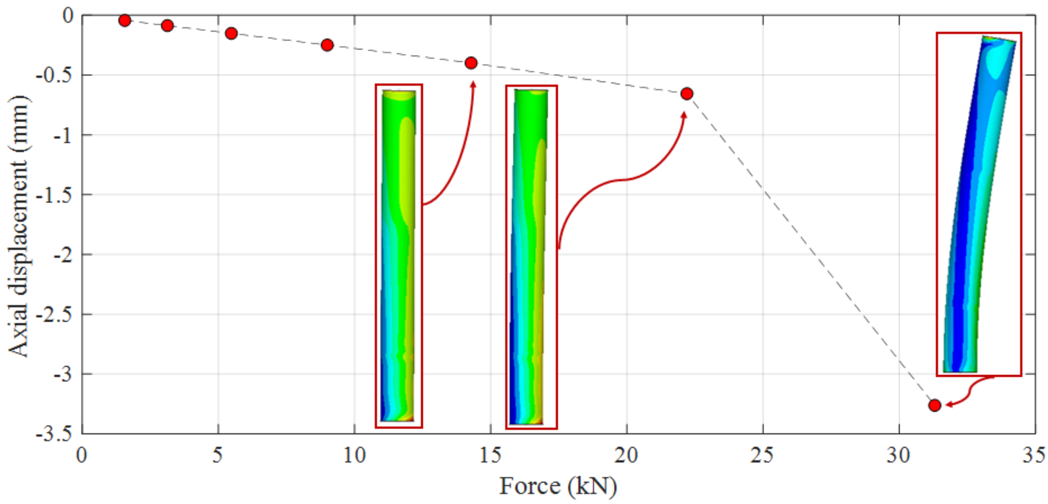

Figure 4.12 – Linear and nonlinear buckling analyses considering the maximum load supported by a hybrid tube with ply drop-offs.

It should be noted that for a hybrid tapered tubular structure, the maximum buckling load represents almost five times the load recommend by the 10328 ISO standard of 4.480 kN. In the case of the non-hybrid tubes, the maximum buckling load found is 16.173 kN, as depicted in Figure 4.13, almost four times greater than the compression load applied in the tubular structure. Therefore, it is proved that the load applied in compression will not cause buckling in the tubular structures with ply drop-offs and, additionally, a higher loading could be applied with security on the structures so that they will not suffer buckling.

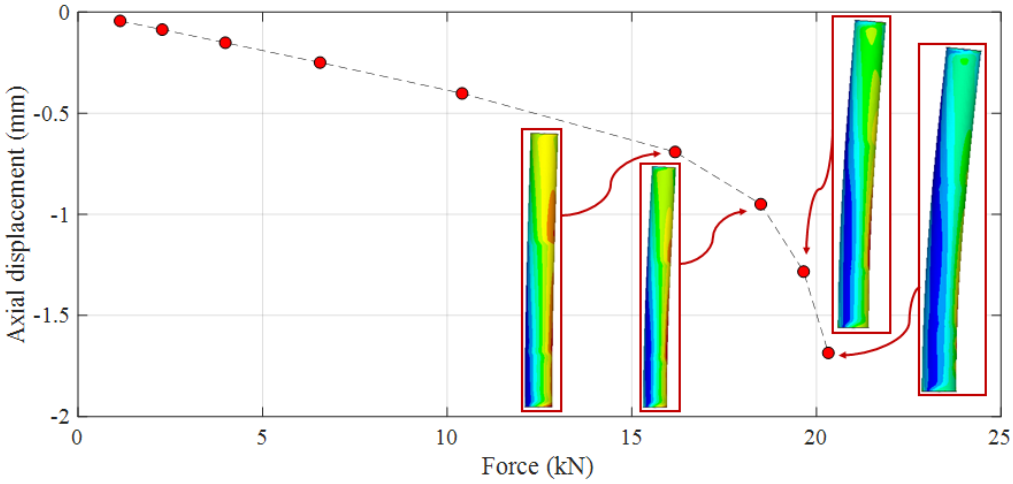

Figure 4.13 – Linear and nonlinear buckling analyses considering the maximum load supported by a non-hybrid tube with ply drop-offs.

Indeed, a buckling load greater for hybrid tubes compared to non-hybrid tubes was expected due to the glass fiber being thicker than carbon fiber. Furthermore, the hybrid tubes are only composed of two carbon layers, and the remainder is glass. In this way, the transversal section area where the load is applied tends to be thicker.

4.2.2 Factorial design and Response surface analyzed by Analysis of Variance

The factorial design was created, generating 17 different runs for tapered hybrid tubes. It is necessary to make a distinction between model curvatures, the last run represents the center point, where the component proportions are the averages of the vertex proportions in the design space, as can be seen in Table 4.7.

Table 4.7 – Factorial design experimental matrix for the hybrid tapered tubes considering the design factors related to ply drop-off location and structural responses.

	Design factors				Structural Responses				
Exp.	X_1	Y_1	X_2	Y_2	TW_t	TW_C	*ωn (Hz)*	*Mass (kg)*	*λ (N)*
1	0.06	2	0.18	3	0.04507	0.03074	145.69	0.1859	9363.86
2	0.12	2	0.18	3	0.04507	0.03075	140.64	0.1982	9505.68
3	0.06	4	0.18	3	0.09146	0.01860	186.13	0.1859	15038.80
4	0.12	4	0.18	3	0.09146	0.01860	179.68	0.1982	15180.60
5	0.06	2	0.24	3	0.04507	0.03074	159.54	0.1982	11776.10
6	0.12	2	0.24	3	0.04507	0.03075	154.07	0.2104	11988.50
7	0.06	4	0.24	3	0.09146	0.01860	198.74	0.1982	17734.40
8	0.12	4	0.24	3	0.09146	0.01860	191.92	0.2104	17947.20
9	0.06	2	0.18	5	0.04532	0.01867	193.04	0.1859	15393.60
10	0.12	2	0.18	5	0.04532	0.01862	186.72	0.1982	15819.10
11	0.06	4	0.18	5	0.10543	0.01155	224.91	0.1859	21068.40
12	0.12	4	0.18	5	0.10543	0.01155	217.36	0.1982	21352.20
13	0.06	2	0.24	5	0.04532	0.01862	197.80	0.1982	16386.70
14	0.12	2	0.24	5	0.04532	0.01862	191.38	0.2104	16812.20
15	0.06	4	0.24	5	0.10546	0.01155	228.55	0.1982	21848.70
16	0.12	4	0.24	5	0.10546	0.01155	220.94	0.2104	22203.40
17	0.09	3	0.21	4	0.10581	0.01805	221.11	0.1737	17379.70

where TW_t and TW_C represent the Tsai-Wu failure criterion or FI in torsion and compression, respectively, ωn is 1st natural frequency and λ the nonlinear buckling load.

An ANOVA is generated by factorial design with the goal of revealing the significance level and curvature parameters. The curvature can be represented by the addition of an interaction term in a first-order model, making it possible to determine the model fit of the system. As can be seen in Table 4.8, it can be inferred that the Tsai-Wu failure criterion in compression and buckling load responses ensure an excellent quality of fit with an R^2_{adj} of 99.49% and 99.08%, respectively. The mass response showed a low fit with R^2_{adj} less than 70%.

Table 4.8 – Results of the R^2_{adj} considering the response variables about the structural behavior of hybrid tubes with ply drop-offs.

Responses	**R^2**	**R^2_{adj}**	**$R^2_{(pred)}$**
TW_T (torsion)	88.47%	87.70%	86.40%
TW_C (compression)	99.59%	99.49%	99.52%
ω_n	86.86%	84.98%	83.12%
Mass	68.00%	63.43%	63.7%
Nonlinear buckling λ	99.31%	99.08%	99.01%

According to factorial design results, a RSM was created, considering the responses more significant, such as the Tsai-Wu failure criterion in compression and buckling load. As depicted in Table 4.9, the design variables for the design matrix using the RSM were the same as considered in the factorial design with the addition of a categorical variable (hybrid), which is responsible for determining if the structure is hybrid or not.

Table 4.9a – Design matrix created to analyze the response surface considering the ply drop-off location (part I).

	Design variables					**Structural Responses**	
	X_1	***Y_1***	***X_2***	***Y_2***	***Hybrid***	***TW_C***	***λ (N)***
1	0.06	2	0.18	3	Yes	0.03074	9363.86
2	0.12	2	0.18	3	Yes	0.03075	9505.68
3	0.06	4	0.18	3	Yes	0.01860	15038.80
4	0.12	4	0.18	3	Yes	0.01860	15180.60
5	0.06	2	0.24	3	Yes	0.03074	11776.10
6	0.12	2	0.24	3	Yes	0.03075	11988.50
7	0.06	4	0.24	3	Yes	0.01860	17734.40
8	0.12	4	0.24	3	Yes	0.01860	17947.20
9	0.06	2	0.18	5	Yes	0.01867	15393.60
10	0.12	2	0.18	5	Yes	0.01862	15819.10
11	0.06	4	0.18	5	Yes	0.01155	21068.40
12	0.12	4	0.18	5	Yes	0.01155	21352.20
13	0.06	2	0.24	5	Yes	0.01862	16386.70
14	0.12	2	0.24	5	Yes	0.01862	16812.20
15	0.06	4	0.24	5	Yes	0.01155	21848.70
16	0.12	4	0.24	5	Yes	0.01155	22203.40
17	0.09	3	0.21	4	Yes	0.01805	17379.70
18	0.09	3	0.21	4	Yes	0.01805	17379.70
19	0.09	3	0.21	4	Yes	0.01805	17379.70
20	0.09	3	0.21	4	Yes	0.01805	17379.70
21	0.06	2	0.18	3	No	0.05210	5533.16
22	0.12	2	0.18	3	No	0.05209	5604.15
23	0.06	4	0.18	3	No	0.03022	10215.00
24	0.12	4	0.18	3	No	0.03023	10286.00

Table 4.9b – Design matrix created to analyze the response surface considering the ply drop-off location (part II).

	Design variables					Structural Responses	
	X_1	Y_1	X_2	Y_2	*Hybrid*	TW_C	λ *(N)*
25	0.06	2	0.24	3	No	0.05210	7235.70
26	0.12	2	0.24	3	No	0.05209	7377.68
27	0.06	4	0.24	3	No	0.03022	12201.30
28	0.12	4	0.24	3	No	0.03023	12343.20
29	0.06	2	0.18	5	No	0.02700	11137.20
30	0.12	2	0.18	5	No	0.02702	11421.10
31	0.06	4	0.18	5	No	0.01641	15819.10
32	0.12	4	0.18	5	No	0.01641	16031.90
34	0.12	2	0.24	5	No	0.02702	11775.80
35	0.06	4	0.24	5	No	0.01641	15961.00
36	0.12	4	0.24	5	No	0.01641	16244.70
37	0.09	3	0.21	4	No	0.03008	9363.75
38	0.09	3	0.21	4	No	0.03008	9363.75
39	0.09	3	0.21	4	No	0.03008	9363.75
40	0.09	3	0.21	4	No	0.03008	9363.75
41	0.06	3	0.21	4	Yes	0.01860	14258.40
42	0.12	3	0.21	4	Yes	0.01860	14400.30
43	0.09	2	0.21	4	Yes	0.01874	13832.80
44	0.09	4	0.21	4	Yes	0.01158	20713.80
45	0.09	3	0.18	4	Yes	0.01874	13832.80
46	0.09	3	0.24	4	Yes	0.01484	16386.60
47	0.09	3	0.21	3	Yes	0.03091	8725.36
48	0.09	3	0.21	5	Yes	0.01867	15038.80
49	0.09	3	0.21	4	Yes	0.01874	13832.80
50	0.09	3	0.21	4	Yes	0.01874	13832.80
51	0.06	3	0.21	4	No	0.03023	9647.51
52	0.12	3	0.21	4	No	0.03023	9718.45
53	0.09	2	0.21	4	No	0.03008	9363.77
54	0.09	4	0.21	4	No	0.01642	15677.20
55	0.09	3	0.18	4	No	0.03008	9647.51
56	0.09	3	0.24	4	No	0.03008	10073.10
57	0.09	3	0.21	3	No	0.05418	5107.54
58	0.09	3	0.21	5	No	0.02721	10924.40
59	0.09	3	0.21	4	No	0.03008	9363.75
60	0.09	3	0.21	4	No	0.03008	9363.75

Proceeding in a similar manner, Table 4.10 and Table 4.11 show the quality of fit obtained by the RSM through an ANOVA. While that, the relevance of variables can be seen in Figure 4.14 with Pareto charts, show the importance of each variable and their interactions in relation to the Tsai-Wu failure criterion and buckling load response variables.

Table 4.10 – Results of the ANOVA for Tsai-Wu failure criterion response variable in compression conditions.

Source	**DF**	**Adj SS**	**Adj MS**	**F-Value**	**P-Value**
Model	20	0.006451	0.000323	134.29	0.000
Blocks	1	0.000002	0.000002	0.70	0.407
Linear	5	0.005569	0.001114	463.73	0.000
X1	1	0.000000	0.000000	0.00	0.999
Y1	1	0.001439	0.001439	599.16	0.000
X2	1	0.000000	0.000000	0.18	0.673
Y2	1	0.002047	0.002047	852.05	0.000
Hybrid	1	0.002083	0.002083	867.25	0.000
Square	4	0.000402	0.000101	41.87	0.000
X1*X1	1	0.000000	0.000000	0.04	0.845
Y1*Y1	1	0.000145	0.000145	60.32	0.000
X2*X2	1	0.000006	0.000006	2.60	0.115
Y2*Y2	1	0.000341	0.000341	141.97	0.000
2-Way Interaction	10	0.000476	0.000048	19.82	0.000
X1*Y1	1	0.000000	0.000000	0.00	1.000
X1*X2	1	0.000000	0.000000	0.00	0.996
X1*Y2	1	0.000000	0.000000	0.00	0.996
X1*Hybrid	1	0.000000	0.000000	0.00	0.995
Y1*X2	1	0.000000	0.000000	0.00	0.996
Y1*Y2	1	0.000133	0.000133	55.56	0.000
Y1*Hybrid	1	0.000098	0.000098	40.88	0.000
X2*Y2	1	0.000000	0.000000	0.00	0.996
X2*Hybrid	1	0.000000	0.000000	0.18	0.673
Y2*Hybrid	1	0.000244	0.000244	101.58	0.000
Error	39	0.000094	0.000002		
Lack-of-Fit	31	0.000094	0.000003	*	*
PureError	8	0.000000	0.000000		
Total	59	0.006545			
R^2	98.57%	R^2_{adj}	97.83%	$R^2_{(pred)}$	96.52%

Table 4.11 – Results of the ANOVA for buckling load response variable considering a nonlinear buckling.

Source	**DF**	**Adj SS**	**Adj MS**	**F-Value**	**P-Value**
Model	20	1018016307	50900815	83.38	0.000
Blocks	1	11373780	11373780	18.63	0.000
Linear	5	927896939	185579388	304.00	0.000
X1	1	438295	438295	0.72	0.402
Y1	1	256633992	256633992	420.39	0.000
X2	1	18015950	18015950	29.51	0.000
Y2	1	242814670	242814670	397.75	0.000
Hybrid	1	409994033	409994033	671.61	0.000
Square	4	50924733	12731183	20.85	0.000
X1*X1	1	232269	232269	0.38	0.541
Y1*Y1	1	36378416	36378416	59.59	0.000
X2*X2	1	356379	356379	0.58	0.449
Y2*Y2	1	26184681	26184681	42.89	0.000
2-Way Interaction	10	9674352	967435	1.58	0.148
X1*Y1	1	3925	3925	0.01	0.937
X1*X2	1	7693	7693	0.01	0.911
X1*Y2	1	69379	69379	0.11	0.738
X1*Hybrid	1	13932	13932	0.02	0.881
Y1*X2	1	7690	7690	0.01	0.911
Y1*Y2	1	151108	151108	0.25	0.622
Y1*Hybrid	1	1913205	1913205	3.13	0.084
X2*Y2	1	5499528	5499528	9.01	0.005
X2*Hybrid	1	1600394	1600394	2.62	0.113
Y2*Hybrid	1	407497	407497	0.67	0.419
Error	39	23808208	610467		
Lack-of-Fit	31	23808208	768007	*	*
PureError	8	0	0		
Total	59	1041824515			
R^2	97.71%	R^2_{adj}	96.54%	$R^2_{(pred)}$	96.32%

Clearly, the Tsai-Wu failure criterion and buckling load represent high predictive capability, as long as the R^2_{adj} is above 95%, as shown in the ANOVA results in Table 4.10 and Table 4.11. The *p-value* generated by ANOVA for the Tsai-Wu failure criterion demonstrated that there exists a statistically significant relationship between the Y_1, X_2, Y_2 and hybrid design variables with this response variable. The X_2 design variable did not demonstrate any relation to response variables, their *p-value* being above 0.05, as can be confirmed by Table 4.10. While for the buckling load response variable, the Y_1, Y_2 and hybrid design variables had *p-value* less than 0.05, demonstrating the significance between design and response variables, as depicted in Table 4.11. In this case, the X_1 and X_2 design variables demonstrated that there is no significance between the design and response variables. As can be observed for both response variables, the X_2 design variable related to the second drop-off position on the panel had a *p-value* above 0.05, demonstrating that this variable is not significant for the failure criterion and buckling load responses.

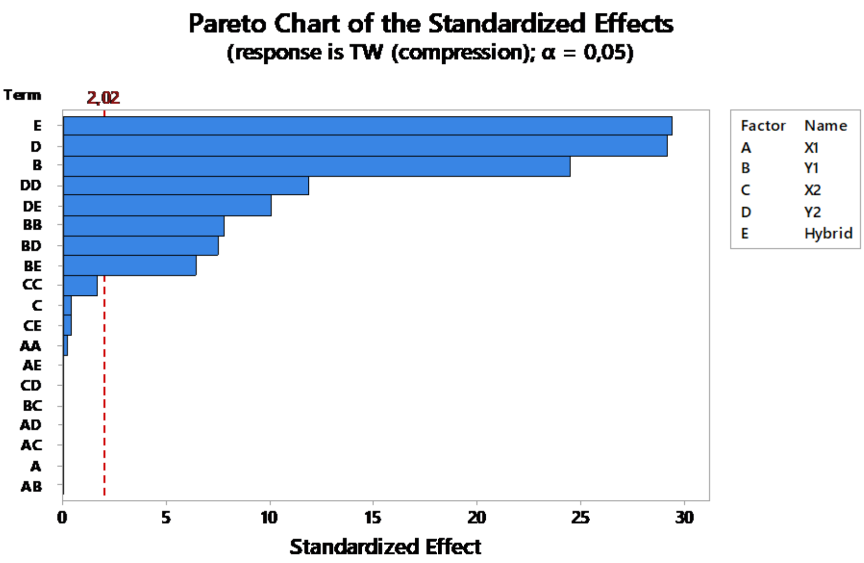

(a)

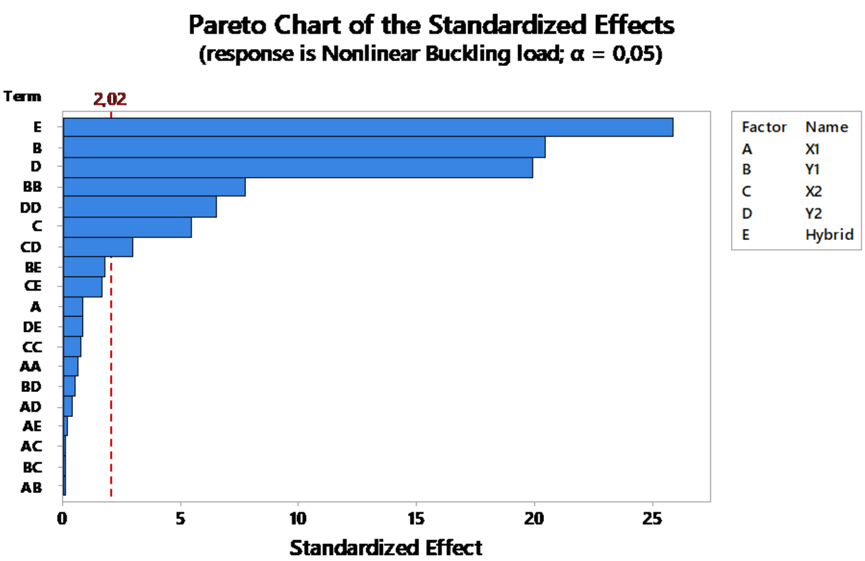

(b)

Figure 4.14 – Pareto charts considering the effects of the response variables: (a) Tsai-Wu failure

criterion in compression conditions and (b) nonlinear buckling load.

These important results show that the Y_1, Y_2, hybrid design variables and their interactions present a noticeable influence on the ply drop-off location, interfering directly with all the response variables. The X_2 variable and its interactions with the Y_2 variable demonstrated relevance for the buckling load response variable with a *p-value* lower than 0.05.

As shown in Figure 4.15, the quadratic plots of the main effects were developed in accordance with the changes in variable level from low to high, demonstrating how much each design variable interferes with the responses.

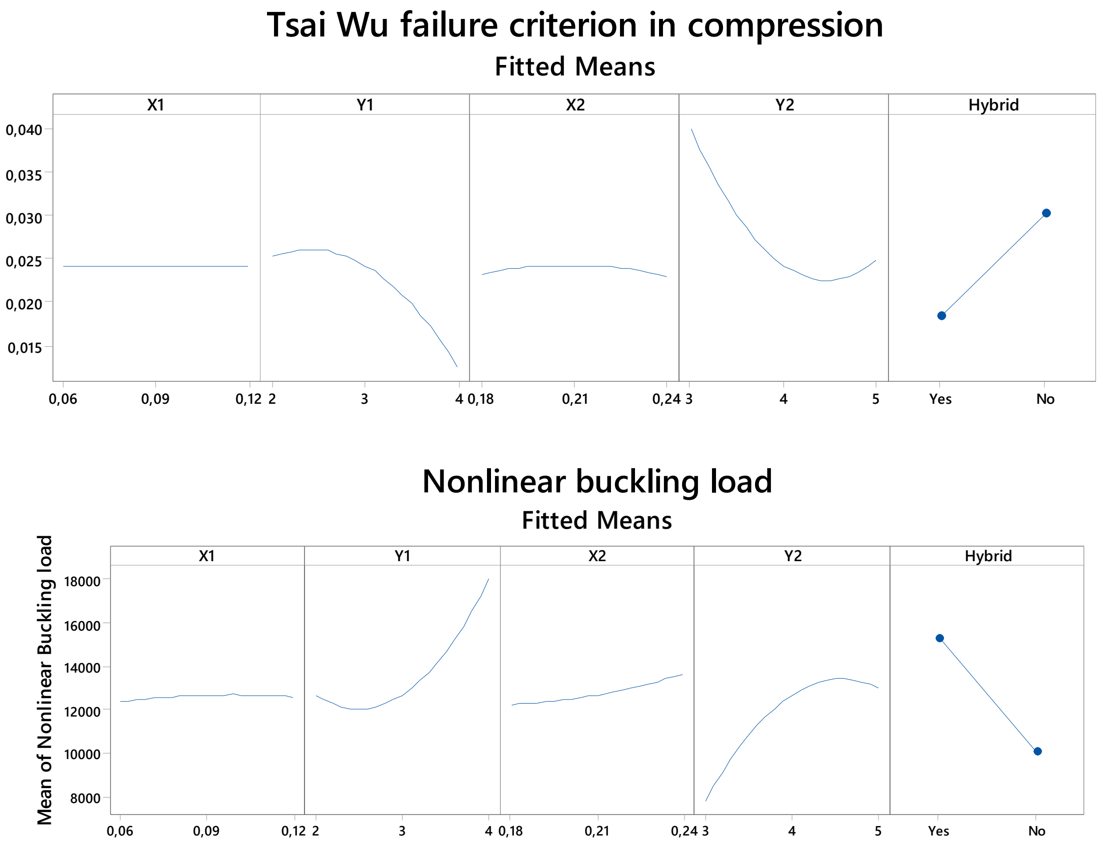

Figure 4.15 – Main effects plot for Tsai-Wu failure criterion and buckling load response variables considering the ply drop-off location.

The horizontal line reveals that the main effect is low for the case of the variable X_1 in both responses and X_2 for the Tsai-Wu failure criterion response variable. The slightly sloped line for the X_2 variable demonstrates that there is a little influence of the variable in the buckling load response. Also, the main effect of the hybrid variable is the highest, followed by the *Y* variable. This situation has already been revealed in the ANOVA results and Pareto charts in Figure 4.14. Therefore, it is possible to prove that the hybrid variable is decisive for the optimal performance of tubes with ply drop-offs.

The following second-order model was formulated using the ANOVA based on the significant response variables distinguishing between hybrid and non-hybrid tubes, as depicted in Equations 4.4 - 4.7.

$$TW_{C\ (HYBRID)} = \begin{gathered} 0.1056 + 0.027 X_1 + 0.01920 Y_1 + 0.511 X_2 - 0.07661 Y_2 \\ - 0.151 X_1{*}X_1 - 0.005342 Y_1{*}Y_1 - 1.233 X_2{*}X_2 \\ + 0.008196 Y_2{*}Y_2 + 0.00000 X_1{*}Y_1 + 0.001 X_1{*}X_2 - \\ 0.00004 X_1{*}Y_2 + 0.00005 Y_1{*}X_2 + 0.002042 Y_1{*}Y_2 - \\ 0.00005 X_2{*}Y_2 \end{gathered} \tag{4.4}$$

$$TW_{C} = \begin{gathered} 0.1466 + 0.027 X_1 + 0.01590 Y_1 + 0.518 X_2 - 0.08182 Y_2 \\ - 0.151 X_1{*}X_1 - 0.005342 Y_1{*}Y_1 - 1.233 X_2{*}X_2 \\ + 0.008196 Y_2{*}Y_2 + 0.00000 X_1{*}Y_1 + 0.001 X_1{*}X_2 - \\ 0.00004 X_1{*}Y_2 + 0.00005 Y_1{*}X_2 + 0.002042 Y_1{*}Y_2 - \\ 0.00005 X_2{*}Y_2 \end{gathered} \tag{4.5}$$

$$\lambda_{(HYBRID)} = \begin{gathered} -23526 + 38393 X_1 - 12961 Y_1 - 40858 X_2 + 23840 Y_2 - \\ 237658 X_1{*}X_1 + 2677 Y_1{*}Y_1 + 294383 X_2{*}X_2 - 2271 Y_2{*}Y_2 - \\ 369 X_1{*}Y_1 + 17228 X_1{*}X_2 + 1552 X_1{*}Y_2 + 517 Y_1{*}X_2 - \\ 69 Y_1{*}Y_2 - 13819 X_2{*}Y_2 \end{gathered} \tag{4.6}$$

$$\lambda = \begin{gathered} -23450 + 37082 X_1 - 13422 Y_1 - 54915 X_2 + 23627 Y_2 - \\ 237658 X_1{*}X_1 + 2677 Y_1{*}Y_1 + 294383 X_2{*}X_2 - 2271 Y_2{*}Y_2 - \\ 369 X_1{*}Y_1 + 17228 X_1{*}X_2 + 1552 X_1{*}Y_2 + 517 Y_1{*}X_2 - \\ 69 Y_1{*}Y_2 - 13819 X_2{*}Y_2 \end{gathered} \tag{4.7}$$

Based on the equations of regression mentioned above, it has become possible to create a metamodel that determines the relationship between the responses and the combinations of design variable levels. Furthermore, the regression model allows creating quadratic surface plots that illustrate the relationship between the fitted response and two variables, as shown in Figure 4.16 and Figure 4.17.

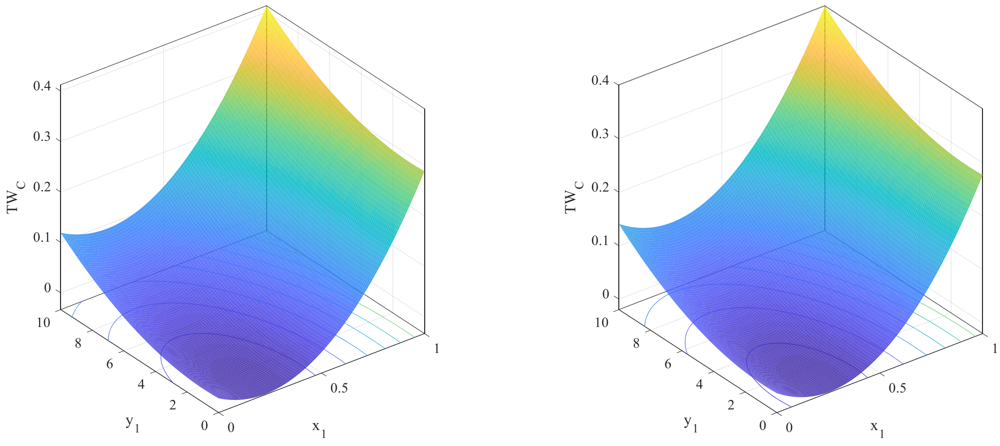

(a) TW_C (fixed at X_2=0.21 Y_2=4) (b) TW_C hybrid (fixed at X_2=0.21 Y_2=4)

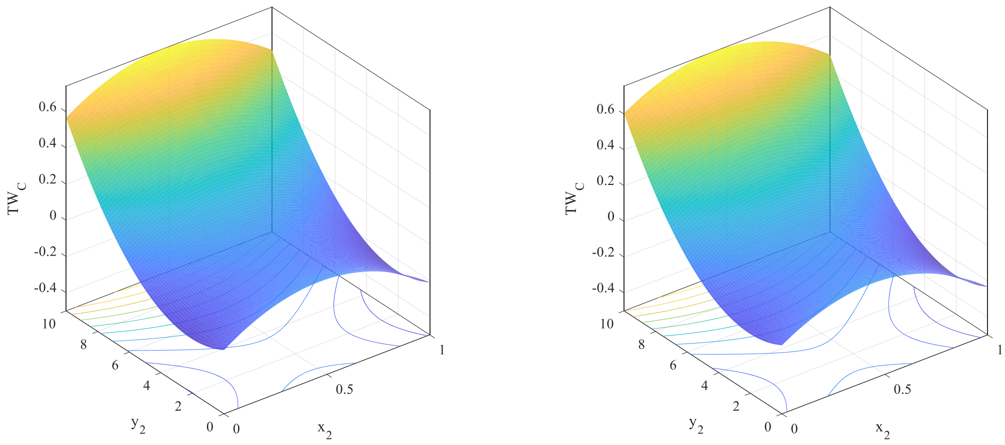

(c) TW_C (fixed at X_1=0.09 Y_1=3) (d) TW_C hybrid (fixed at X_1=0.09 Y_1=3)

Figure 4.16 – Surface plot of the Tsai-Wu failure criterion response variable considering: (a) the X_2 and Y_2 design variables for the non-hybrid tube, (b) the X_2 and Y_2 design variables for the hybrid tube, (c) the X_1 and Y_1 design variables for the non-hybrid tube and (d) the X_1 and Y_1 design variables for the hybrid tube.

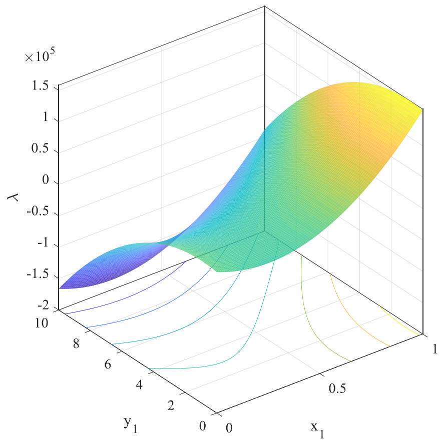

(a) λ (fixed at X_2=0.21 Y_2=4)

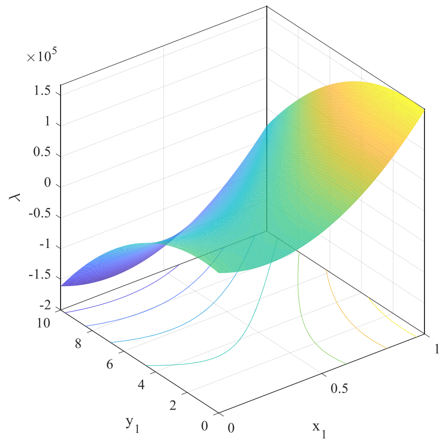

(b) λ hybrid (fixed at X_2=0.21 Y_2=4)

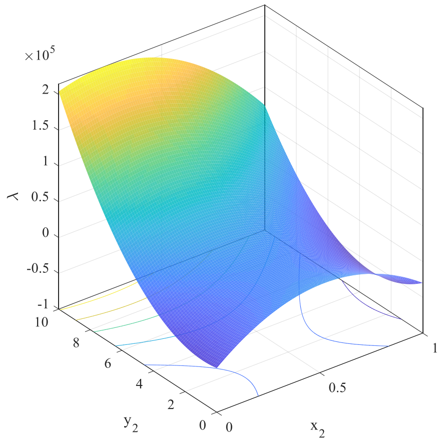

(c) λ (fixed at X_1=0.09 Y_1=3)

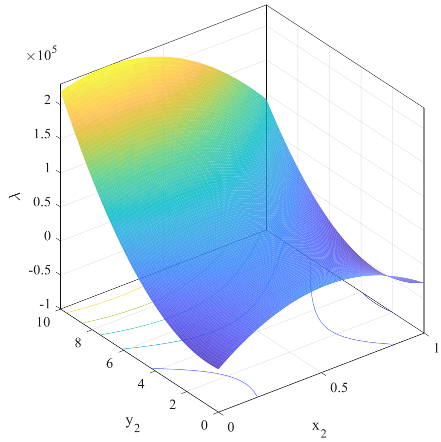

(d) λ hybrid (fixed at X_1=0.09 Y_1=3)

Figure 4.17 – Surface plot of the nonlinear buckling load considering: (a) the X_2 and Y_2 design variables for the non-hybrid tube, (b) the X_2 and Y_2 design variables for the hybrid tube, (c) the X_1 and Y_1 design variables for the non-hybrid tube and (d) the X_1 and Y_1 design variables for the hybrid tube.

The surface plots are very efficient for indicating the fitted responses considering the optimum region where the minimum point for Tsai-Wu failure criterion and the maximum point for buckling load are located, as can be seen in Figure 4.16 and Figure 4.17. It is possible to see that the behavior for failure criterion in the hybrid and non-hybrid tubes is very similar in cases (a) and (b), while for the cases (c) and (d), there is a small difference, as shown in Figure 4.16. In relation to the buckling load, all the cases revealed a small difference, as depicted in Figure 4.17. For failure criterion response, cases (a) and (b) tend to be more parabolic than in other cases, while for buckling load, all cases tend to be a little linear, as can be seen in Figure 4.17.

4.2.3 Optimization using the metamodel-based SunFlower optimization algorithm

A multiobjective optimization is developed aiming at the best ply drop-offs location that maximizes the buckling load and minimizes the *FI*. The constrained nonlinear optimization problem can be formulated considering the metamodel obtained with the composite tubes with ply drop-offs, as can be seen in Equations 4.8 - 4.17.

$$i)\ Minimize\ TW_C(\mathbf{x}) \tag{4.8}$$

$$ii)\ Maximize\ \lambda(\mathbf{x}) \tag{4.9}$$

$$iii)\ Minimize\ TW(\mathbf{x})\ \&\ Maximize\ \lambda(\mathbf{x}) \tag{4.10}$$

$$Subject\ to:\ g(x):\ \mathbf{x}^T\mathbf{x} \leq \alpha \tag{4.11}$$

$$0.06 \leq x_1 \leq 0.12 \tag{4.12}$$

$$2 \leq x_2 \leq 4 \tag{4.13}$$

$$0.18 \leq x_3 \leq 0.24 \tag{4.14}$$

$$3 \leq x_4 \leq 5 \tag{4.15}$$

$$x_5 = \{no, yes\} \tag{4.16}$$

$$\mathbf{x} = \{x_1, x_2, x_3, x_4, x_5\} \tag{4.17}$$

Now the ply positions are represented by x_2 and x_4, while the hybrid categorical variable is represented by x_5. Meanwhile, the limits laid down for the ply and longitudinal positions are the same. The problem was tackled according to three different optimization backgrounds: *i)* Tsai-Wu failure index mono-objective optimization (Equation 4.8), *ii)* buckling load mono-objective optimization (Equation 4.9) and *iii)* both response multiobjective optimization (Equation 4.10). In all optimization cases, a nonlinear constrained spherical Equation is incorporated to ensure that the optimal is always in the viable region (Equation 4.11). The lateral limits are defined according to Equations 4.12 to 4.16. It is important to note that decision variables x_1 and x_3 are continuous, x_2 and x_4 are discrete, and x_5 is categorical.

In addition, we can optimize the better ply drop-off location using the SFO algorithm considering the following parameters depicted in Table 4.12.

Table 4.12 – Main parameters used in the SunFlower optimization algorithm to identify the best ply drop-off location.

Population	200 individuals
Pollination rate	10%
Mortality	10%
Survival rate	80%
Maximum number of iterations (stop criterion)	100

The maximum number of iterations was defined as the stopping criterion. The results of the multiobjective optimization were exposed using a Pareto front composed of non-dominated solutions. In this study, there are two conflicting cases (objectives), i.e., buckling load and TW_C, especially when considering the 5th design variable (hybrid categorical variable), which gives the information on whether the structure must be hybrid or not (Figure 4.15). In this sense, the optimization considered the responses alone in a mono-objective optimization and, subsequently, in a multiobjective optimization, considered both responses at the same time, as can be seen in Table 4.13 and Table 4.14.

Table 4.13 – Mono-objective optimization for the better ply drop-off location in a tubular structure aims to minimize the failure criterion and maximize the buckling load, separately.

Case	Objective	Response	x_1	x_2	x_3	x_4	x_5	Predicted Response
1	Minimize	TW_C	0.06	4	0.24	4.17	Yes	0.006742
2	Maximize	λ	0.10	4	0.24	4.49	Yes	-22.6619 kN

Table 4.14 – Multiobjective optimization for the better ply drop-off location in a tubular structure aims to minimize the failure criterion and maximize the buckling load, simultaneously.

Case	Objective	Response	x_1	x_2	x_3	x_4	x_5	Predicted Response
3	Minimize	TW_C	0.1085	4	0.2398	4.23	yes	0.0071
	Maximize	λ						-22.0825 kN

Complementarily, Figures 4.18 and 4.19 show the convergence curves for the two mono-objective cases studied. It is observed that the problem converged properly and the parameters used in the optimizer were adequate.

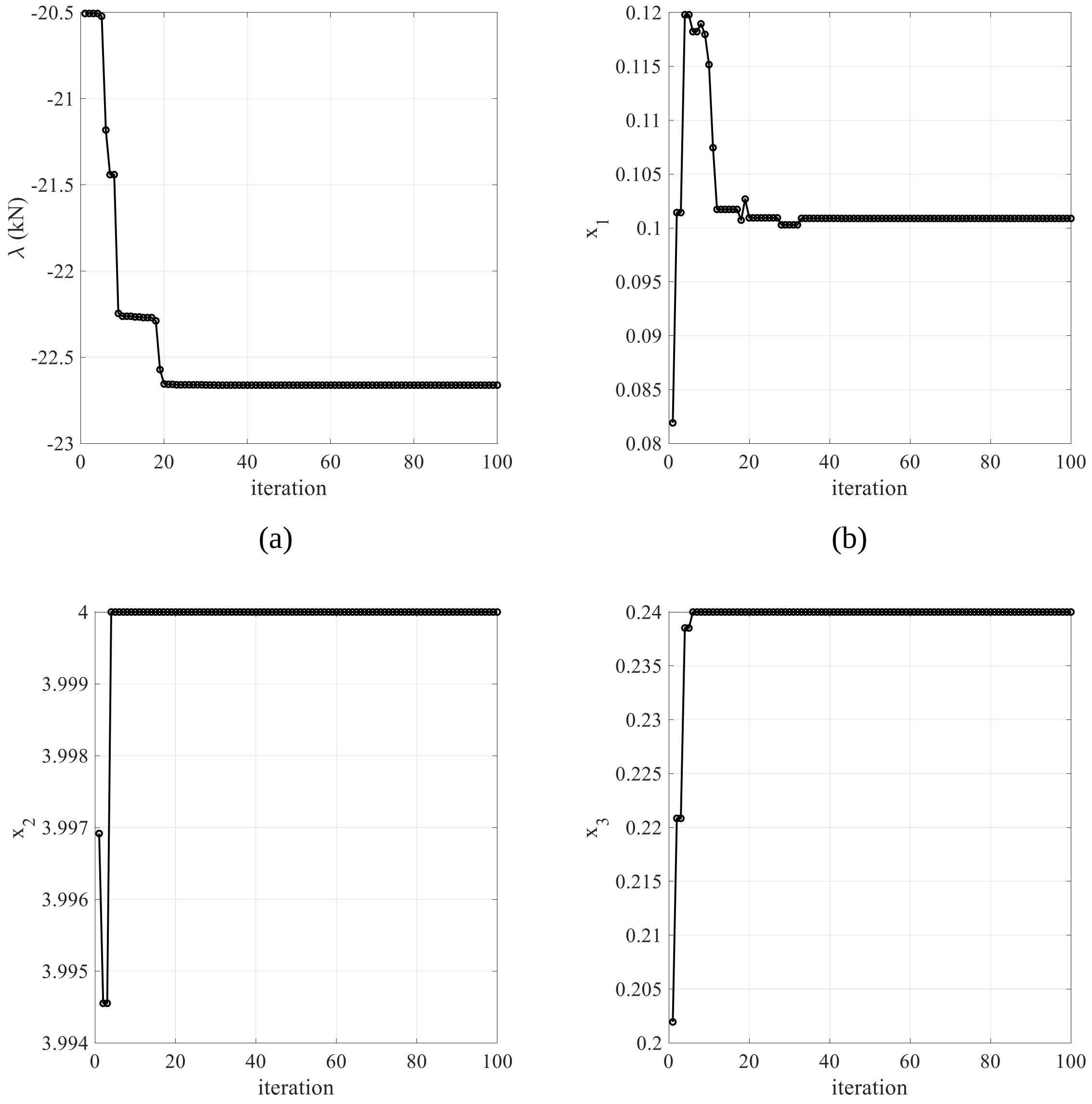

(a) (b) (c) (d)

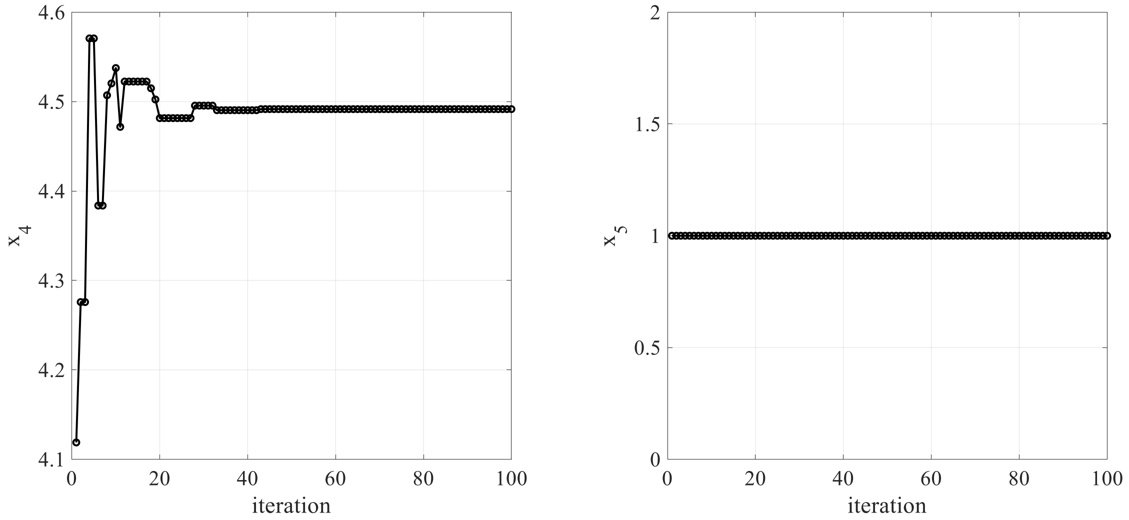

(e) (f)

Figure 4.18 – Optimization converge results for the case I (buckling): objective function (a) and design variables (b)-(f).

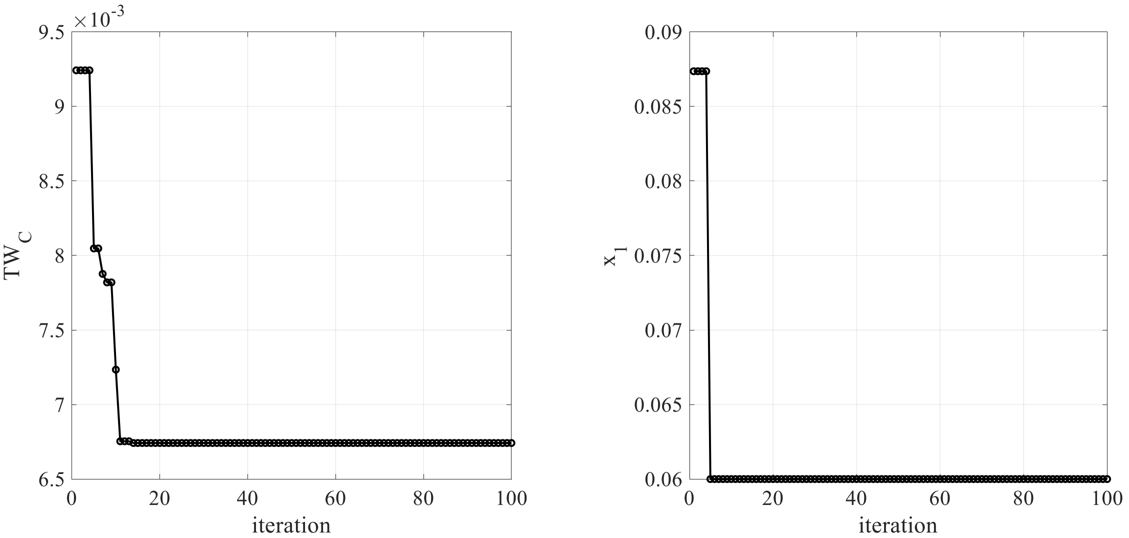

(a) (b)

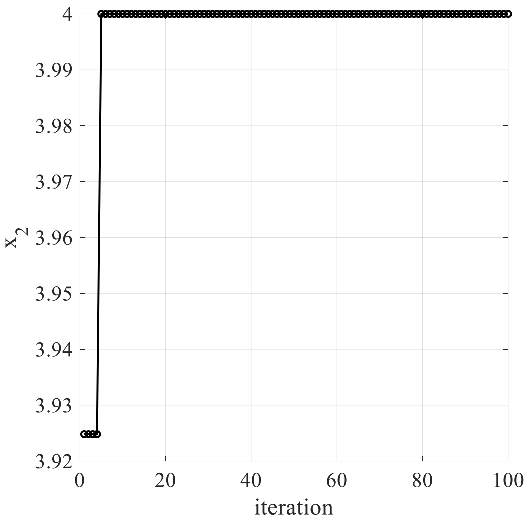

(c)

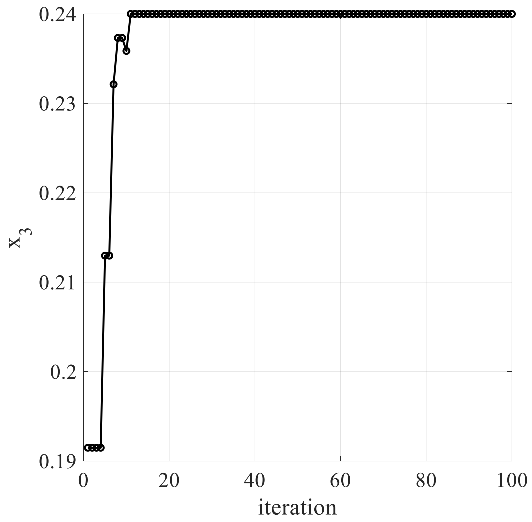

(d)

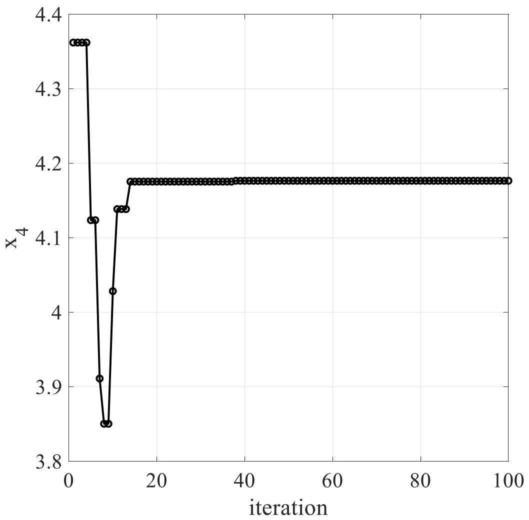

(e)

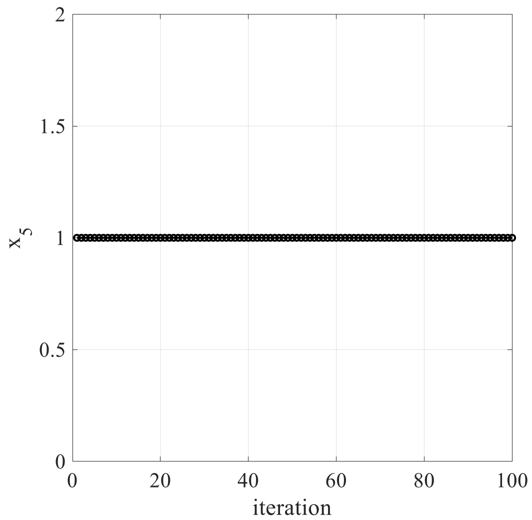

(f)

Figure 4.19 – Optimization converge results for the case II (Tsai-Wu): objective function (a) and design variables (b)-(f).

The results obtained by mono-objective and multiobjective optimization demonstrated that the best ply drop-off location is the dropped plies 4 and 5 together with a hybrid tube. As can be observed in Table 4.13 and Table 4.14, this setup has generated higher buckling load and a lower failure index.

As can be seen in Figure 4.15, the ply position (x_2 and x_4) and hybrid (x_5) variables are inversely proportional, being considered conflicting variables that can be well represented by the Pareto front, as depicted in Figure 4.20.

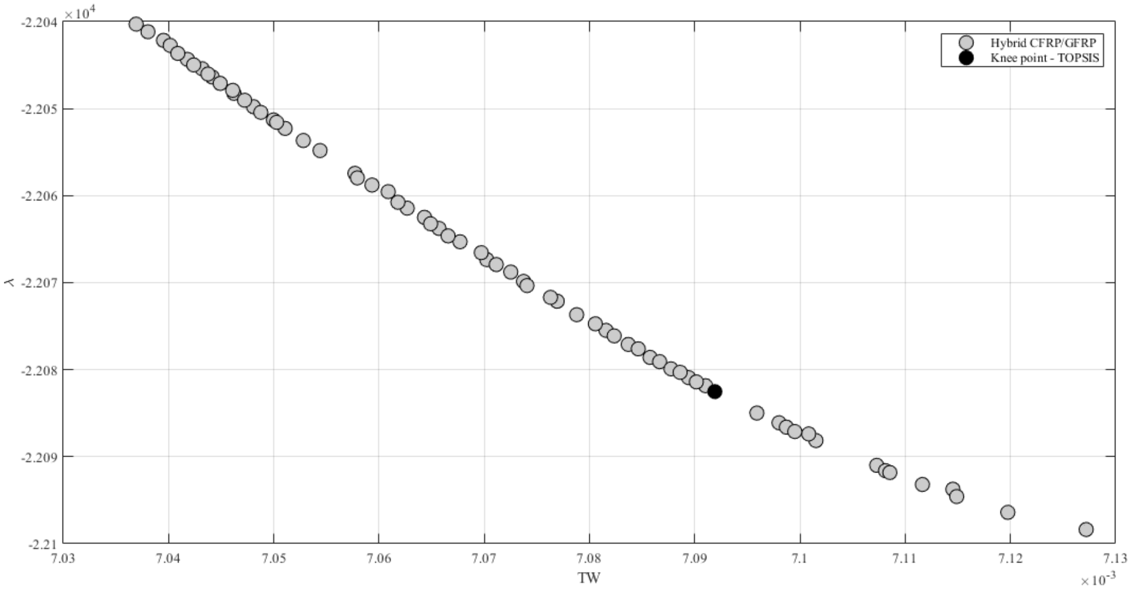

Figure 4.20 – Optimal solution found using Pareto front for the ply drop-off location considering the failure index and buckling load responses.

According to Figure 4.20, it could be concluded that the optimal point is close due to the physical characteristics of the presented problem, as only a small range could be obtained from the combination of five design variables, contributing to this phenomenon.

To further analysis, the Pareto front determines a set of feasible points that, in this case, are represented by the CFRP/GFRP hybrid tube. The optimal solution can be found at the knee point due to convexity, as can be seen in Figure 4.20. While the points located at the ends of the curve correspond to the points known as Nadir, they also symbolize optimal parameters considering the mono-optimization (MESSAC and MATTSON, 2004). The Nadir 1 point represents the optimal result aimed at minimizing TW, while the Nadir 2 point represents maximizing buckling loading. The knee and Nadir points are depicted in Table 4.15, representing the multiobjective optimization.

Table 4.15 – Multiobjective optimization considering Pareto front considering the better structural responses.

Point	x_1	x_2	x_3	x_4	x_5	**Structural Response**
Nadir 1	0.1159	4	0.2399	4	Yes	TW_c=0.0070 λ = -22.0430kN
Nadir 2	0.1018	4	0.2397	4	Yes	TW_c=0.0071 λ= -22.0984kN
Knee	0.1085	4	0.2398	4.23	Yes	TW_c=0.0071 λ=-22.0750kN

For the Nadir and Knee points, the best results were considered a hybrid tube, as depicted in Table 4.15. Another important fact is that it was the 5 dropped ply on the second panel due to the 4 ply having already been dropped in x_1. According to panel position, the first ply drop-off located at the beginning of the tube and the second ply drop-off at the end provide better results related to buckling load and failure index, as can be seen in Tables 4.13 to 4.15.

To conclude, for buckling load and *FI*, the ply drop-offs located nearest to the ends of the tube in opposite directions are the most convenient. Ply drop-offs located in the middle of the tube generate a reduction in the buckling load. Figure 4.21 shows in detail the optimal panel position for the ply drop-off in the tubular structure.

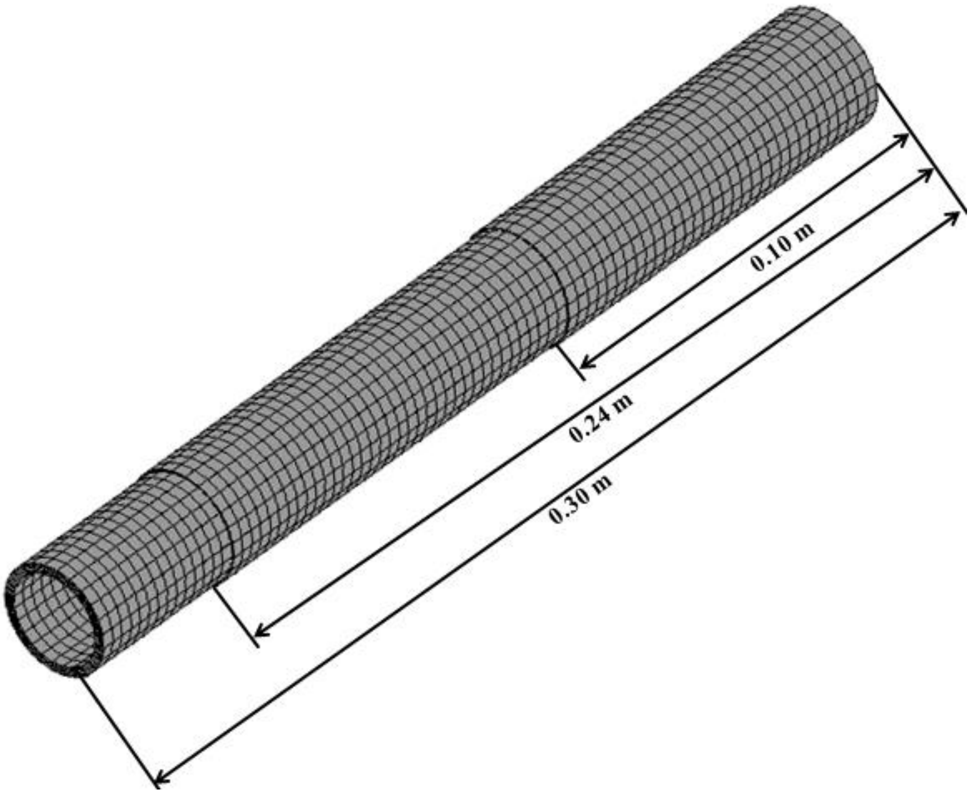

Figure 4.21 – Optimal tubular structure with a total length of 0.3 m considering the fourth ply dropped at 0.1 m and the fifth ply at 0.24m, respectively.

4.3 On the Influence of manufacturing Parameters on Buckling and Modal Properties of Sandwich Composite Structures

To simplify the text, abbreviations were adopted for each type of honeycomb structure, i.e., honeycomb sandwich structure with carbon face and aramid core (CAC), carbon face and PP core (CP), glass face and aramid core (GA), glass face and PP core (GP), carbon and aramid hybrid face and aramid core (HCA), carbon and aramid hybrid face and PP core (HCP), glass and aramid hybrid face and aramid core (HGA) and glass and aramid hybrid face and PP core (HGP). Index 1 was used for the first replicate, and index 2 was used for the second.

4.3.1 Modal behavior of sandwich structures with different cores and face sheets

Based on the experimental tests, the first three natural frequencies of the honeycomb sandwich specimens with different materials in the face and core have been obtained, as can be seen in Figure 4.22.

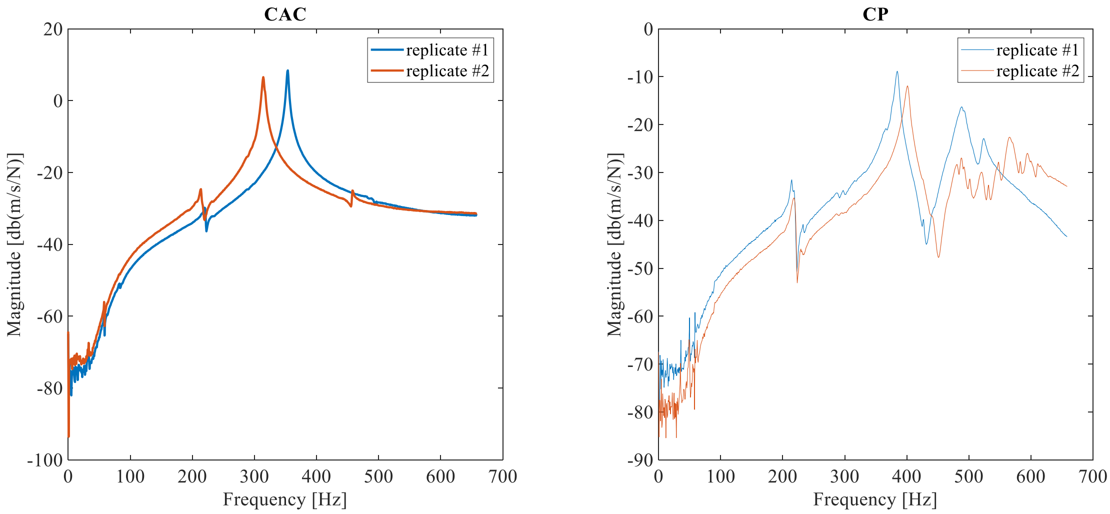

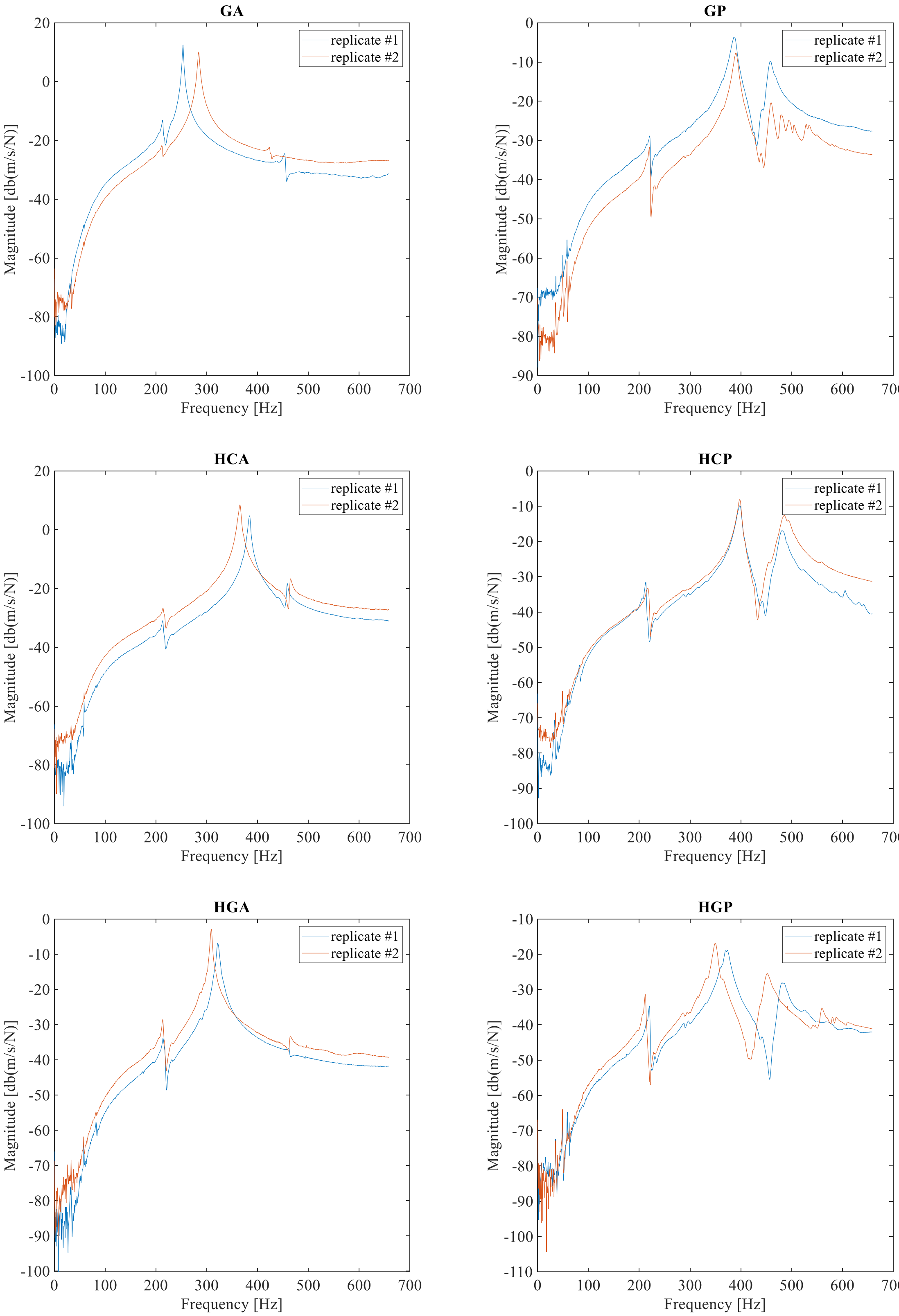

Figure 4.22 – Frequency response functions of sandwich specimens with different cores and face sheets with length of 125 mm and width of 46 mm considering two replicates.

It is possible to assert that the natural frequency has a direct connection with the stiffness and structural mass. The results for the frequency response functions (FRFs) considering each specimen and their replicates showed good agreement. The discrepancy between the results of replicates 1 and 2, for all cases, showed minor differences of less than 5%. The first natural frequency for all specimens presented little variation between 210 Hz and 220 Hz. Higher natural frequencies were found for honeycomb sandwich specimens manufactured with glass faces, with carbon and aramid hybrid faces, and with carbon faces, both manufactured with PP cores. While lower values were found for GA, HCA, and HGA, these specimens were manufactured with an aramid core, which is lighter and thinner than the PP core. According to Abbadi *et al.* (2009), the PP core is denser than the aramid core, promoting high stiffness in the sandwich structures with this type of core.

4.3.2 Bending behavior of sandwich structures with different cores and face sheets

To understand the effects of bending strength on the eight different honeycomb sandwich specimens (CAC, CP, GA, GP, HCA, HCP, HGA, and HGP) and their replicates, load versus displacement curves were plotted in Figure 4.23. One can see that the load versus displacement curves demonstrated fairly similar patterns between the two replicates for each combination, despite different levels. The bending load increased when the glass and aramid hybrid fabric were used on the beam faces. Considering the fabrics used in these experimental tests, the glass and aramid hybrid fabric is the strongest. However, it is the heaviest, thickest, and most expensive. The lower loads were obtained for specimens manufactured with aramid cores. One reason for this can be reductions in specimen thickness when aramid cores are used. GA specimens showed slight decreases in maximum loading and were demonstrated to be the weakest when compared to the other specimens. The results of the bending tests for the GP specimens were very similar to those found by Arbaoui *et al.* (2018).

Sun *et al.* (2017) divided the load versus displacement curve in a bending test into two stages, considering load peak. In stage 1 (point zero to point A), the pre-buckling occurs according to the crosshead as it moves downward. The increased load causes structural instability. As shown in Figure 4.23, the load is stable in stage 2 (point B to the end), also known as the post-buckling stage. Linear-elastic behavior for the sandwich structures was observed at the initial stages (from point zero to point A). Structure stiffness is reduced at point A towards point B, where failures occur. Collapse and sheet fractures were observed at point A towards point B, where loading was decreasing or recovering. The HGA and HGP specimens showed different behavior. An abrupt decrease in loading was seen after peak load (point B). The load rose again to reach the second peak, repeating this sequence until it arrived at the end of the curve. This was probably caused by the load reaching the bottom beam face (HAN *et al.* 2020). The HGA specimens showed greater ranges between the initial and pre-buckling stages, generating a longer lasting linear-elastic behavior. The loading remained more stable in the post-buckling stage for the HGA, HGP, and CA specimens, promoting large displacements. As shown in Figure 4.23, the GP and HGP specimens with small displacements showed reductions in structural stiffness. However, the HGP specimens supported much higher loads than GP specimens. The use of the PP core provided a considerable increase in the maximum bending load in all specimens, as can be observed in Figure 4.23. This fact can be justified by the cell size and mechanical properties of the material.

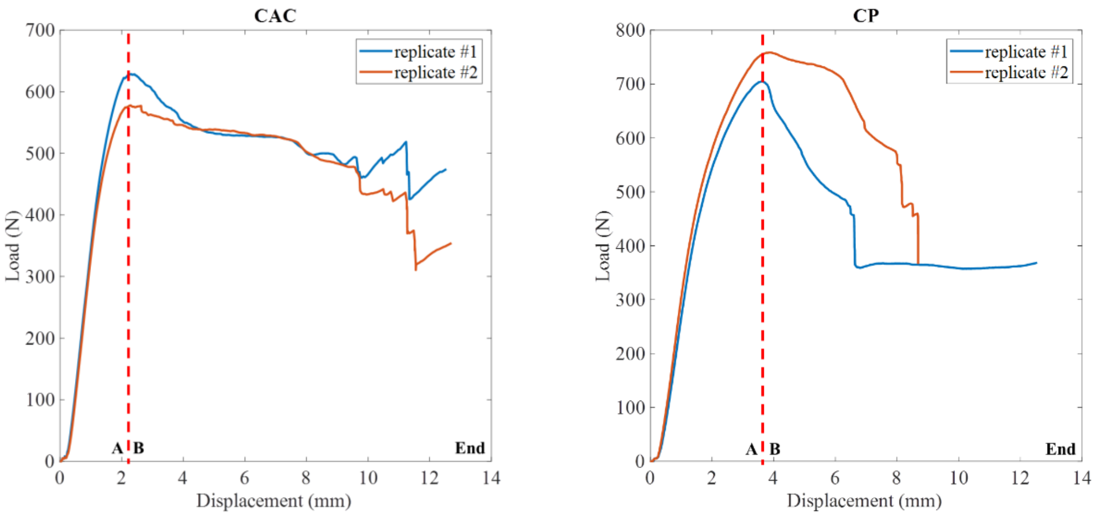

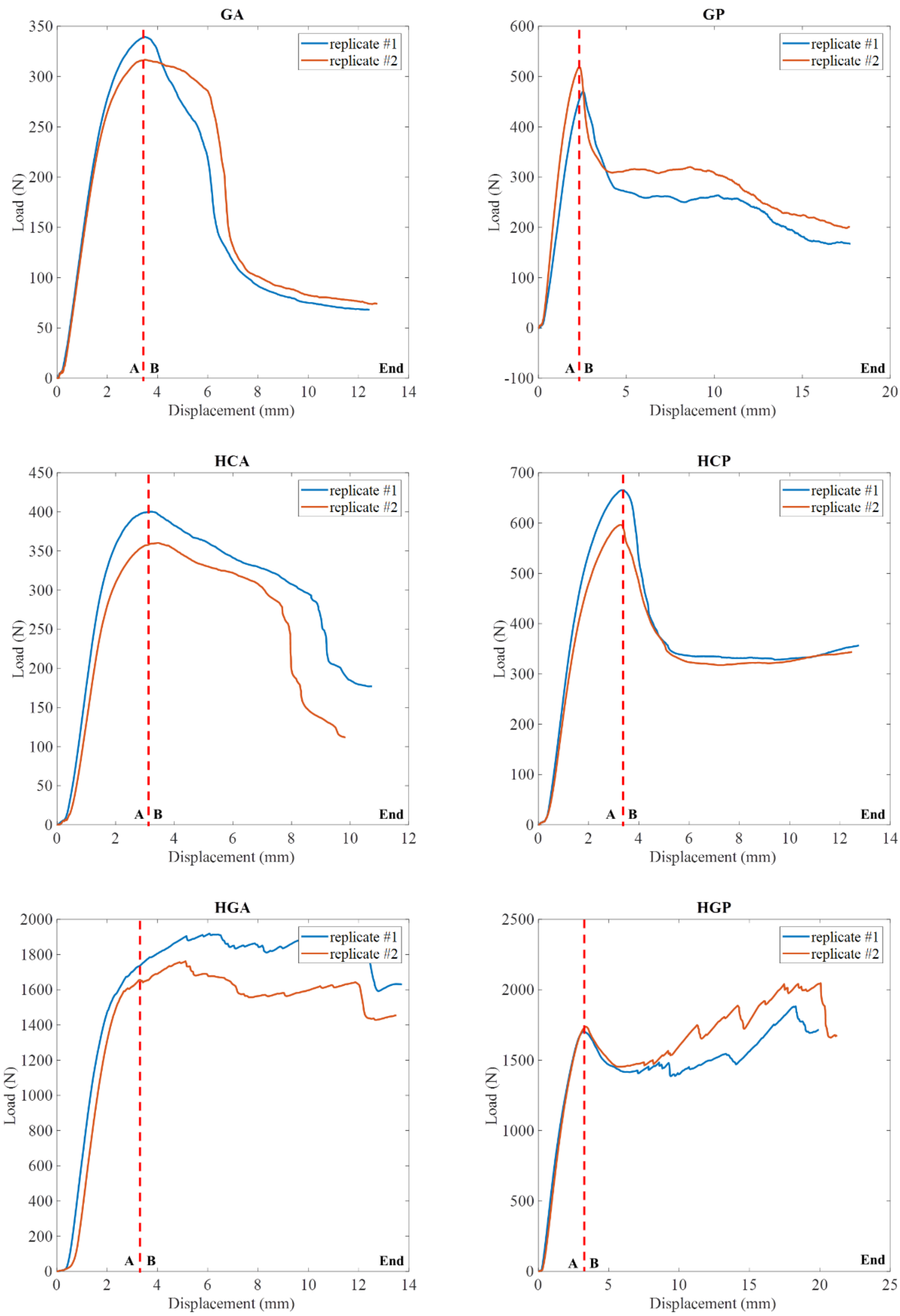

Figure 4.23 – Load versus displacement curves of honeycomb sandwich specimens with different cores and face sheets with length of 125 mm and width of 46 mm considering two replicates obtained with the three-point bending test (--- replicate 1, --- replicate 2).

Some sandwich specimens tended to deform in a “V” shape (mode A), like GP and GA specimens, while other specimens deformed in a “semi-circle” shape (mode B), given the geometry of the loading pin, as shown in Figure 4.24. The specimens that showed a failure mode in a “V” shape had thinner faces. As the thickness was increased, the shape failure mode changed to a “semi-circle”. Sun *et al.* (2017) affirm that face thickness and cell size length can be important parameters for determining the “V” shape failure mode for sandwich structures subjected to three-point bending tests. In this study, we verified that thinner-faced specimens tended to fail in mode A, regardless of core cell size. It is worth noting that PP thermoplastic cores showed notable shape-recovery effects compared to other materials, like metals, given their elasticity-plasticity properties (GAO *et al.* 2020).

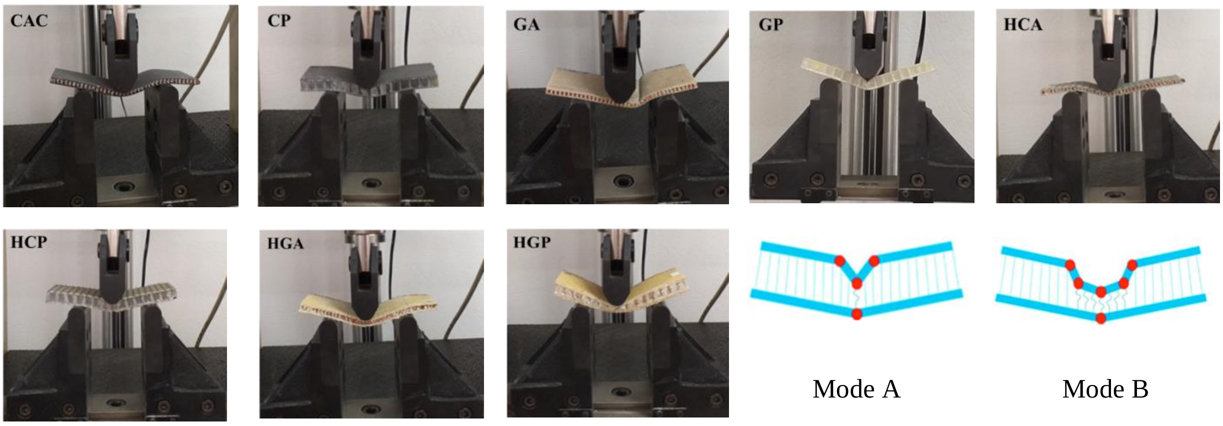

Figure 4.24 – Comparison of the deformation schematic considering the deformation modes A and B for different honeycomb sandwich specimens in the three-point bending test (adapted from SUN *et al.* 2017).

It is worth noting that no honeycomb sandwich structure presented delamination on either the upper or bottom faces. Dutra *et al.* (2019) reported that the honeycombs manufactured with diagonal cell walls are responsible for a more uniform stress distribution at the interface, providing an effective at the bonding interface.

The deformation modes are associated with failure modes like indentation, face buckling, core buckling, wrinkling of the face layer, and core crushing. The HGP specimens showed core crushing, while specimens with carbon or carbon and aramid hybrid fabric faces suffered less wrinkling than glass and glass/aramid faces, as shown in Figure 4.25.

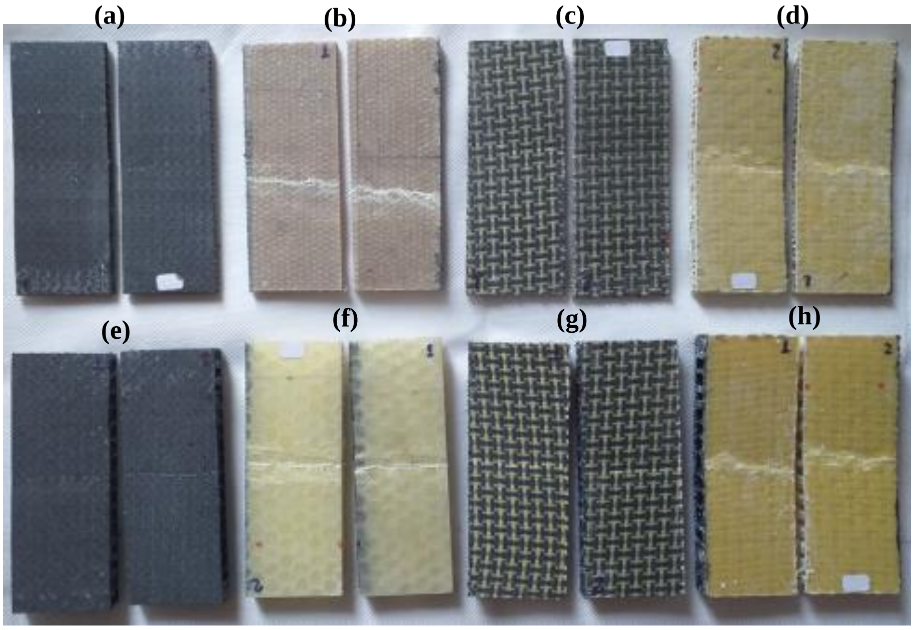

Figure 4.25 – Honeycomb sandwich specimens after the three-point bending test for the specimens: (a) CAC, (b) GA, (c) HCA, (d) HGA, (e) CP, (f) GP, (g) HCP and (h) HGP.

The facing stress was significantly affected by the thickness of the specimens. Thicker specimens had lower facing stress, like HGP at 14 MPa, which can be attributed to the face thickness and stress factors, which are inversely proportional, as shown by Equation 3.2. The highest final core shear strength was for carbon fiber applied to the sandwich faces, where the average final core shear strength was 41 MPa and 39 MPa for CAC and HCA specimens, and 20 MPa and 23 MPa for CP and HCP specimens, respectively. The lowest final core shear strength values were for HGP, at 14 MPa. When the PP core was replaced by an aramid core, this led to increased final core shear strength for the HGA specimens (37 MPa), consequently affecting the flexural strength of the honeycomb sandwich specimens. Indeed, the change in core material provided increased strength for all sandwich specimens, as can be confirmed in Section 4.3.4 in Table 4.17.

4.3.3 Buckling behavior of sandwich structures with different cores and face sheets

Buckling is a common failure mode, occurring when applied loads reach the top of the curve and then the load drops gradually. First, buckling occurs, and then failure modes are analyzed. As shown in Figure 4.26, honeycomb sandwich specimens presented greater strength in buckling than in bending. Buckling was not clearly visible along the whole curve in some cases, like HCA_1, HCP_1, and HCP_2, and the peak load drop was small and almost imperceptible. Furthermore, for these specimens, increased load was restored, and then new peaks arose, as can be observed in Figure 4.26.

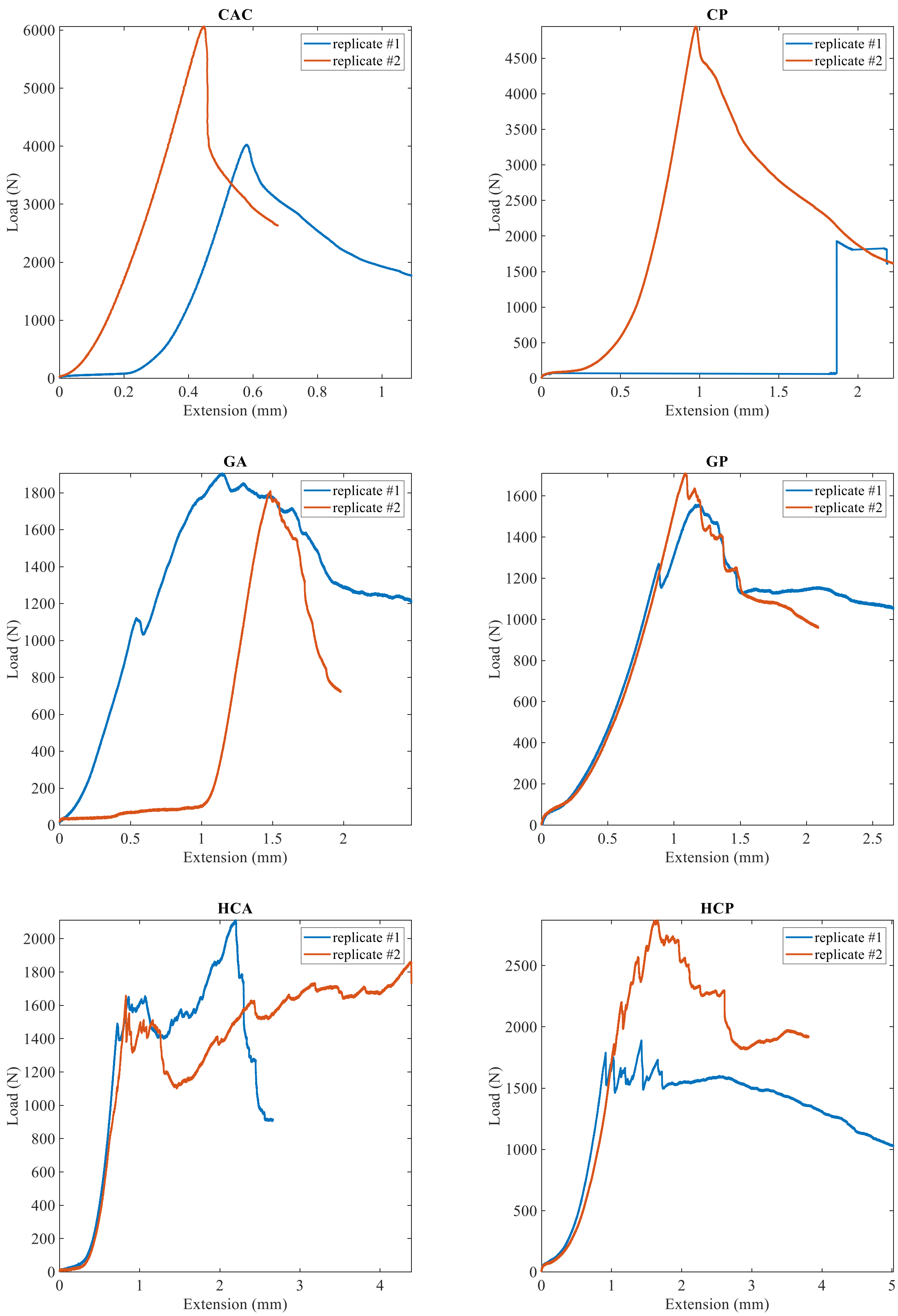

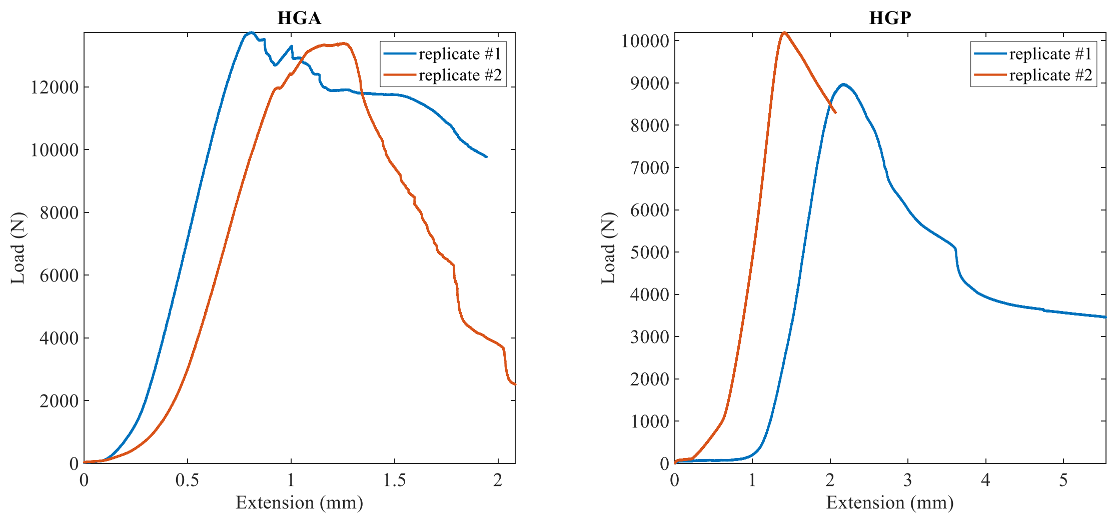

Figure 4.26 – Load versus extension curves of honeycomb sandwich specimens with different combinations of cores and face sheets considering two replicates obtained in the buckling test.

The lowest loadings were observed for GA and GP specimens, with average loads of 1.46 kN and 1.48 kN, with corresponding displacements of 1.02 mm and 0.99 mm, respectively. We observed that both specimens manufactured with glass fabric faces with thinner faced-sheets supported lower loads as per the bending tests. Eyvazian *et al.* (2019) reported that increased face sheet thickness causes increases in buckling loads. Additionally, it is worth noting that buckling is smoother in specimens with thinner faced-sheets, like glass-faced sheet. Sun *et al.* (2017) concluded that face thickness has a significant influence on the development of the load versus extension curves and collapse modes.

The highest loads before buckling were for HGA and HGP specimens, with average ranges of between 12.75 kN and 9.53 kN, respectively. Both specimens were manufactured with glass and aramid hybrid fabric on the face sheets, which is the thicker fabric. The CAC and CP specimens manufactured with carbon fiber endured higher loadings compared to HCA and HCP in the bending and buckling conditions. Although carbon fiber is stronger, it is more expensive.

For CAC, CP, HCA, and HCP, the load reached average peaks of 5.04 kN, 4.94 kN, 1.54 kN, and 1.77 kN, respectively. The maximum buckling load for CP_1 was reduced compared to CP_2. The possible reason for this influence could be some noise in the experimental test, resulting in a divergence between the curves, whereas both specimens were manufactured using the same experimental conditions.

According to ASTM C364/C364M-16, the failure modes available for the buckling test are face sheet buckling, face sheet compression, face sheet dimpling, core compression, and core shear, as shown in Figure 4.27.

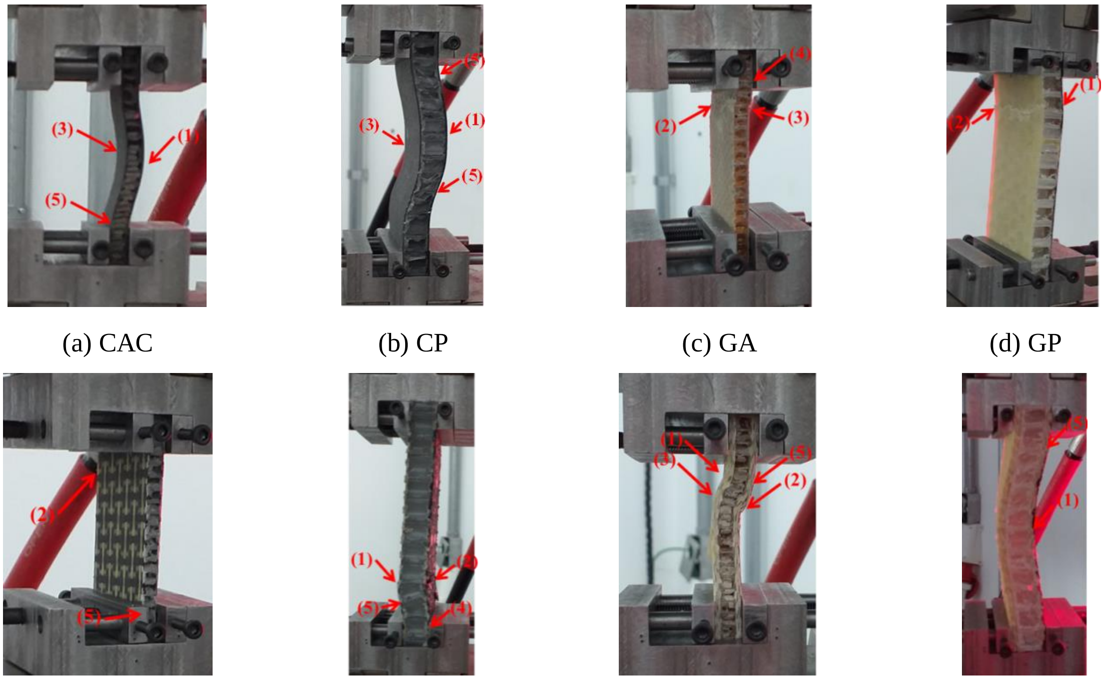

(a) CAC (b) CP (c) GA (d) GP

(e) HCA (f) HGP (g) HGA (h) HGP

Figure 4.27 – Typical failure modes occurred in the honeycomb sandwich specimens during buckling test: (1) face sheet buckling, (2) face sheet compression, (3) face sheet dimpling, (4) core compression, and (5) core shear.

The boundary conditions also affect failure modes, and laterally clamping the specimens prevents extremity crushing failures, which is the most common failure mode causing structural instability. As seen in Figure 4.27, buckling was more evident for CAC, CP, GP, HGA, and HGP. The failure modes for the specimens manufactured with carbon face sheets were similar since all specimens showed face sheet buckling, face sheet dimpling, and core shear. The failure modes for HCA and HCP were less significant, and failures were more visible in specimens with PP cores. The specimens with glass face sheets supported a lower loading, presenting cracks in the extremity close to clamping pins, as can be seen in the GA and GP specimens, where cracks were found in the upper region. It is important to note that, similar to the bending test, no delamination occurred in the buckling test.

It can be stated that CAC and HGA specimens suffered from face sheet dimpling, which may have been caused at the beginning of the tension in this region. The specimens with cracks in their face sheets also suffered tension or compression depending on the slope caused by the crack on the specimen. For HCA and GP, the cracks caused compression in the upper region. For the HCP specimen, compression was seen at the bottom region, as shown in Figure 4.27.

4.3.4 Full general factorial design for different honeycomb sandwich structures

The statistical study seeks to characterize the properties of different honeycomb structures when submitted to distinct loading conditions. Furthermore, the full general factorial designs allowed for the creation of combinations for manufacturing honeycomb sandwich specimens. The full general factorial design considering the response variables obtained by the buckling test is shown in Table 4.16, while the full general factorial for the modal and bending tests is shown in Table 4.17.

Table 4.16 – Full general factorial design with two design variables and four response variables derived from buckling test.

	Design variables		**Experimental responses**			
Exp.	**Type of face sheet**	**Type of core**	***Mass [g]***	***P_{max} [N]***	***δ_{max} [mm]***	***σ_{max} [MPa]***
1	Carbon	Aramid	5.59	4022.87	0.58	19.20
2	Carbon	PP	15.46	4930.89	0.18	9.43
3	Glass	Aramid	4.03	1110.25	0.55	5.69
4	Glass	PP	12.74	1264.34	0.89	2.59
5	Carbon/aramid	Aramid	3.62	1489.94	0.72	7.51
6	Carbon/aramid	PP	12.21	1761.31	0.91	3.58
7	Glass/aramid	Aramid	14.68	13688.76	0.79	46.93
8	Glass/aramid	PP	39.64	8913.12	2.12	13.26
9	Carbon	Aramid	5.92	6059.12	0.45	28.58
10	Carbon	PP	15.78	4939.36	0.98	9.45
11	Glass	Aramid	4.51	1806.83	1.49	9.33
12	Glass	PP	12.55	1704.76	1.09	3.41
13	Carbon/aramid	Aramid	3.79	1581.31	0.82	8.17
14	Carbon/aramid	PP	12.37	1788.71	1.02	3.60
15	Glass/aramid	Aramid	14.46	11818.07	0.91	41.24
16	Glass/aramid	PP	38.88	10146.70	1.38	14.82

Table 4.17 – Full general factorial design with two design variables and ten response variables derived from modal and bending tests.

Exp.	**Design variables**		**Experimental responses**									
	Type of face sheet	**Type of core**	ω_1 ***[Hz]***	ω_2 ***[Hz]***	ω_3 ***[Hz]***	***Mass [g]***	η ***[%]***	***Cost[$]***	F_{max} ***[N]***	δ_{max} ***[mm]***	F_{ult} ***[MPa]***	σ_{fac} ***[MPa]***
1	Carbon	Aramid	219.7	353.8	458.5	14.16	0.7458	12.96	628.76	2.23	1.48	42.53
2	Carbon	PP	213.9	384.5	486.3	18.00	1.3502	12.06	704.81	3.62	0.72	21.65
3	Glass	Aramid	213.1	253.4	453.4	9.25	0.8023	5.76	339.35	3.49	0.84	36.18
4	Glass	PP	220.5	387.5	457.8	15.05	1.8731	4.86	470.57	2.54	0.49	18.19
5	Carbon/aramid	Aramid	213.1	384.5	458.5	9.00	0.9897	11.02	400.26	3.20	0.99	43.26
6	Carbon/aramid	PP	213.1	397.7	480.5	15.25	1.3944	10.12	665.65	3.33	0.69	24.12
7	Glass/aramid	Aramid	213.9	321.5	461.4	37.04	1.4281	14.75	1932.91	10.78	3.74	40.38
8	Glass/aramid	PP	219.7	375.0	481.2	45.52	2.2369	15.29	1881.57	18.28	1.70	14.91
9	Carbon	Aramid	213.2	314.2	458.5	14.08	1.0974	12.96	577.77	2.28	1.37	39.82
10	Carbon	PP	216.8	399.2	479.0	19.41	1.3683	12.06	758.58	3.86	0.77	19.27
11	Glass	Aramid	210.2	284.2	423.3	9.13	1.072	5.76	316.55	3.47	0.78	33.00
12	Glass	PP	219.7	389.6	460.0	15.89	1.5395	4.86	517.9	2.34	0.54	21.97
13	Carbon/aramid	Aramid	213.9	366.2	465.1	8.91	1.1116	11.02	360.23	3.42	0.88	35.07
14	Carbon/aramid	PP	215.3	397.7	485.6	15.16	1.4645	10.12	596.39	3.27	0.62	22.80
15	Glass/aramid	Aramid	213.1	309.1	465.8	35.01	1.3446	14.75	1762.19	5.12	3.38	35.26
16	Glass/aramid	PP	211.7	349.4	452.6	45.44	2.0017	15.29	2046.55	20.06	1.80	13.21

The quality of fit was measured by ANOVA using the R^2_{adj} indicator, considering the results obtained by the modal, bending, and buckling tests, are shown in Table 4.18.

Table 4.18 – R^2_{adj} indicator obtained from ANOVA considering different honeycomb sandwich structures for the modal and bending test results.

Responses	R^2_{adj}
ω_1 [Hz]	21.49%
ω_2 [Hz]	88.02%
ω_3 [Hz]	53.98%
mass [g]	99.74%
η [%]	85.56%
Cost[$]	100.00%
F_{max} [N]	98.89%
$\delta_{max}[mm]_{(Bending)}$	93.04%
$F_{ult(core\ shear)}[MPa]$	98.82%
$\sigma_{(facing)}[MPa]$	92.08%
P_{max} [N]	35.09%
$\delta_{max}[mm]_{(buckling)}$	99.94%
$mass\ [g]_{(Buckling)}$	96.45%
σ_{max} [MPa]	95.30%

The first and third natural frequencies showed a lack of fit to the model, generating a poor quality of fit, as can be seen from the R^2_{adj} indicator below 80%. The remaining of the response variables demonstrated is appropriate for the model using two design variables. Therefore, it is clear that the type of face sheet and the type of core both exert great influence on the second natural frequency, the structural mass, the modal damping factor, the material costs, and the maximum bending load, the final core shear strength, and the facing stress. The design created from the buckling test results shows that the structural mass, the maximum displacement, and the maximum buckling load response variables are significant for this model.

Pareto charts were drawn to determine the effect of each design variable, their interaction, and the parameters that contributed to response variability. As shown in Figure 4.28, the dashed red line denotes the relevance of the effects.

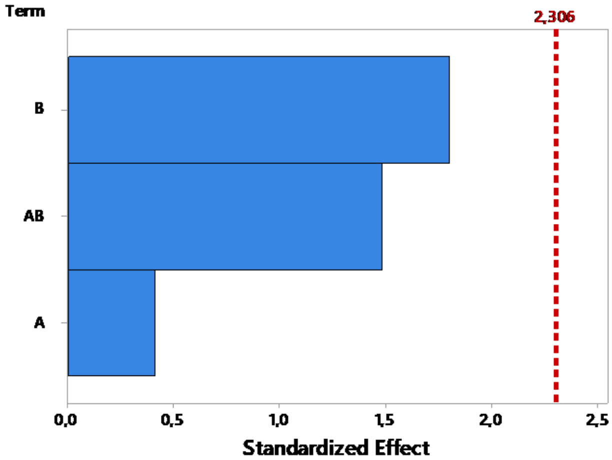
Term
2,306
B
AB
A
0,0
0,5
1,0
1,5
2,0
2,5
Standardized Effect
(a)

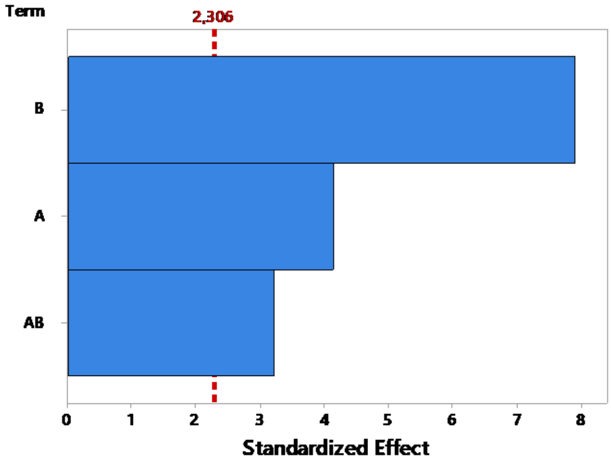
Term
2,306
B
A
AB
0
1
2
3
4
5
6
7
8
Standardized Effect
(b)

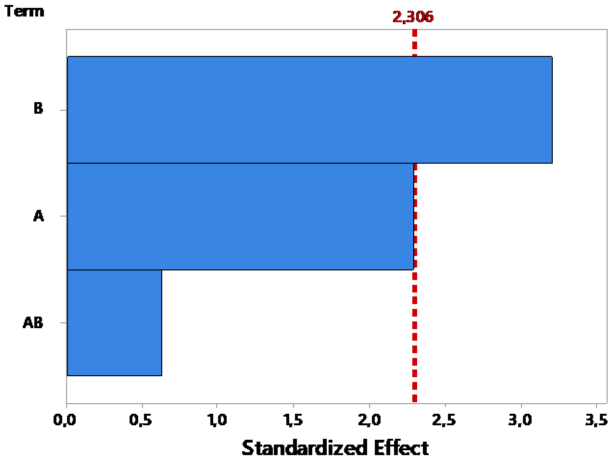
Term
2,306
B
A
AB
0,0
0,5
1,0
1,5
2,0
2,5
3,0
3,5
Standardized Effect
(c)

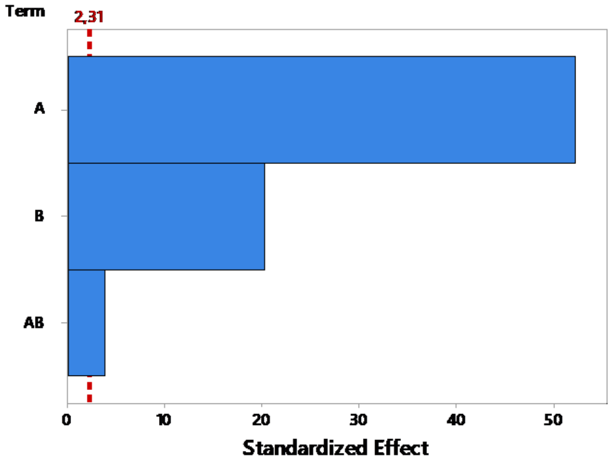
Term
2,31
A
B
AB
0
10
20
30
40
50
Standardized Effect
(d)

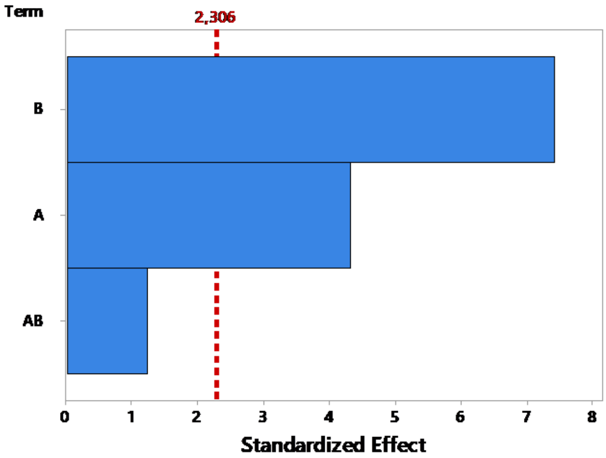
Term
2,306
B
A
AB
0
1
2
3
4
5
6
7
8
Standardized Effect
(e)

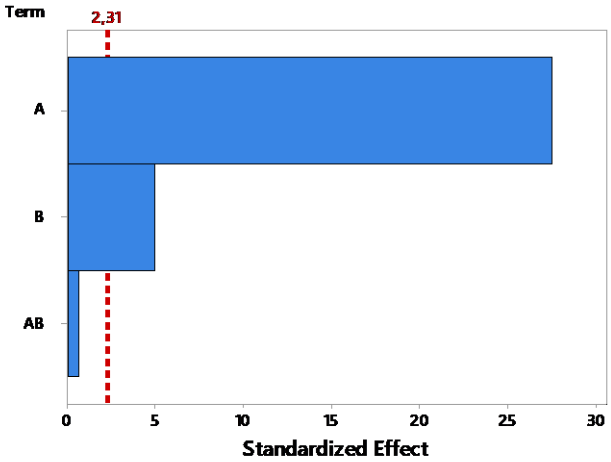
Term
2,31
A
B
AB
0
5
10
15
20
25
30
Standardized Effect
(f)

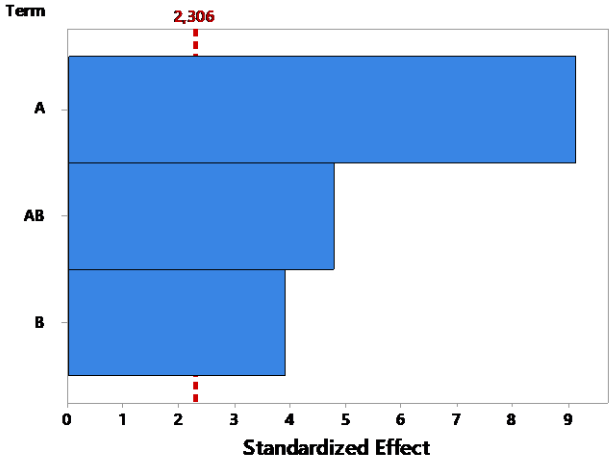
Term
2,306
A
AB
B
0 1 2 3 4 5 6 7 8 9
Standardized Effect

(g)

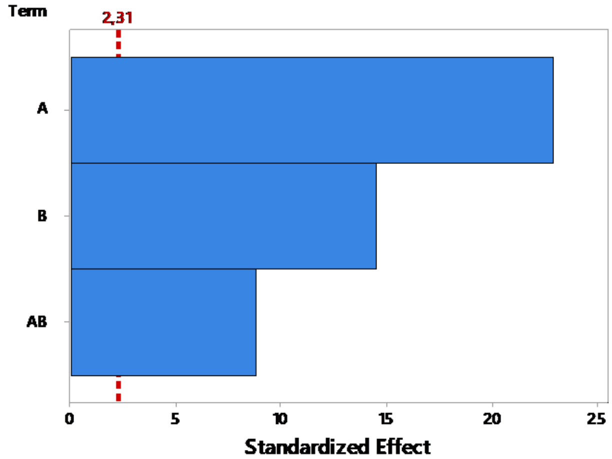
Term
2,31
A
B
AB
0 5 10 15 20 25
Standardized Effect

(h)

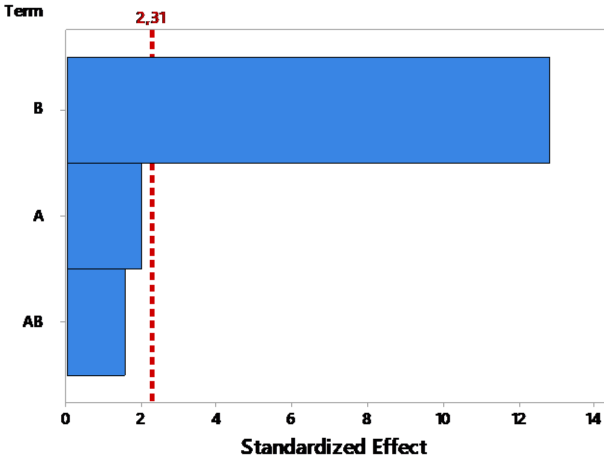
Term
2,31
B
A
AB
0 2 4 6 8 10 12 14
Standardized Effect

(i)

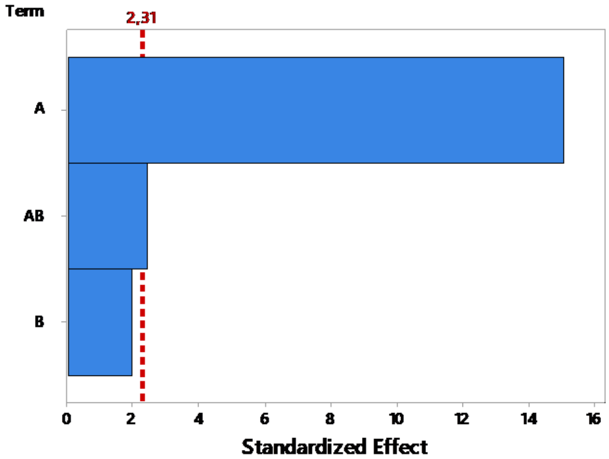
Term
2,31
A
AB
B
0 2 4 6 8 10 12 14 16
Standardized Effect

(j)

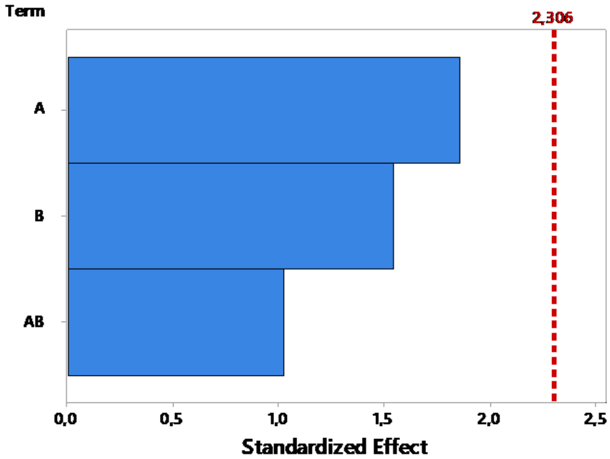
Term
2,306
A
B
AB
0,0 0,5 1,0 1,5 2,0 2,5
Standardized Effect

(k)

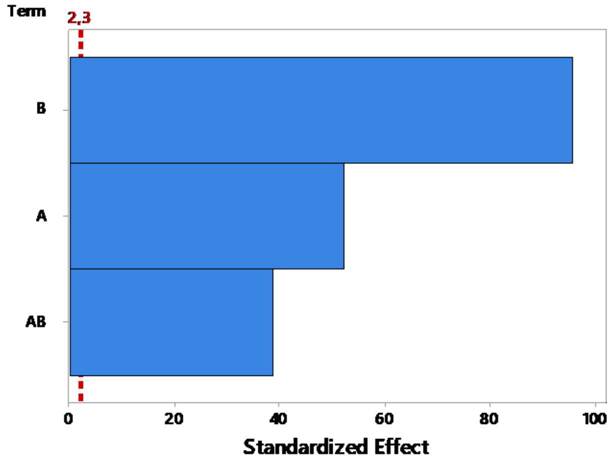
Term
2,3
B
A
AB
0 20 40 60 80 100
Standardized Effect

(l)

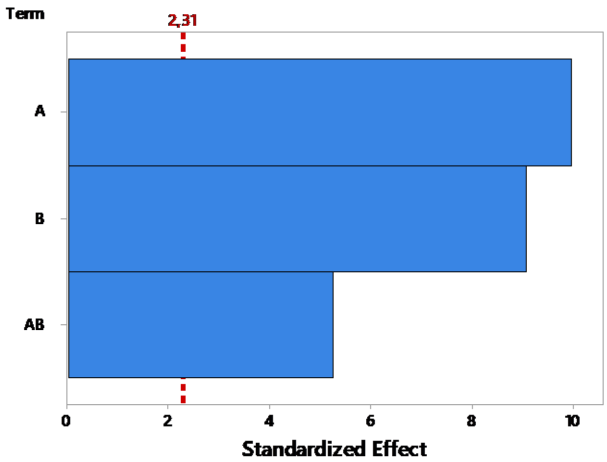

(m)

Figure 4.28 – Pareto charts for (a) ω_1, (b) ω_2, (c) ω_3, (d) mass, (e) η, (f) F_{max}, (g) $\delta_{max\ (Bending)}$, (h) $F_{ult(core\ shear)}$, (i) $\sigma_{(facing)}$, (j) P_{max}, (k) $\delta_{max\ (Buckling)}$, (l) mass, and (m) σ_{max} response variables obtained in the modal, bending and buckling tests (legend factor A = type of face sheet and factor B = type of core).

The cost response variable is not shown in the Pareto chart because the standard error for the effects is inexistent. However, this was an isolated fact that can be explained by the cost design variable of each combination being the same for the replicate 1 and replicate 2 because they are manufactured with the same type of core and face sheet. The cost response variable has been interesting in the manufacturing scope. The HGA and HGP specimens were more expensive, costing around R$15.00. However, these specimens were stronger in bending and presented a higher damping factor. While the GA and GP specimens were cheaper, each costing around R$5.00, they demonstrated support for lower bending and bucking loadings.

The Pareto charts show that the type of face sheet and type of core design were not significant for the first natural frequency and the maximum displacement in the buckling response variables, as shown in Figure 4.28a and Figure 4.28k. We can see that the third natural frequency and facing stress response variables only depend on the core design factor, as shown in Figure 4.28c and Figure 4.28i. The remaining response variables have similar relationships with the design variables and/or their interactions.

Therefore, it is correct to affirm that the core design variable contributed more to response variability than anything else. In general, it should be noted that the PP honeycomb core provided higher structural stiffness, the thicker specimens had lower facing stress, the carbon fabric offered higher final core shear strength, the lower buckling loads were obtained using glass fabric on the face sheets, and the glass and aramid hybrid fabric generated higher loadings in bending and buckling conditions. Despite glass and aramid hybrid fabric having high strength, it was not selected to manufacture the tubular structures due to their high cost, thicker and difficult-to-handle nature.

4.4 The Influence of the Type of Fabric on the Static and Dynamic Behavior of Composite Tubes with Ply Drop-offs

The experimental tests were performed considering tubular structures with ply drop-offs located in specific regions determined by the metamodel created for ply drop-off location optimization. As can be seen in Figure 4.29, all the tubular structures had their thickness reduced due to the tapering of the four plies.

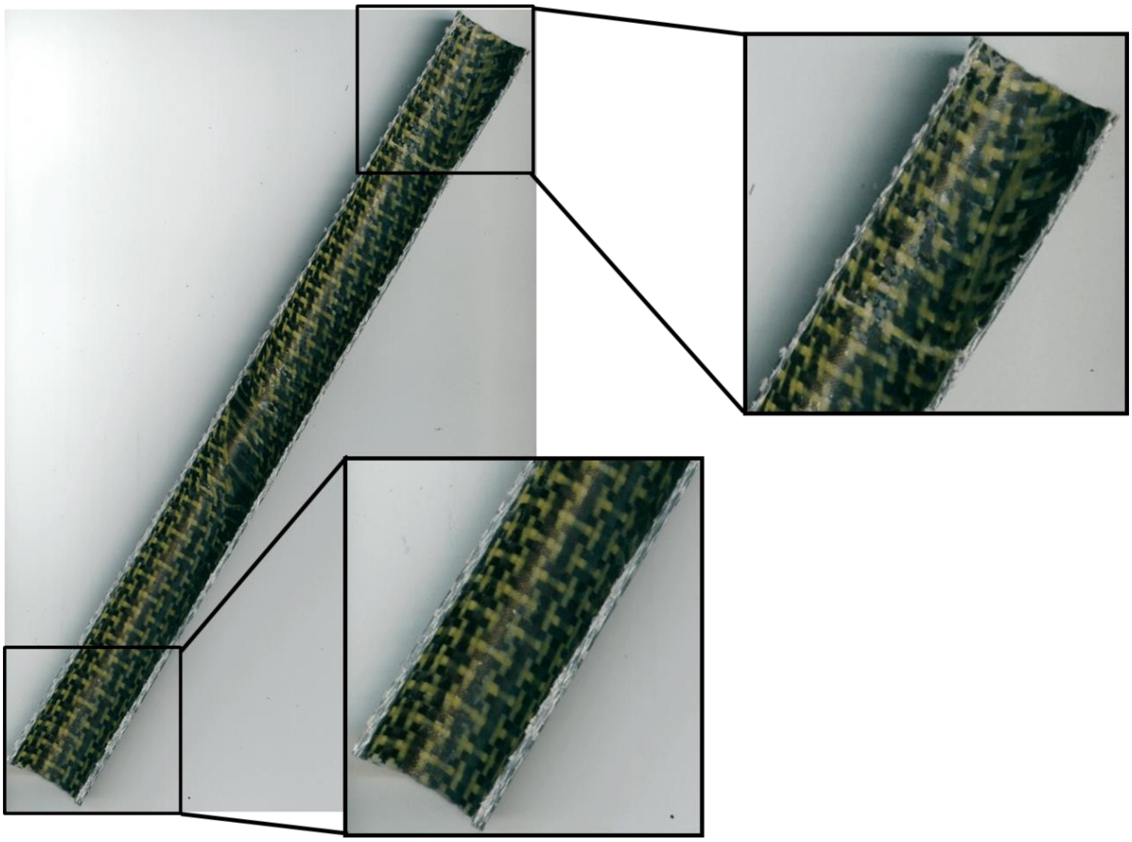

Figure 4.29 – Evident change in the thickness due to the use of ply drop-offs in a tube manufactured with carbon and aramid hybrid fabric.

Then, new experimental tests were performed considering non-tapered tubular structures. With knowledge about the structural behavior of non-tapered tubular structures, it is possible to determine the advantages of the use of ply drop-offs in different tubular structures.

4.4.1 Compression experimental test in hybrid and non-hybrid tubes

The compressive load-extension curve measured for all tubes with ply drop-offs is shown in Figures 4.30 to 4.34. As the failure in the CA tapered tube not evident, the crack phenomenon was not shown in Figure 4.31.

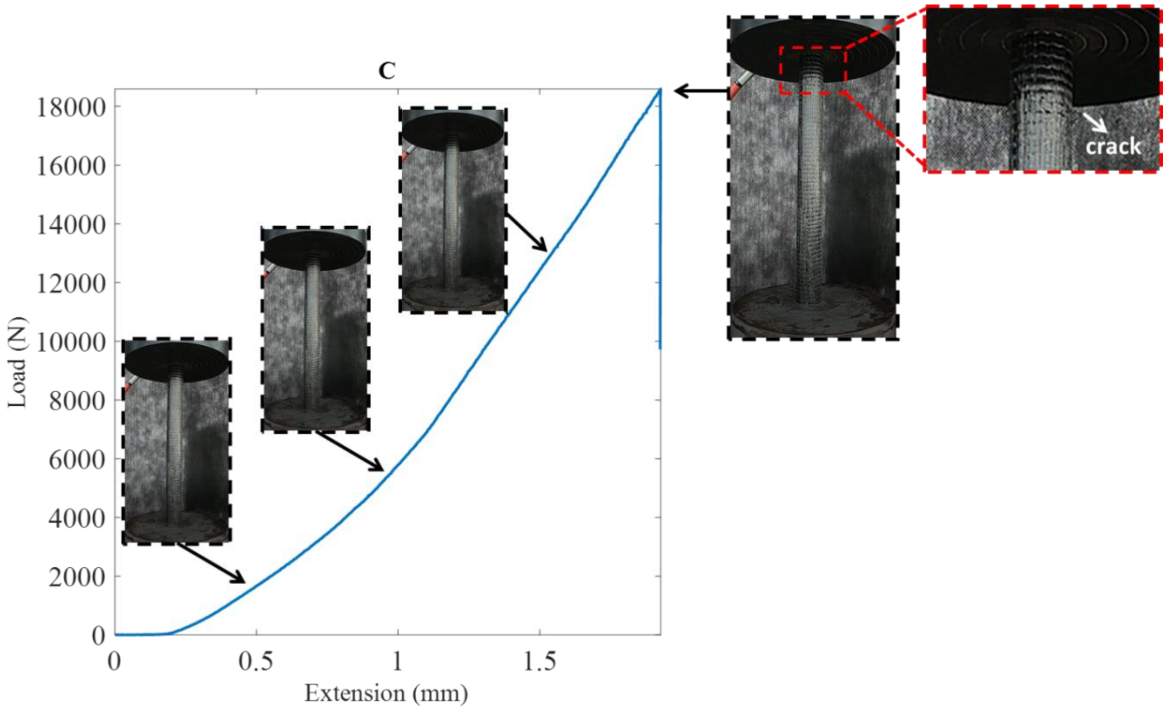

Figure 4.30 – Compressive load-extension curves for C tube with ply drop-offs in compression test.

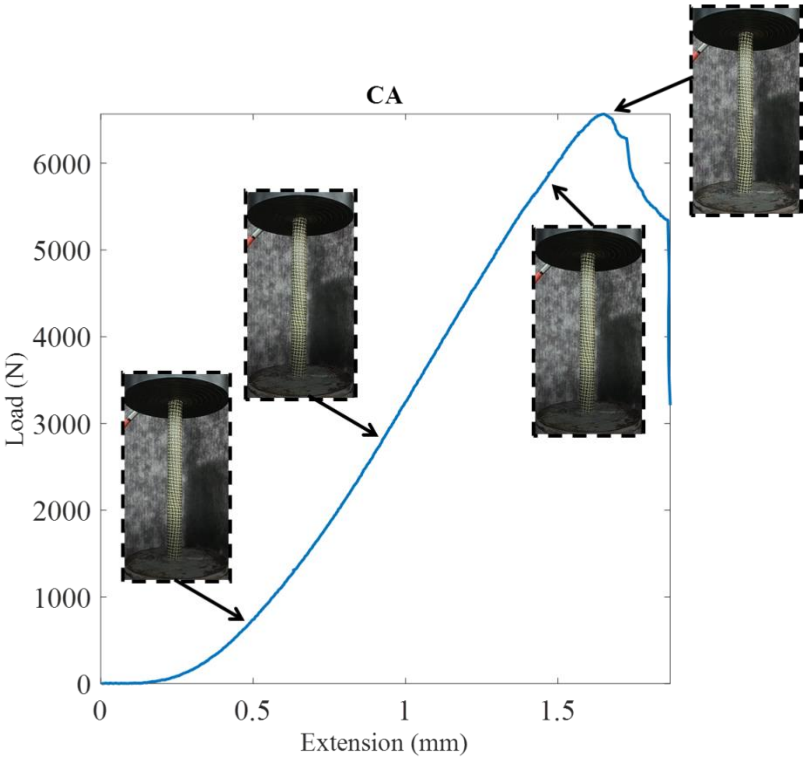

Figure 4.31 – Compressive load-extension curves for CA tube with ply drop-offs in compression test.

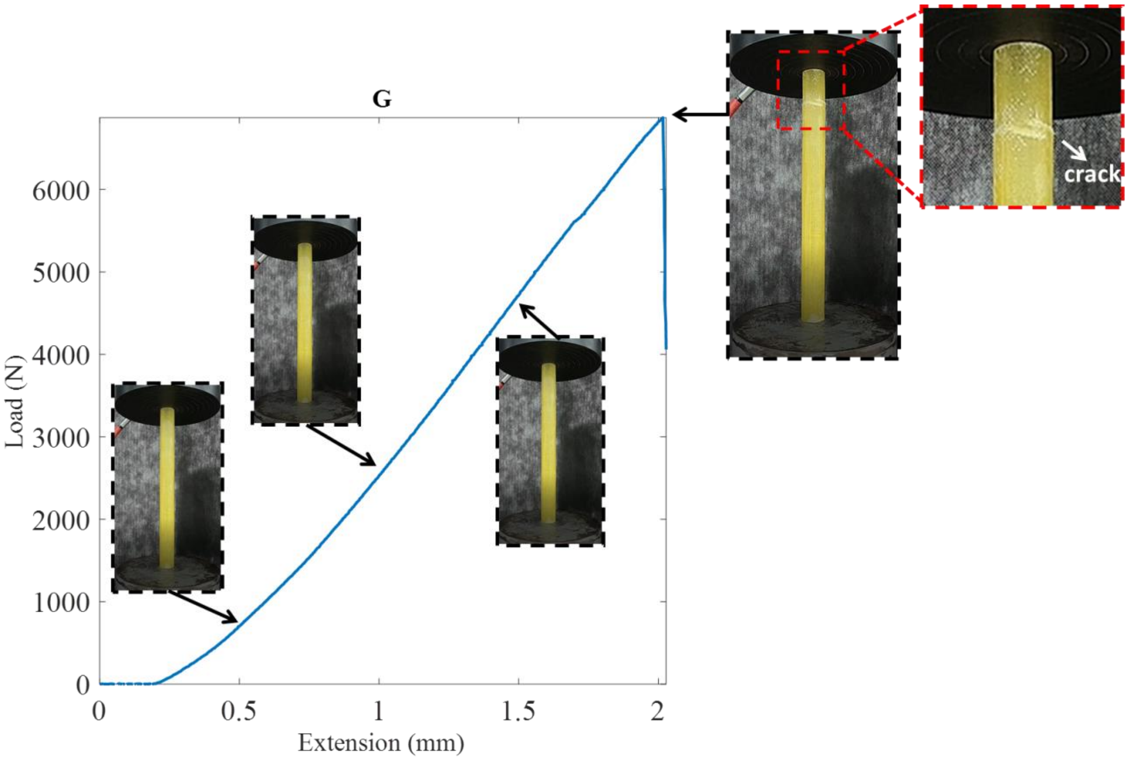

Figure 4.32 – Compressive load-extension curves for G tube with ply drop-offs in compression test.

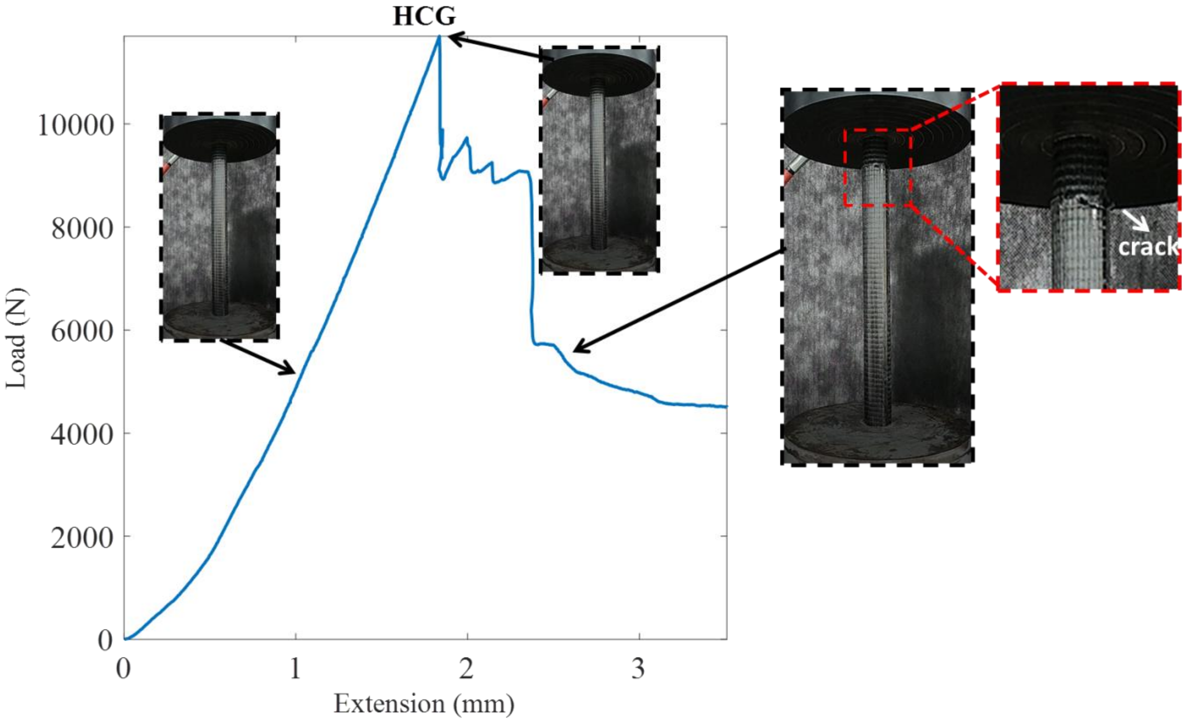

Figure 4.33 – Compressive load-extension curves for HCG tube with ply drop-offs in compression test.

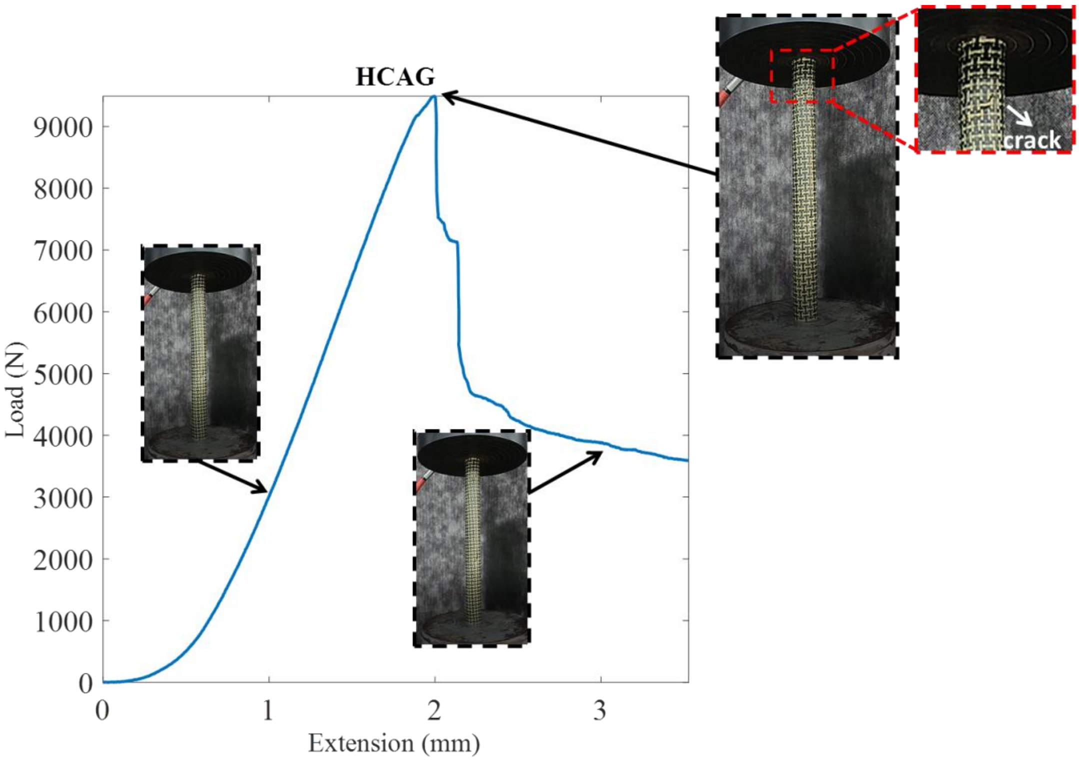

Figure 4.34 – Compressive load-extension curves for HCAG tube with ply drop-offs in compression test.

The results indicate that the C tube with ply drop-offs supports a higher loading of 18.591 kN while the CA tapered tube supports a lower loading of 6.566 kN. The tapered tube manufactured with glass fabric presented a maximum load in compression of 6.870 kN. While the hybrid structures demonstrated promising results with maximum loads of 11.702 kN and 9.489 kN for the HCG and HCAG tubular structures, respectively. As can be confirmed by Figure 4.33, the compressive load-extension curve for the HCG structure showed a slight revival of the loading sometimes during structural displacement.

The results revealed the effectiveness of using a hybrid structure that requires only two carbon plies on the outer surfaces. Because carbon fabric is more expensive when compared with the other types of fibers used in this study, the hybrid tube with glass fabric in the inner plies becomes an excellent choice, providing advantageous properties with a decrease in the cost of materials.

The tubes with ply drop-offs were compressed until they failed structurally. Figure 4.35 depicts the tapered tubes damaged after the compression test.

C tube with ply drop-offs	CA tube with ply drop-offs	G tube with ply drop-offs	HCG tube with ply drop-offs	HCAG tube with ply drop-offs

Figure 4.35 – Failure suffered by tubes with ply drop-offs after compression tests.

It is also important to highlight that the damage is very well indicated in the C, G, and HCG tubular structures. The failure in the tapered tubes follows the same trend with a crack close to the last ply drop-offs, as depicted in Figure 4.35. The damage in this place was expected due to the reduction in the number of plies from 8 to 4 plies, making this part of the structure considered thinner and weaker, as can be confirmed in Figure 4.29. The CA and HCAG structures were also damaged, but the failure was not as visible.

Predictably, the non-tapered tubular structures demonstrated support higher loads in compression conditions. The compressive load-extension curve measured for all tubes without ply drop-offs is shown in Figure 4.36 to Figure 4.40.

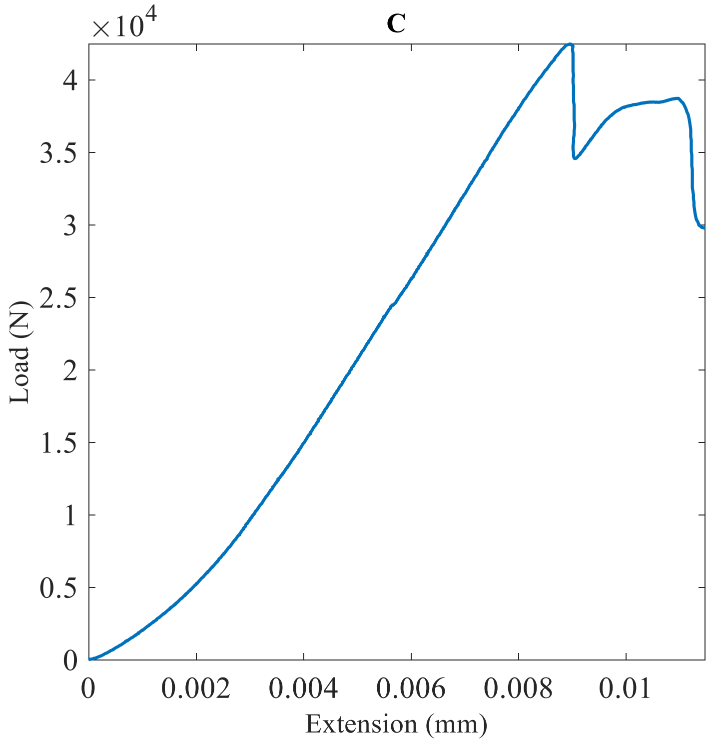

Figure 4.36 – Compressive load-extension curves for C tube without ply drop-offs in compression test.

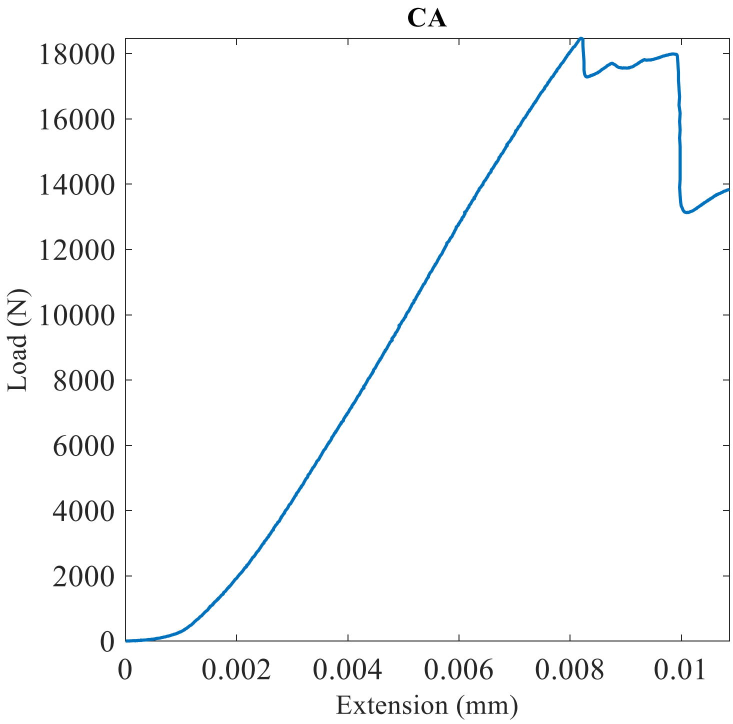

Figure 4.37 – Compressive load-extension curves for CA tube without ply drop-offs in compression test.

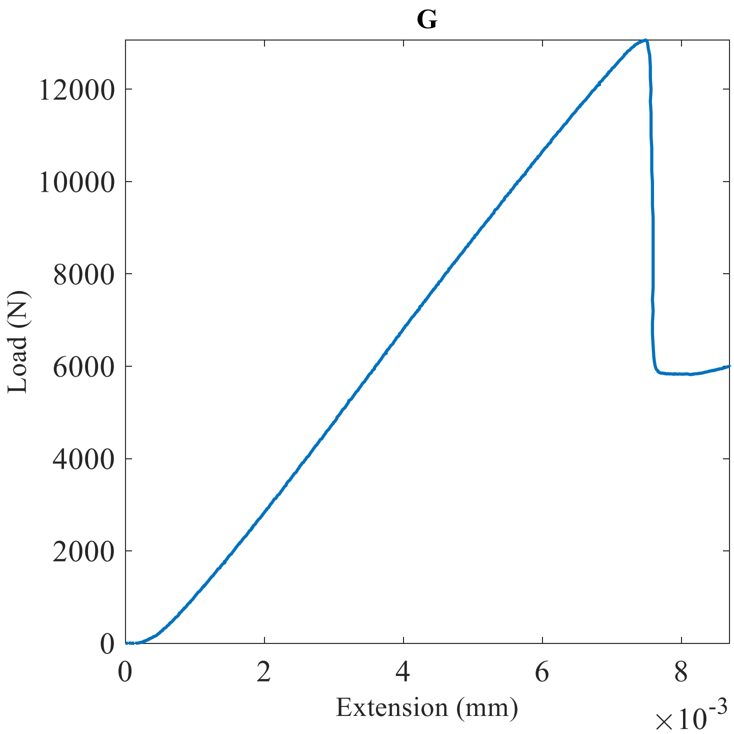

Figure 4.38 – Compressive load-extension curves for G tube without ply drop-offs in compression test.

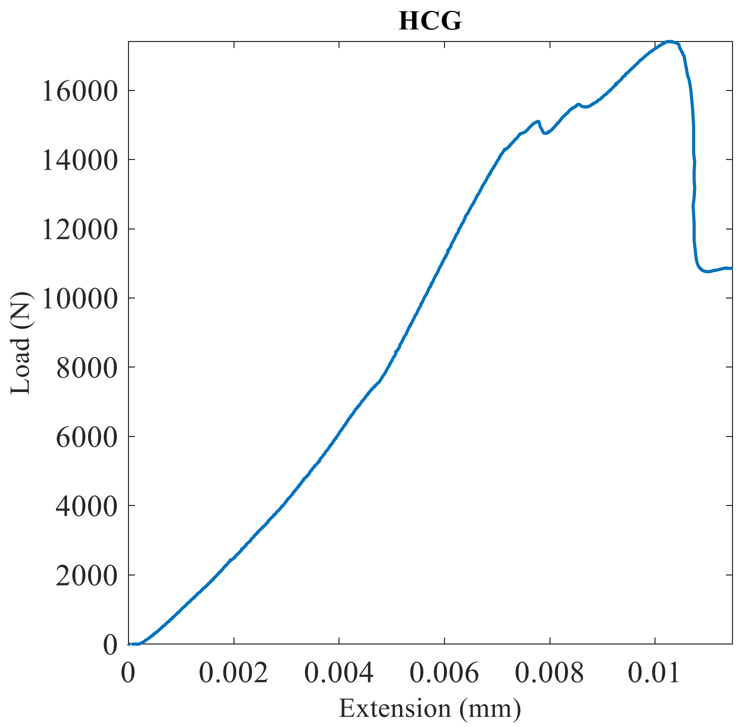

Figure 4.39 – Compressive load-extension curves for HCG tube without ply drop-offs in compression test.

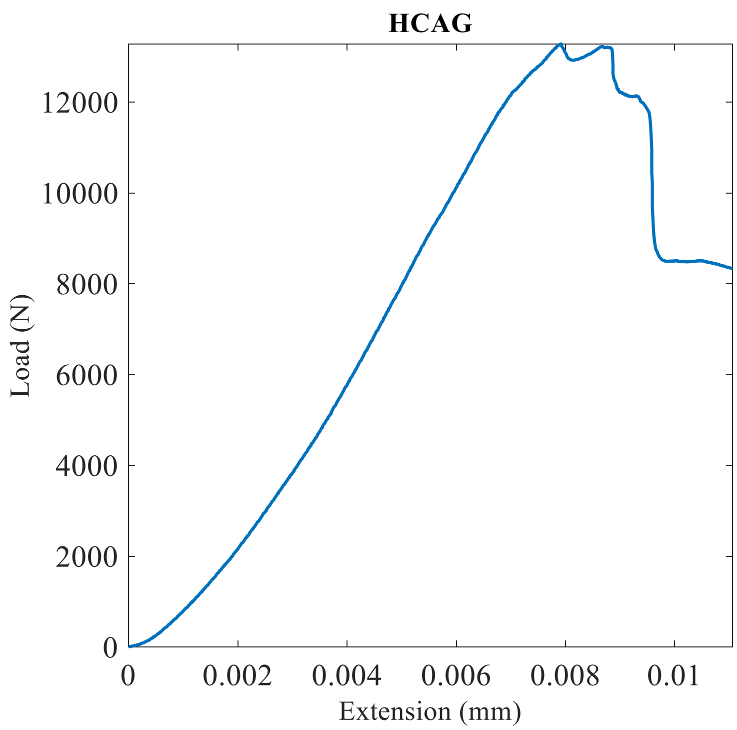

Figure 4.40 – Compressive load-extension curves for HCAG tube without ply drop-offs in compression test.

Again, the tube manufactured only with carbon fibers supported a higher compression load of 42.464 kN. The CA, G, HCG and HCAG tubes without ply drop-offs had maximum compression loads of 18.470 kN, 13.067 kN, 15.100kN, and 13.283 kN, respectively. For non-tapered hybrid structures, there was an increase in the strength in compression conditions of 22% for the HCG and 29% for HCAG when compared with tapered hybrid tubes. The reduction in the compression load for tapered hybrid tubes is considered acceptable when it is remembered that the tapered tubes have only four continus plies and four dropped. Furthermore, the tapered hybrid tubes had a meaningful reduction in mass when compared with non-tapered hybrid tubes. The HCG and HCAG tapered tubes had a decrease of 17% and 30% in mass, respectively, when compared with non-tapered hybrid tubes. As can be noted in Table 4.19, the non-hybrid tubes without ply drop-offs presented a considerable increase in the compression load when compared with the non-hybrid tubes with ply drop-offs.

Table 4.19 – Comparative results for tapered and non-tapered tubes considering maximum compression load and mass variables.

	Tapered tubes		Non-tapered tubes	
Nomenclature	**Maximum compression load (kN)**	**Mass (g)**	**Maximum compression load (kN)**	**Mass (g)**
C	18.591	88.14	42.464	101.23
CA	6.566	54.99	18.470	72.42
G	6.870	55.26	13.067	72.68
HCG	11.702	72.12	15.100	87.18
HCAG	9.489	53.64	13.283	77.03

The compreesion test for non-tapered tubes followed the same guidelines used for tapered tubes, where each tube was compressed until it demonstrated structural failure. The Figure 4.41 depicts the damage caused by compression load in each non-tapered tube.

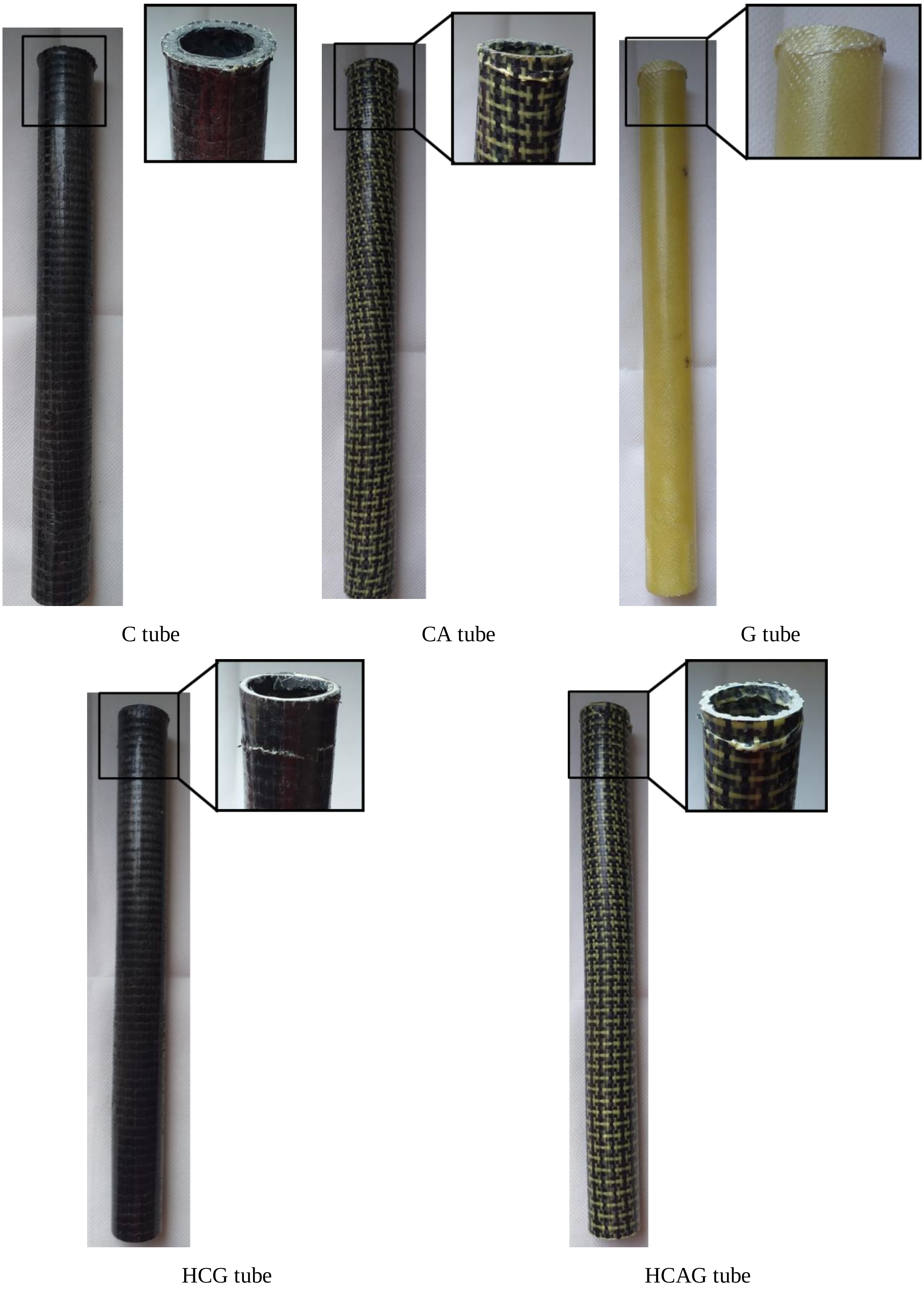

Figure 4.41 – Failure suffered by tubes without ply drop-offs after compression tests.

The failure mode evident in the non-tapered structures was a crack close to the extremity where the loading was applied. An exception was the C tube, which showed crushing in the extremity, as depicted in Figure 4.41.

It is important to note that the ply drop-off in the hybrid setup had their strength in compression slightly affected. It is made up of mass and material cost reductions. Then, it is possible to affirm that the tapered hybrid tubes are a feasible and promising option. As can be confirmed by Table 4.19, the tapered tubes when compared with non-tapered tubes manufactured with single fabric demonstrated a significant strength reduction in the compression conditions. This fact does not discourage the use of ply drop-offs in non-hybrid setups. Certainly, for many designs, the maximum compression loading found for tapered tubes is acceptable and appropriate. In addition to this, the non-hybrid setup also presented a reasonable reduction in the mass and material cost.

4.4.2 Modal experimental test considering intact and damage tubes

The natural frequencies of the free vibration modes and modal damping loss factors for tapered tubes under cantilever boundary conditions were measured, firstly, taking into account an undamaged structure (*bf*), and then a damaged structure (*pf*), to evaluate the interference of structural failure in the dynamic conditions. Table 4.20 presents the results of structural damping percentage and first natural frequencies for pristine and damaged tapered structures.

Table 4.20 – The results are for tubes with ply drop-offs considering the first natural frequency and damping loss factors obtained before and post failure in modal experimental tests.

Nomenclature	Before failure (bf)		Post failure (pf)		Difference (%)	
	ω_{bf} (Hz)	η_{bf} (%)	ω_{pf} (Hz)	η_{pf} (%)	ω	η
C	266	2.2464	253	1.8055	4.89	19.63
CA	262	1.5961	284	1.5498	7.75	2.90
G	204	1.7206	206	1.7259	0.97	0.31
HCG	256	2.5192	247	1.6398	3.52	34.91
HCAG	315	2.2757	245	1.8395	22.22	19.17

The results revealed that the damping loss factor increases with the structural hybridization, where the HCG and HCAG tapered tubes present the higher modal damping loss factors of 2.51% and 2.27%, respectively. It noted that the increase in damping is attributed to a change in the type of fiber in the laminate structure (BHUDOLIA *et al.* 2017). While the lower damping loss factor is found for the CA tapered tube at 1.59%, the C and G tapered tubes had damping loss factors of 2.24% and 1.72%, respectively. The high damping ratios reduces the mechanical vibration and limit its effect on the system (FOUAD *et al.* 2020).

The failure provided the loss of structural integrity, where both the natural frequency and damping loss factor tend to be modified. Kiral *et al.* (2012) ensure that the damping ratio is more sensitive to a failure than the natural frequency. For the modal damping loss factor, the tapered tubular structures demonstrated a considerable reduction in their values, except for the G tube with ply drop-offs that practically remained at the same damping value, as can be confirmed by Table 4.20. This fact can be justified by the friction due to the matrix cracks and broken fibers (KIRAL *et al.* 2012).

The high damping reduction post failure was noted for the HCG structure with ply drop-offs of almost 34.91%. While the CA structure presented a lower reduction of 2.90%, the G structure had an increase in the damping of 0.31%. The HCAG and C structures had damping reduction values of 19.17% and 19.63%, respectively. It is clear that the damping properties of the laminates depend on intrinsic material properties, which strictly depend on material microstructure and viscoelastic properties that consequently depend on external factors, such as the natural frequency (ALSAADI *et al.* 2018; GALOS *et al.* 2019).

Figure 4.42 shows the velocity curve response over time, which allows determining the damping loss factor. While the Figure 4.43 shows the FRF measurements considering the first natural frequency. In both cases, we analyzed each tube with ply drop-offs before and post failure.

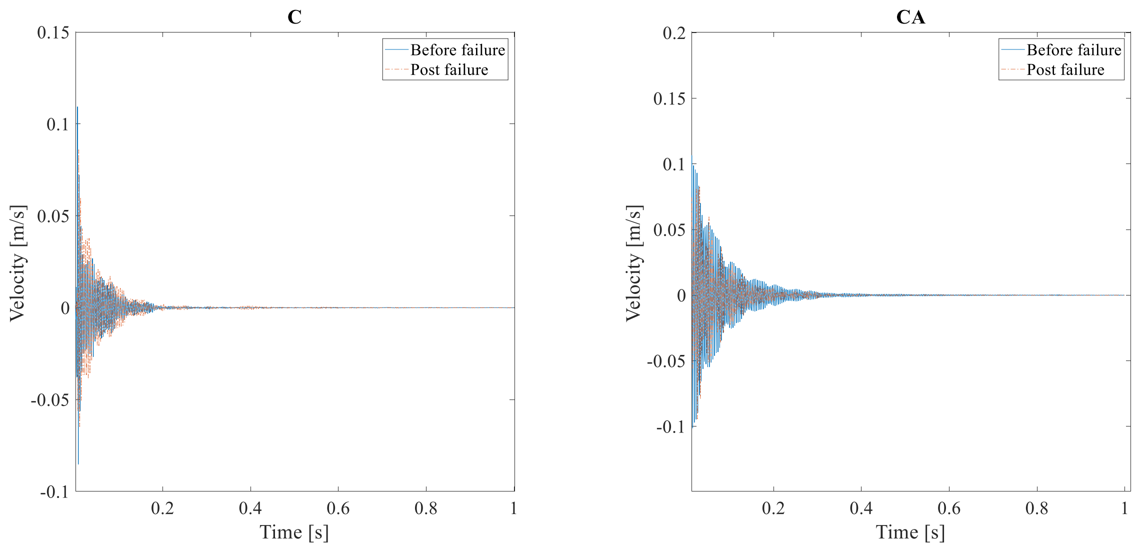

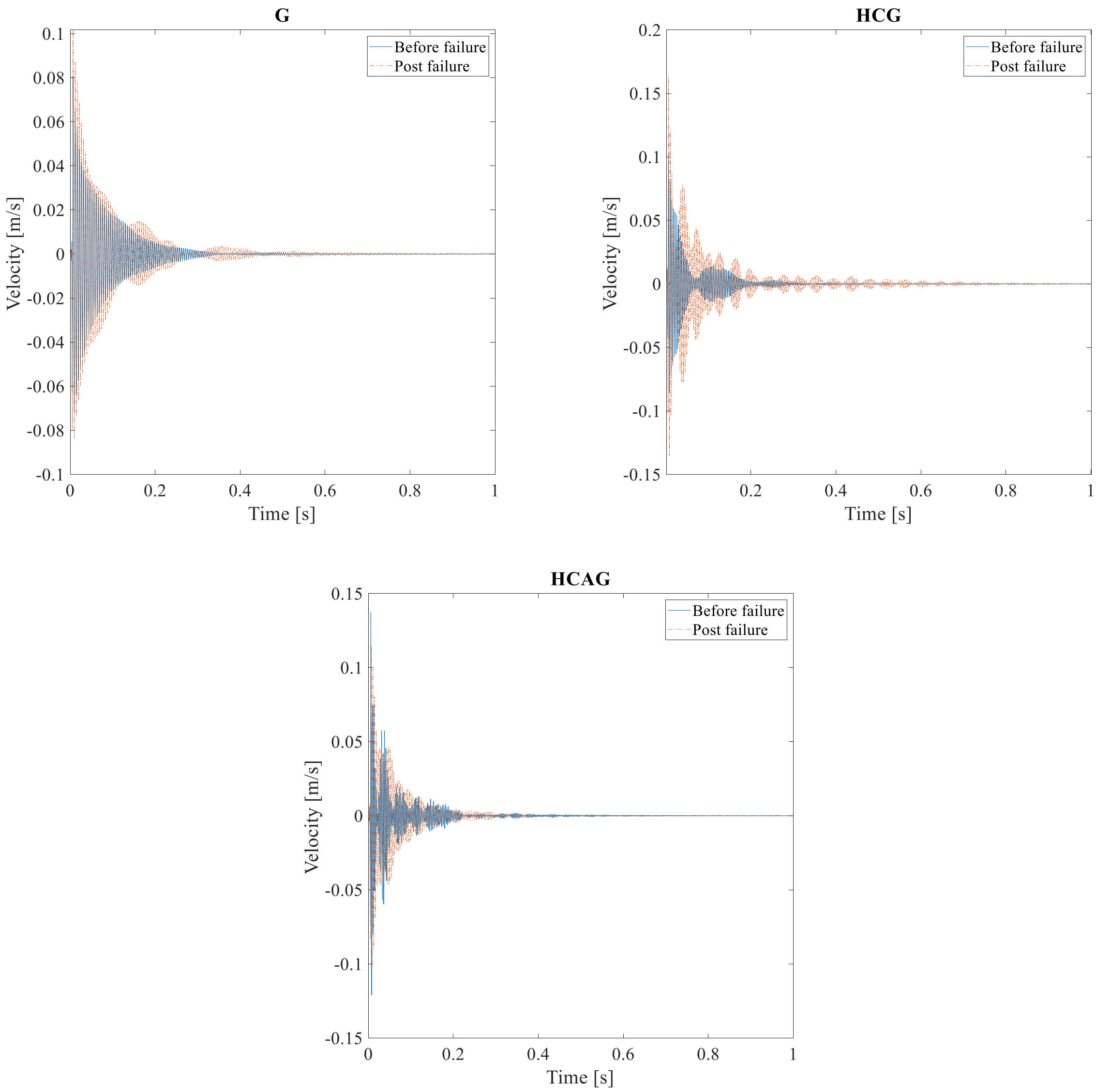

Figure 4.42 – Free vibration analysis considering the velocity vs. time response of all the tubes with ply drop-offs.

(Intentionally left blank)

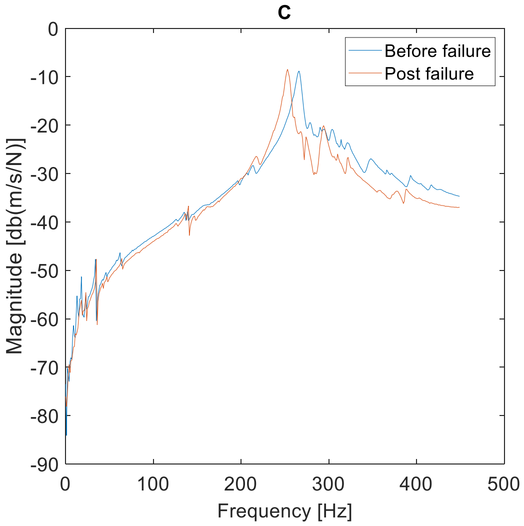

(a) $\omega_{n(before)}$ = 266 Hz and $\omega_{n(post)}$ = 253 Hz

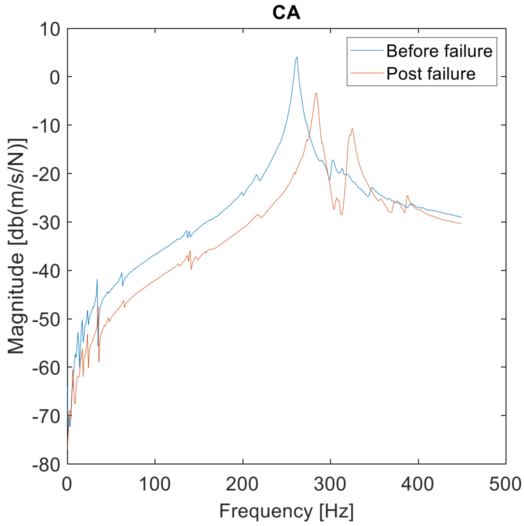

(b) $\omega_{n(before)}$ = 262 Hz and $\omega_{n(post)}$ = 284 Hz

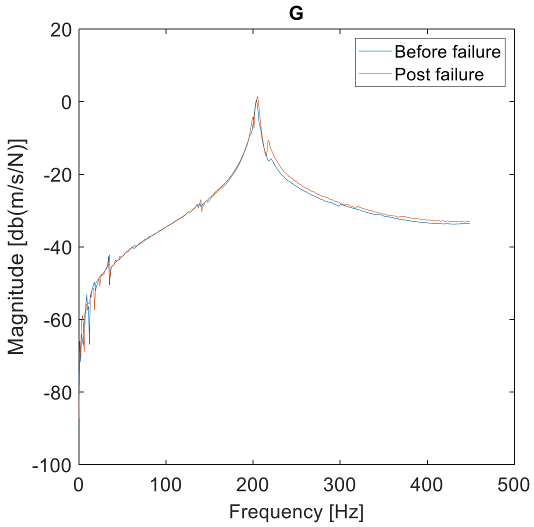

(c) $\omega_{n(before)}$ = 204 Hz and $\omega_{n(post)}$ = 206 Hz

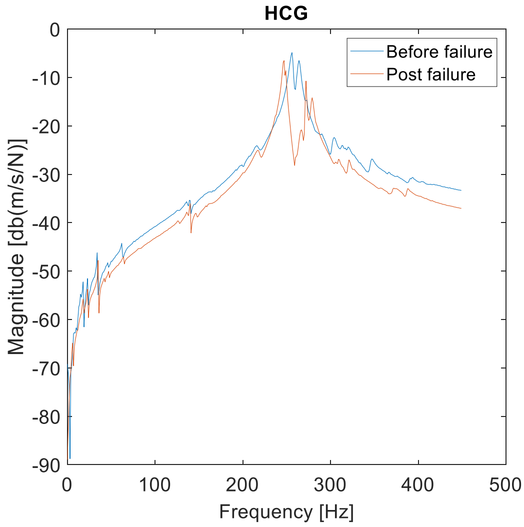

(d) $\omega_{n(before)}$ = 256 Hz and $\omega_{n(post)}$ = 247 Hz

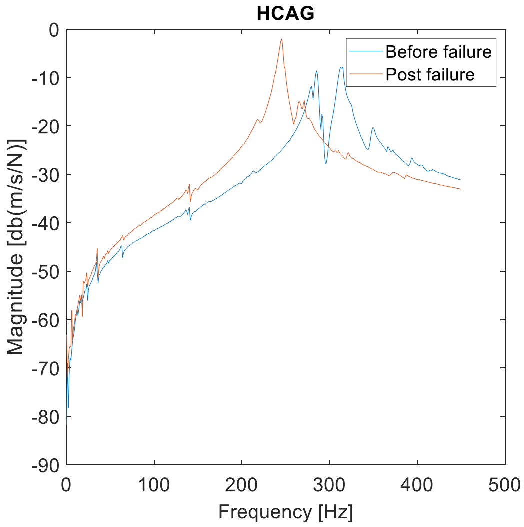

$\omega_{n(before)}$ = 315 Hz and $\omega_{n(post)}$ = 245 Hz

Figure 4.43 – Frequency response functions (FRFs) before and post failure of five different types of tubes with ply drop-offs.

It is possible to note that the first natural frequencies obtained before and post failure present a similarity to the same shape of the curves, as can be confirmed by Figure 4.43. However, there is a slight disagreement between the levels of the natural frequencies before and post-failure. These differences are mainly due to the fact that the total stiffness of the laminate is reduced when the structure presents some type of damage. Consequently, changes in the composite’s stiffness cause changes in the natural frequencies provided that the resonant frequency depends on the physical and geometrical properties of the composite (NSENGIYUMVA *et al.* 2021).

As can be easily seen in Figure 4.43, the CA structure presented a high natural frequency post-failure when compared with the natural frequency before failure. According to Pérez *et al.* (2014), the natural frequencies have practical limitations due to their low sensibility to damage, necessitating sometimes precise measurements or large damage levels to cause a decrease in the natural frequencies. The G structure presented natural frequencies before and after failure very close to 204 Hz and 206 Hz, respectively. As can be seen in Figure 4.43, the C, HCA, and HCAG structures revealed a discrepancy between the natural frequencies before and post failure.

Finally, the modal test results for tapered tubes are summarized through a comparison between the natural frequencies and damping loss factors considering undamaged and damaged tapered structures, as can be seen in Figure 4.44.

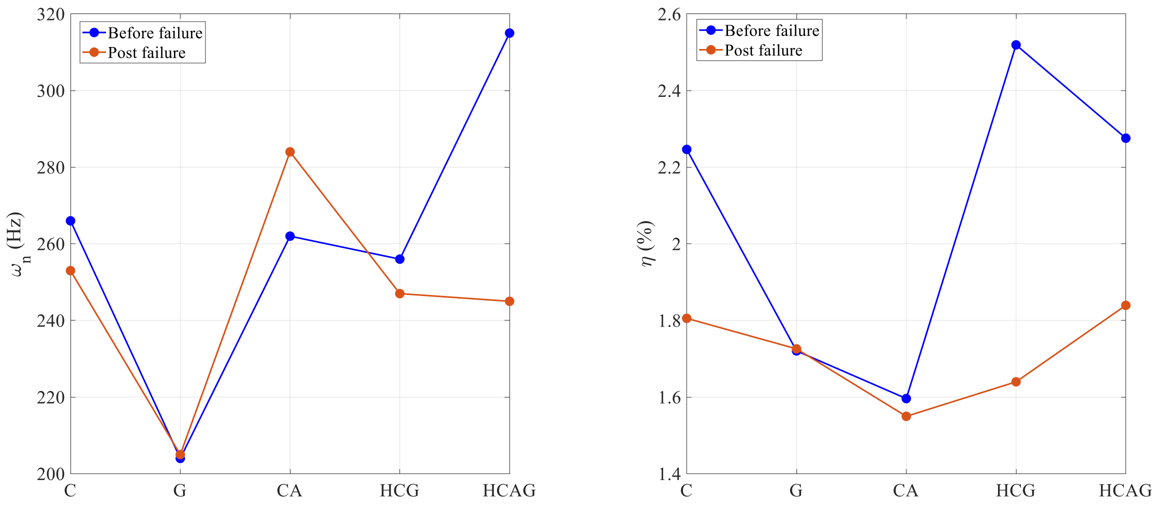

(a) (b)

Figure 4.44 – Experimental results before and after failure of tapered tubes considering the modal parameters of (a) fundamental natural frequencies and (b) damping loss factors.

As would be observed in Figure 4.44a, the higher peak of natural frequency of 315 Hz is found for HCAG tubes with ply drop-offs, while the lower natural frequency of 204 Hz is obtained by tubes manufactured with glass fabric, both considering pristine structures. For damaged structures, the higher peak of natural frequency is found in the CA tube and the lower in the G tube. As the natural frequency is attributed to the stiffness of the material, it is possible to affirm that the hybrid tube with ply drop-offs manufactured with carbon/aramid and glass fabrics can be considered stiffer, while the G tube has low stiffness, taking into consideration pristine structures.

As detailed previously, the discrepancy between the damping loss factor values obtained before and post failure is notable mainly for the C, HCG, and HCAG tubular structures, as can be confirmed by Figure 4.44b.

For non-tapered tubular structures, the modal test results in relation to the damping loss factor and natural frequency obtained before and post failure are depicted in Figure 4.45 and Figure 4.46, respectively.

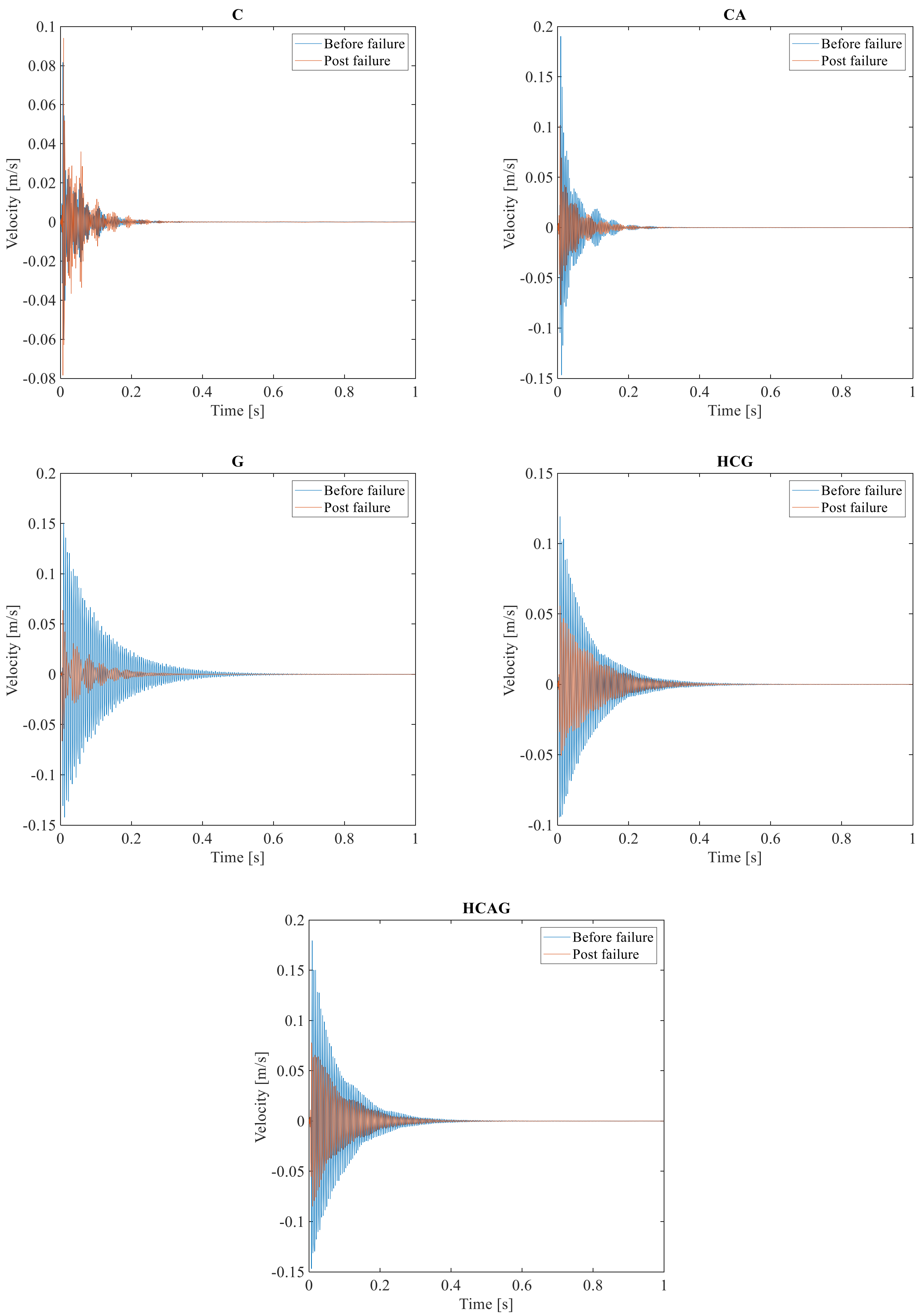

Figure 4.45 – Free vibration analysis considering the velocity vs. time response of all the tubes without ply drop-offs.

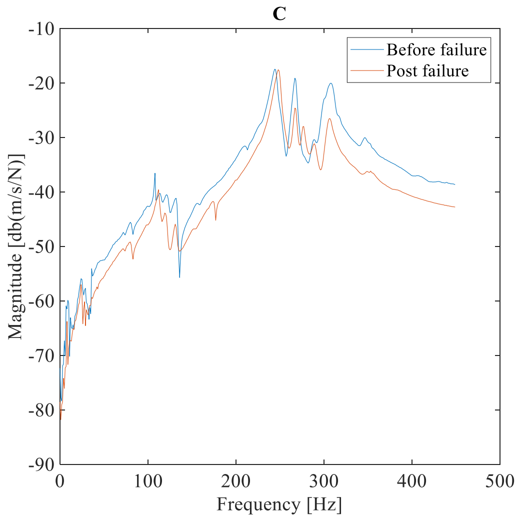

(a) $\omega_{n(before)}$ = 244 Hz and $\omega_{n(post)}$ = 248 Hz

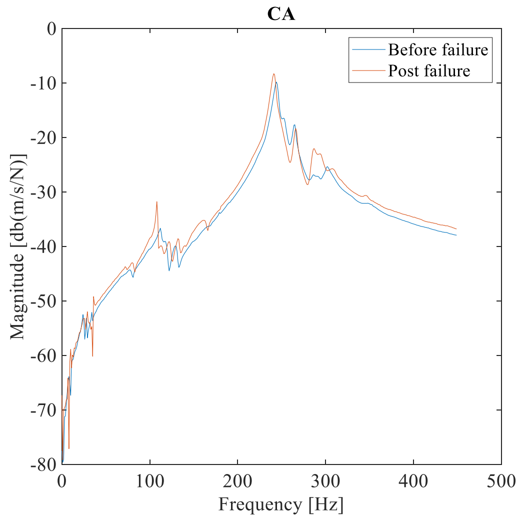

(b) $\omega_{n(before)}$ = 245 Hz and $\omega_{n(post)}$ = 241 Hz

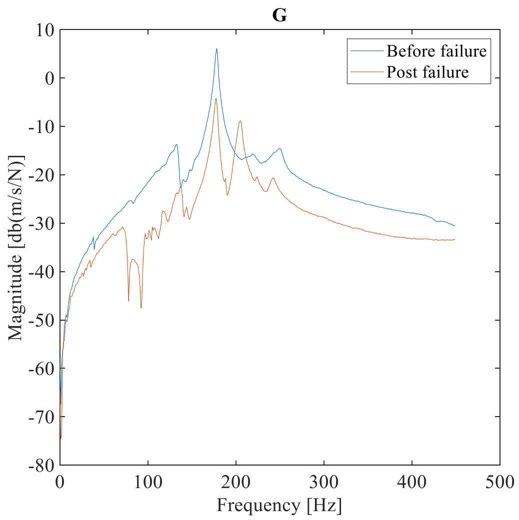

(c) $\omega_{n(before)}$ = 178 Hz and $\omega_{n(post)}$ = 177 Hz

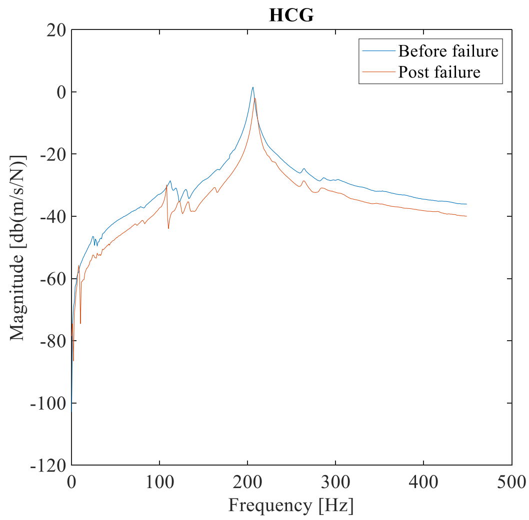

(d) $\omega_{n(before)}$ = 206 Hz and $\omega_{n(post)}$ = 209 Hz

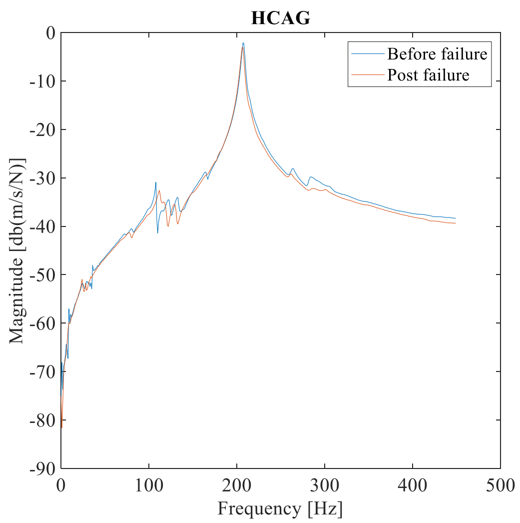

(e) $\omega_{n(before)}$ = 207 Hz and $\omega_{n(post)}$ = 206 Hz

Figure 4.46 – Frequency response functions (FRFs) before and post failure of five different types of tubes without ply drop-offs.

It is possible to infer a little noise at the beginning of the natural frequency curves, which can have been caused by environmental conditions. However, the first natural frequency was clearly identified in each modal analysis. The modal results considering the non-tapered tubes are summarized in Table 4.21.

Table 4.21 – The results are for tubes without ply drop-offs considering the first natural frequency and damping loss factors obtained before and post failure in modal experimental tests.

Nomenclature	Before failure (bf)		Post failure (pf)		Difference (%)	
	ω_{bf} (Hz)	η_{bf} (%)	ω_{pf} (Hz)	η_{pf} (%)	ω	η
C	244	3.2283	248	3.2687	1.61	1.24
CA	245	2.2347	241	2.2876	1.63	2.31
G	178	5.5078	177	2.0489	0.56	62.80
HCG	206	1.5719	209	1.3316	1.43	15.29
HCAG	207	1.6161	206	1.8355	0.48	11.95

The non-tapered tubes presented a reduction in the first natural frequency when compared with tapered tubes. Due to the absence of ply drop-off, the structural mass tends to be higher and, consequently, the natural frequency and stiffness are reducted, as occurred for the tubes without ply drop-offs. Similarly to the G and CA tapered tubes, the C and HCG non-tapered tubes presented an increase in the first natural frequency post failure. As can be observed in Table 4.21, the before and post failure first natural frequency values were very close for all the cases. For the non-tapered structures, the higher damping reduction is noted in the G structure with 62.80%. The C and CA structures demonstrated an increase in the damping after failure of 1.24% and 2.31%, respectively. While the HCG hybrid structure had a damping reduction after failure of 11.95%, the HCAG structure presented an increase in the damping post failure of 15.29%, as can be confirmed by Table 4.21. With knowledge about modal results, it is clear that the tapered tubes are more susceptible to damage than the non-tapered tubes. The natural frequency values suffered more with the damage, as can be observed by the range between the natural frequencies obtained before and post failure in Table 4.20.

Then, it can be concluded that the optimized tapered tubular structures have appropriated static and dynamic behavior for various applications. The hybrid setup is more indicated due their lightness, low material cost, high damping and excellent compression strength. For the hybrid setups, the dropping of four plies caused little impact in the mechanical properties.

(Intentionally left blank)

CHAPTER 5: FINAL REMARKS

5.1 General Conclusion

This study proposed a metamodel-based optimization strategy to determine the best parameters for the use of ply drop-offs in laminate composite in order to examine their static and dynamic behavior, aiming for excellent mechanical performance. The metamodel involving Design of Experiments, SunFlower Optimizer Algorithm, and Finite Element Method was proposed for a cantilever beam with two ply drop-offs and, posteriorly, for hybrid and non-hybrid tubes with four ply drop-offs, considering results related to mass, strain, failure criterion, buckling loading, and natural frequency. The results obtained with the optimization allowed us to know the best ply drop-off location. But besides that, it allowed us to understand the effect of the ply drop-off in relation to mechanical performance. A characterization study of different types of fabric was performed through the manufacture of sandwich structures using experimental tests. Firstly, the optimum layout for the tapered tubular structure was manufactured, and then non-tapered tubes were also manufactured. Lastly, experimental tests were conducted to prove the feasibility of the use of ply drop-offs in the tubular structures.

The main conclusions of this study are as follows:

- The metamodel created by optimization of the beam with ply drop-offs revealed that the failure criterion response variable was not significant with low fit quality, with an R^2_{adj} of 48.60%. One possible reason for this is that the dropped ply was oriented at 90º, and when this type of ply is dropped, it presents low interlaminar stress, demonstrating a negligible effect on the stress distribution. Besides that, the laminate had 16 plies stacked and only two were dropped. Because of this fact, the structural failure did not occur. The strain and first natural frequency response variables demonstrated how well the model fits the data, with an R^2_{adj} of 94.67% and 93.81%, respectively. The longitudinal position design factor demonstrated a high influence on all the response variables;
- In relation to the multiobjective optimization using RSM with desirability, to minimize the strain and maximize the first natural frequency, it is necessary that the second ply be dropped at a longitudinal position of 0.1008m. This dimension is located between the

fifth and seventy panels. With knowledge of these parameters, the tapered beam presented a strain of 0.0013m with a first natural frequency of 101.32 Hz;

- The metamodel proposed for the hybrid and non-hybrid tapered tubes involving the Design of Experiments and SunFlower Optimization Algorithm revealed a significant reduction in structural mass with the use of the ply drop-offs and hybrid setup. The mass variable response demonstrated low quality of fit, with R^2_{adj} less than 70%. While the failure criterion in compression and buckling load response variables presented an R^2_{adj} of 99.49% and 99.08%, respectively, demonstrating high predictive capability;

- The region close to ply drop-off, demonstrated an intensity increase of the stress related to the failure. Nevertheless, all failure criterion values were lower than 1, proving that the structures are secure. In this case, the laminate had 10 plies stacked with their four dropped plies, which could cause an increase in the stress intensity in the region close to ply drop-off;

- In relation to buckling, the hybrid tapered tubular structure had a maximum buckling load of 22.203 kN while the non-hybrid structure presented 16.173 kN. These values are much higher than the recommended ISO standard of 4.4480 kN. Finally, the optimum parameters for the ply drop-off location are the fourth and fifth plies dropped at the position of 0.10 m and 0.24 m, respectively, considering a hybrid structure. In this case, the ply drop-offs are located close to the two extremities of the tubes;

- The characterization study performed with sandwich structures considering bending, buckling, and vibration conditions revealed that all four fabrics have advantageous mechanical properties. However, the hybrid fabric manufactured with glass and aramid fibes presented a high mass and cost, besides being difficult to handle. For this, only the fabrics of glass, carbon, and carbon/aramid were selected for the manufacture of the tubes;

- The tubes with ply drop-offs were designed with five different setups in mind and provided excellent mechanical properties. Experimental tests revealed that the hybrid structures supported a high compression load, with a maximum load in compression for the HCG structure of 11.702 kN and of 9.489 kN for the HCAG structure. The damping loss factors had a significant increase due to the hybridization of the tubular structures. The HCG tube presented a damping loss factor of 2.51%, while the HCAG tube had a 2.27%;

- The investigation into the dynamic behavior before and post failure, revealed a decrease in the damping loss factor and natural frequency of the tubular structures. In fact, this is expected due to the total stiffness of the laminate being reduced when the structure presents some type of damage;

- The non-tapered tubes had an increase in the compression load and structural mass when compared with tapered tubes due to the absence of ply drop-offs in the laminate. The HCG and HCAG non-tapered tubes presented an increase in mass of 17% and 30%, respectively, while the maximum compression load increased by 22% and 29%, respectivelly. The reduction in the strength of these structures is proportional to the mass reduction;
- The tapered structures were demonstrated to be more sensible to damage than the non-tapered structures considering dynamic conditions. The non-tapered tubes suffered minor variations in the natural frequency values obtained before and post failure. While the tapered tubes had a winder range between the natural frequency values obtained before and post failure.

In general, this study revealed the optimum parameters for the manufacture of ply drop-offs in tubular structures considering static and dynamic behavior with hybrid and non-hybrid setups. A new tubular structure was elaborated numerically and experimentally, promoting meaningful mechanical performance. The findings and observations presented in this study will serve to apply in future studies the optimum ply drop-off location considering planar and tubular structures acoordingly to design requirements, while also understanding the mechanical behavior of tapered structures and knowing the mechanical properties of different fabrics.

5.2 Publications and Submissions

The publications resulting out of this thesis study is listed below:

- Diniz, C. A., Méndez, Y., de Almeida, F. A., da Cunha Jr, S. S., Gomes, G. F. (2021). Optimum design of composite structures with ply drop-offs using response surface methodology. **Engineering Computations**, 38(7), 3036-3060.
DOI 10.1108/EC-07-2020-0354.
Impact factor: 1.59.

• Diniz, C. A., Pereira, J. L. J., da Cunha Jr, S. S., Gomes, G. F. Drop-off location optimization in hybrid CFRP/GFRP composite tubes using design of experiments and SunFlower optimization algorithm. **Applied Composite Materials**.
DOI 10.1007/s10443-022-10046-z.
Impact factor: 2.18.

The submissions resulting out of this thesis study are listed below:

• Diniz, C. A., Bortoluzzi, D. B., Pereira, J. L. J., da Cunha Jr, S. S., Gomes, G. F. On the influence of manufacturing parameters on buckling and modal properties of sandwich composite structures. Submitted to **Structures Journal** – Journal – Elsevier (Paper under revision by the Journal).
Impact factor: 2.98.

• Diniz, C. A., Pereira, J. L. J., Bortoluzzi, D. B., da Cunha Jr, S. S., Gomes, G. F. The influence of the type of fabric on the static and dynamic behavior of composite tubes with drop-off. Submitted to **Engineering Structures** – Journal – Elsevier (Paper under revision by the Journal).
Impact factor: 5.69.

5.3 Further Works

The main suggestions for further works are:

• Application of the metamodel created in this study to other types of structures;

• Analyses of other parameters related to ply drop-offs, such as fiber orietantion and ply drop-off size;

• Develop experiments to determine the basic properties of the material used in the manufacture of the tapered tubes, with the goal of numerical models that are as close to reality as possible.

REFERENCES

ABBADI, A., KOUTSAWA, Y., CARMASOL, A., BELOUETTAR, S., AZARI, Z. (2009). Experimental and numerical characterization of honeycomb sandwich composite panels. **Simulation Modelling Practice and Theory**, 17, 1533-1547.

ADAMU, M., RAHMAN, M. R., HAMDAN, S. (2019). Formulation optimization and characterization of bamboo/polyvinyl alcohol/clay nanocomposite by response surface methodology. **Composites Part B: Engineering**, 176, 107297.

ALBANESI, A., ROMAN, N., BRE, F., FACHINOTTI, V. (2018a). A metamodel-based optimization approach to reduce the weight of composite laminated wind turbine blades. **Composite Structures**, 194, 345-356.

ALBANESI, A., BRE, F., FACHINOTTI, V., GEBHARDT, C. (2018b). Simultaneous ply-order, ply-number and ply-drop optimization of laminate wind turbine blades using the inverse finite element method. **Composite Structures**, 184, 894-903.

ALSAADI, M., BULUT, M., ERKLIĞ, A., JABBAR, A. (2018). Nano-silica inclusion effects on mechanical and dynamic behavior of fiber reinforced carbon/Kevlar with epoxy resin hybrid composites. **Composites Part B: Engineering**, 152, 169-179.

AMAECHI, C. V., CHESTERTON, C., BUTLER, H. O., GILLET, N., WANG, C., JAE, I. A., REDA, A., ODIJIE, A. C. (2022). Review of Composite Marine Risers for Deep-Water Applications: Design, Development and Mechanics. **Journal of Composites Science**, 6 (3), 96.

AN, H., CHEN, S., HUANG, H. (2019). Stacking sequence optimization and blending design of laminated composite structures. **Structural and Multidisciplinary Optimization**, 59(1), 1-19.

ARBAOUI, J., MOUSTABCHIR, H., PRUNCU, C. I., SCHMITT, Y. (2018). Modeling and experimental analysis of polypropylene honeycomb multi-layer sandwich composites under four-point bending. **Journal of Sandwich Structures & Materials**, 20, 493-511.

ARTEIRO, A., FURTADO, C., CATALANOTTI, G., LINDE, P., CAMANHO, P. P. (2020). Thin-ply polymer composite materials: A review. **Composites Part A: Applied Science and Manufacturing**, 105777.

ASTM E2954–15, standard test method for axial compression test of reinforced plastic and polymer matrix composite vertical members, ASTM International, West Conshohocken, PA.

ASTM C364/C364M-16, standard test method for edgewise compressive strength of sandwich constructions, ASTM International, West Conshohocken, PA.

ASTM C393/C393M-20, standard test method for core shear properties of sandwich constructions by beam flexure, ASTM International, West Conshohocken, PA.

BARBERO, E. J. (2014). **Finite Element Analysis of Composite Materials using Ansys**.CRC press.

BAKHTIARI, A., GHASEMI, F. A., NADERI, G., NAKHAEI, M. R. (2020). An approach to the optimization of mechanical properties of polypropylene/nitrile butadiene rubber/halloysite nanotube/polypropylene-g-maleic anhydride nanocomposites using response surface methodology. **Polymer Composites**. 41, 1-14.

BHUDOLIA, S. K., PERROTEY, P., JOSHI, S. C. (2017). Enhanced vibration damping and dynamic mechanical characteristics of composites with novel pseudo-thermoset matrix system. **Composite Structures**, 179, 502-513.

BISAGNI, C. (2005). Dynamic buckling of fiber composite shells under impulsive axial compression. **Thin-walled structures**, 43(3), 499-514.

CAIRNS, D. S., MANDELL, J. F., SCOTT, M. E., MACCAGNANO, J. Z. (1999). Design and manufacturing considerations for ply drops in composite structures. **Composites Part B: Engineering**, 30(5), 523-534.

CAMPBELL, F. C. (2010). **Structural Composite Materials**. ASM International.

CRUPI, V., EPASTO, G., GUGLIELMINO, E. (2012). Collapse modes in aluminium honeycomb sandwich panels under bending and impact loading. **International Journal of Impact Engineering**, 43, 6-15.

DHURVEY, P., MITTAL, N. D. (2013). Review on various studies of composite laminates with ply drop off Analysis. ARPN **Journal of Engineering and Applied Sciences**, 8 (8).

DINIZ, C. A., CUNHA, S. S., GOMES, G. F., ANCELOTTI, A. C. (2019). Optimization of the Layers of Composite Materials from Neural Networks with Tsai–Wu Failure Criterion. **Journal of Failure Analysis and Prevention**, 19(3), 709-715.

DUTRA, J. R., RIBEIRO FILHO, S. L. M., CHRISTOFORO, A. L., PANZERA, T. H., SCARPA, F. (2019). Investigations on sustainable honeycomb sandwich panels containing eucalyptus sawdust, Piassava and cement particles. **Thin-Walled Structures**, 143, 106191.

EYVAZIAN, A., TAGHIZADEH, S. A., HAMOUDA, A. M., TARLOCHAN, F., MOEINIFARD, M., GOBBI, M. (2019). Buckling and crushing behavior of foam-core hybrid composite sandwich columns under quasi-static edgewise compression. **Journal of Sandwich Structures & Materials**, 1099636219894665.

EWINS, D.J. (2000). **Modal testing: Theory and practice**. Baldock, England: Research Studies Press.

FITRIAH, S. N., MAJID, M. S. A., RIDZUAN, M. J. M., DAUD, R., GIBSON, A. G., ASSALEH, T. A. (2017). Influence of hydrothermal ageing on the compressive behaviour of glass fibre/epoxy composite pipes. **Composite structures**, 159, 350-360.

FOUAD, H., MOURAD, A. H. I., ALSHAMMARI, B. A., HASSAN, M. K., ABDALLAH, M. Y., HASHEM, M. (2020). Fracture toughness, vibration modal analysis and viscoelastic behavior of Kevlar, glass, and carbon fiber/epoxy composites for dental-post applications. **Journal of the mechanical behavior of biomedical materials**, 101, 103456.

GAO, X., ZHANG, M., HUANG, Y., SANG, L., HOU, W. (2020). Experimental and numerical investigation of thermoplastic honeycomb sandwich structures under bending loading. **Thin-Walled Structures**, 155, 106961.

GALOS, J., KHATIBI, A. A., & MOURITZ, A. P. (2019). Vibration and acoustic properties of composites with embedded lithium-ion polymer batteries. **Composite Structures**, 220, 677-686.

GHASEMI, F. A., GHASEMI, I., MENBARI, S., AYAZ, M., ASHORI, A. (2016). Optimization of mechanical properties of polypropylene/talc/graphene composites using response surface methodology. **Polymer Testing**, 53, 283-292.

GOMES, G. F., DINIZ, C. A., DA CUNHA, S. S., ANCELOTTI, A. C. (2017). Design optimization of composite prosthetic tubes using ga-ann algorithm considering tsai-wu failure criteria. **Journal of Failure Analysis and Prevention**, 17(4), 740-749.

GOMES, G. F., MENDÉZ, Y. A. D., ALEXANDRINO, P. D. S. L., DA CUNHA JR, S. S., ANCELOTTI JR, A. C. (2018). The use of intelligent computational tools for damage detection and identification with an emphasis on composites–a review. **Composite Structures**, 196, 44-54.

GOMES, G. F., DA CUNHA, S. S., ANCELOTTI, A. C. (2019). A SunFlower optimization (SFO) algorithm applied to damage identification on laminated composite plates. **Engineering with Computers**, 35(2), 619-626.

HAN, Q., QIN, H., LIU, Z., HAN, Z., ZHANG, J., NIU, S., ZHANG, W., SUN, Y., SHI, S. (2020). Experimental investigation on impact and bending properties of a novel dactyl-inspired sandwich honeycomb with carbon fiber. **Construction and Building Materials**, 253, 119161.

HEYLEN, W., LAMMENS, S., SAS, P. (1997). **Modal analysis theory and testing** (Vol. 200). Leuven, Belgium: Katholieke Universiteit Leuven.

INMAN, D. J. (2014). **Engineering vibration**. Boston Pearson.

IRISARRI, F. X., LASSEIGNE, A., LEROY, F. H., LE RICHE, R. (2014). Optimal design of laminated composite structures with ply drops using stacking sequence Tables. **Composite Structures**, 107, 559-569.

International Standard (2016) ISO 10328 prosthetics - structural testing of lower-limb prostheses - requirements and test methods. ISO, Switzerland.

JONES, R. (1968). Buckling of circular cylindrical shells with multiple orthotropic layers and eccentric stiffeners. **AIAA Journal**, 6(12), 2301-2305.

KAPPEL, E. (2019). Distortions of composite aerospace frames due to processing, thermal loads and trimming operations and an assessment from an assembly perspective. **Composite Structures**, 220, 338-346.

KIRAL, Z., İÇTEN, B. M., KIRAL, B. G. (2012). Effect of impact failure on the damping characteristics of beam-like composite structures. **Composites Part B: Engineering**, 43(8), 3053-3060.

KOLLAR, L. P., SPRINGER, G. S. (2003). **Mechanics of composite structures**. Cambridge university press.

KRISTINSDOTTIR, B. P., ZABINSKY, Z. B., TUTTLE, M. E., NEOGI, S. (2001). Optimal design of large composite panels with varying loads. **Composite Structures**, 51(1), 93-102.

KUMAR, D. S., RAJMOHAN, M. (2019). Optimizing Wear Behavior of Epoxy Composites Using Response Surface Methodology and Artificial Neural Networks. **Polymer Composites**, 40(7), 2812-2818.

LI, M., DENG, Z., LIU, R., GUO, H. (2011). Crashworthiness design optimisation of metal honeycomb energy absorber used in lunar lander. **International Journal of crashworthiness**, 16, 411-419.

LIU, Q., LI, Y., CAO, L., LEI, F., WANG, Q. (2018). Structural design and global sensitivity analysis of the composite B-pillar with ply drop-off. **Structural Multidisciplinary Optimization**, 57(3), 965-975.

LI, S., GUO, X., LIAO, J., LI, Q., SUN, G. (2020). Crushing analysis and design optimization for foam-filled aluminum/CFRP hybrid tube against transverse impact. **Composites Part B: Engineering**, 196, 108029.

LI, F., LI, R., LI, D. (2022). Manufacture and Bending Test of a Cylindrical Laminated Tube with Integrally Formed Ring Flanges. **Applied Composite Materials**, 1-32.

LUND, E. (2018). Discrete Material and Thickness Optimization of laminated composite structures including failure criteria. **Structural and Multidisciplinary Optimization**, 57(6), 2357–2375.

MARTINS, A. T. D. (2015). Projeto e Fabricação de Tubos Compósitos em Fibras de Carbono/Epóxi para Próteses Transtibiais por Moldagem com Bladder. Master in Engineering Thesis - Universidade Federal de Itajubá.

MESSAC, A., MATTSON, C. A. (2004). Normal constraint method with guarantee of even representation of complete Pareto frontier. **AIAA journal**, 42 (10), 2101-2111.

MONTGOMERY, D. C. (2017). **Design and Analysis of experiments**. John Wiley & Sons.

MONTGOMERY, D. C., PECK, E. A., VINING, G. G. (2021). **Introduction to linear regression analysis**. John Wiley & Sons.

MUC, A. (2018). Design of blended/tapered multilayered structures subjected to buckling constraints. **Composite Structures**, 186, 256-266.

MUKHERJEE, B., VARUGHESE, B. (2001). Design guidelines for ply drop-off in laminated composite structures. **Composite Part B Engineering**, 32(2), 153-164.

MYERS, R.H., MONTGOMERY, D.C., ANDERSON-COOK, C.M. (2016). **Response Surface Methodology: Process and Product Optimization Using Designed Experiments**. John Wiley and Sons.

NARESH, K., SHANKAR, K., VELMURUGAN, R., GUPTA, N. K. (2018). Statistical analysis of the tensile strength of GFRP, CFRP and hybrid composites. **Thin-Walled Structures**, 126, 150-161.

NASAB, F. F., GEIJSELAERS, H. J. M., BARAN, I., AKKERNAN, R., DE BOER, A. (2018). A leve-set-based strategy for thickness optimization of blended composite structures. **Composite Structures**, 206, 903-920.

NSENGIYUMVA, W., ZHONG, S., LIN, J., ZHANG, Q., ZHONG, J., HUANG, Y. (2021). Advances, limitations and prospects of nondestructive testing and evaluation of thick composites and sandwich structures: A state-of-the-art review. **Composite Structures**, 256, 112951.

ONKAR, A. K. (2019). Nonlinear buckling analysis of damaged laminated composite plates. **Journal of Composite Materials**, 53(22), 3111-3126.

PANETTIERI, E., MONTEMURRO, M., CATAPANO, A. (2019). Blending constraints for composite laminates in polar parameters space. **Composite Part B**, 168, 448-457.

PEETERS, D,. ABDALLA, M. (2016). Optimization of Ply Drop Locations in Variable-Stiffness Composites. **AIAA JOURNAL**, 54(5), 1760-1768.

PERRY, T. G., DOUGLAS, C. D., GORMAN J. J. (1992). Analytical design procedures for buckling dominated graphite/epoxy pressure hulls. **SNAME Transactions**, 100, 93-115.

PYO, J., PARK, H., JANG, M., CHOI, J., KUMAR, S. K. S. (2021). Tubular laminated composite structural battery. **Composites Science and Technology**, 208, 108646.

QAIS, M. H., HASANIEN, H. M., ALGHUWAINEM, S. (2019). Identification of electrical parameters for three-diode photovoltaic model using analytical and sunflower optimization algorithm. **Applied Energy**, 250, 109-117.

RAO, S.S., GRIFFIN, P. (2018). **Mechanical vibrations**. Harlow: Pearson.

RAVISHANKAR, B., NAYAK, S. K., KADER, M. A. (2019). Hybrid composites for automotive applications – A review. **Journal of Reinforced Plastics and Composites**, 38 (18), 835-845.

SANZ-CORRETGE, J. (2019). A constraint satisfaction problem algorithm for large-scale multi-panel composite structures. **Structural and Multidisciplinary Optimization**, 1-17.

SHIM, D. J. (2002). Role of delamination and interlaminar fatigue in the failure of laminates with ply dropoffs (Doctoral dissertation, Massachusetts Institute of Technology).

SHRIVASTAVA, S., MOHITE, P. M., LIMAYE, M. D. (2019). Optimal design of fighter aircraft wing panels laminates under multi-load case environment by ply-drop and ply-migrations. **Composite Structures**, 207, 909-922.

SJØLUND, J. H., PEETERS, D., LUND, E. (2019). Discrete Material and Thickness Optimization of sandwich structures. **Composite Structures**, 217, 75-88.

SUDHAGAR, P.E., BABU, A.A., RAJAMOHAN, V. AND JEYARAJ, P. (2017). Structural optimization of rotating tapered laminated thick composite plates with ply drop-offs. International **Journal of Mechanics and Materials in Design**, 13(1), 85-124.

SUN, G., HUO, X., CHEN, D., LI, Q. (2017). Experimental and numerical study on honeycomb sandwich panels under bending and in-panel compression. **Materials & Design**, 133, 154-168.

THOMAS, T., TIWARI, G. (2019). Crushing behavior of honeycomb structure: a review. **International journal of crashworthiness**, 24, 555-579.

TSAI, S. W., WU, E. M. (1971). A general theory of strength for anisotropic materials. **Journal of composite materials**, 5(1), 58-80.

TSAI, S. W., HAHN, H. T. (1980). **Introduction to composite materials**. CRC Press.

VEMULURI, R. B., RAJAMOHAN, V., SUDHAGAR, P. E. (2018). Structural optimization of tapered composite sandwich plates partially treated with magnetorheological elastomers. **Composite Structures**, 200, 258-276.

VIDYASHANKAR, B. R., MURTY, A. V. K. (2001). Analysis of laminates with ply drops. **Composites Science and Technology**, 61(5), 749–758.

VOYIADJIS, G. Z., KATTAN, P. I. (2005). **Mechanics of composite materials with Matlab**. Springer.

XU, Y., ZHU, J., WU, Z., CAO, Y., ZHAO, Y., ZHANG, W. (2018). A review on the design of laminated composite structures: constant and variable stiffness design and topology optimization. **Advanced Composites and Hybrid Materials**, 1(3), 460-477.

YANG, H., LEI, H., LU, G., ZHANG, Z., LI, X., LIU, Y. (2020). Energy absorption and failure pattern of hybrid composite tubes under quasi-static axial compression. **Composites Part B: Engineering**, 198, 108217.

YUAN, Z., WANG, W., WANG, H., RAZMJOOY, N. (2020). A new technique for optimal estimation of the circuit-based PEMFCs using developed sunflower optimization algorithm. **Energy Reports**, 6, 662-671.

ZENG, J., HUANG, Z., CHEN, Y., LIU, W., CHU, S. (2019). A simulated annealing approach for optimizing composite structures blended with multiple stacking sequence Tables. **Structural and Multidisciplinary Optimization**, 60(2), 537-563.

ZHANG, B., KAWASHITA, L. F., JONES, M. I., LANDER, J. K., & HALLETT, S. R. (2020). An experimental and numerical investigation into damage mechanisms in tapered laminates under tensile loading. **Composites Part A: Applied Science and Manufacturing**, *133*, 105862.

ZHANG, X., TIAN, Y., JIN, Y. (2014). A knee point-driven evolutionary algorithm for many-objective optimization. **IEEE Transactions on Evolutionary Computation**, 19(6), 761-776.

ZHAO, W., KAPANIA, R. K. (2018). BLP Optimization of Composite Flying-wings with SpaRibs and Multiple Control Surfaces. In 2018 AIAA/ASCE/AHS/ASC Structures, Structural Dynamics, and Materials Conference (p, 2150).

ZHAO, X., ZHU, G., ZHOU, C., YU, Q. (2019). Crashworthiness analysis and design of composite tapered tubes under multiple load cases. **Composite Structures**, 222, 110920.

ZOU, J., LI, Q., YANG, S., BAI, H., ZHENG, J. (2017). A prediction strategy based on center points and knee points for evolutionary dynamic multi-objective optimization. **Applied Soft Computing**, 61, 806-818.

WEISS, A., TRABELSI, W., MICHEL, L., BARRAU, J, J., MAHDI, S. (2010). Influence of ply-drop location on the fatigue behaviour of tapered composites laminates. **Procedia Engineering**, 2(1), 1105–1114.

Appendix A. General Full Factorial Design

First, a full factorial design was created with the goal of recognizing the influence of the design factors on ply drop-off locations, as shown in Table A1.

Table A1a – General full factorial design considering two design factors and three response variables (part I).

No	Design factors		Output responses		
	Plies	Panels	Tsai Wu	Strain (mm/mm)	Frequency (Hz)
1	2	2	0.45215	0.00133	99.76500
2	2	3	0.45242	0.00132	101.28000
3	2	4	0.45243	0.00132	101.88000
4	2	5	0.45243	0.00131	101.63000
5	2	6	0.45243	0.00131	100.58000
6	2	7	0.45243	0.00130	98.73800
7	3	2	0.45252	0.00142	97.67300
8	3	3	0.45243	0.00140	101.27000
9	3	4	0.45243	0.00137	101.50000
10	3	5	0.45243	0.00135	101.53000
11	3	6	0.45243	0.00133	100.57000
12	3	7	0.45243	0.00132	98.73800
13	4	2	0.45212	0.00173	90.41700
14	4	3	0.45242	0.00166	96.46600
15	4	4	0.45243	0.00159	100.01000
16	4	5	0.45243	0.00151	101.14000
17	4	6	0.45243	0.00144	100.51000
18	4	7	0.45243	0.00137	98.73600
19	5	2	0.45252	0.00142	95.39500
20	5	3	0.45243	0.00140	99.11900
21	5	4	0.45243	0.00137	101.06000
22	5	5	0.45243	0.00135	101.42000
23	5	6	0.45243	0.00133	100.55000
24	5	7	0.45243	0.00132	98.73700
25	6	2	0.45212	0.00173	93.09600
26	6	3	0.45242	0.00166	97.91800
27	6	4	0.45243	0.00159	100.59000
28	6	5	0.45243	0.00151	101.29000
29	6	6	0.45243	0.00144	100.53000
30	6	7	0.45243	0.00137	98.73600
31	7	2	0.45252	0.00142	94.16200
32	7	3	0.45243	0.00140	98.48200
33	7	4	0.45243	0.00137	100.81000
34	7	5	0.45243	0.00135	101.35000
35	7	6	0.45243	0.00133	100.54000

Table A1b – General full factorial design considering two design factors and three response variables (part II).

No	Design factors		Output responses		
	Plies	Panels	Tsai Wu	Strain (mm/mm)	Frequency (Hz)
36	7	7	0.45243	0.00132	98.73700
37	8	2	0.45215	0.00133	94.20900
38	8	3	0.45242	0.00132	98.51200
39	8	4	0.45243	0.00132	100.83000
40	8	5	0.45243	0.00131	101.36000
41	8	6	0.45243	0.00131	100.54000
42	8	7	0.45243	0.00130	98.73700